

**Universität
Rostock**



Traditio et Innovatio

**Dynamic Compression Experiments of (Mg,Fe)O
at X-ray Free Electron Laser and Large Laser Facilities**

Dissertation

zur

Erlangung des akademischen Grades

doctor rerum naturalium (Dr. rer. nat)

der Mathematisch-Naturwissenschaftlichen Fakultät

der Universität Rostock

vorgelegt von

Khachiwan Buakor, geb. am 03.10.1994 in Tak, Thailand

aus Halstenbek

Rostock, 2024

Gutachter/innen der Dissertation:

Dr. Thomas Tschentscher, European XFEL

Prof. Dr. Carmen Sanchez-Valle, Universität Münster, Institut für Mineralogie

Prof. Dr. Hauke Marquardt, University of Oxford, Department of Earth Sciences

Jahr der Einreichung: 2024

Jahr der Verteidigung: 2025

Universität Rostock

Institut für Physik

18051 Rostock

Tel: +49 381 498-6916

Fax: +49 381 498-6912

Internet: <http://www.physik.uni-rostock.de>

Email des Autors: khachiwan.buakor@xfel.eu

Abstract

Over 5800 exoplanets including super-Earths, a class of rocky planets with 2 to 10 Earth masses, have been discovered and confirmed in the past decades. Understanding and modeling the structure and formation of super-Earths strongly rely on the knowledge of phase stability and physical properties of relevant compounds at extreme conditions. (Mg,Fe)O is one of the major phases constituting to the Earth's and Super Earth's mantle. It has been the subject of intensive investigation including structural and electronic phase transition. However, the properties of (Mg,Fe)O solid solutions at ultra-high pressure, i.e. the pressure relevant to planetary interiors, are still mostly unknown. This study aims to investigate the structural phase stability of (Mg,Fe)O and its end-member FeO under laser-driven shock compression at a pressure up to above 200 GPa. Powder-epoxy mixtures namely slurry targets and physical vapor deposition (PVD) targets were used in this study. In addition, (Mg,Fe)O was prepared with different Fe compositions to study the effect of Fe-Mg substitution on (Mg,Fe)O phase behaviors. X-ray diffraction (XRD) along the Hugoniot states was measured and the pressure conditions were determined by the velocity interferometer system for any reflector (VISAR) and hydrodynamic simulation.

In this study, FeO was shock-compressed up to the maximum pressure of 250 GPa. The B1-structure FeO was stable up to 172 GPa and liquid FeO was observed from 189 GPa. In addition, the volume reduction of FeO at 120 to 130 GPa could be observed: it could originate from electronic transitions such as the high spin to low spin transition in the FeO B1 structure. The results of (Mg,Fe)O show that the maximum pressure of 270 GPa was reached. The Hugoniot shock velocity (U_s)- particle velocity (U_p) relation of slurry (Mg_{0.9}, Fe_{0.1}) O was successfully obtained as $U_s = 1.4355U_p + 4.5962$. The XRD measurement revealed the stability of the B1-structure (Mg,Fe)O in all the compositions up to 180 GPa. The differences due to the Fe constituents in (Mg,Fe)O could not be concluded. The B1-B2 phase transition of (Mg_{0.9}, Fe_{0.1}) O could be observed at a pressure of approximately 240 GPa. Apart from that, the broad XRD peak features consisting of at least two peaks were observed in (Mg_{0.9}, Fe_{0.1}) O and (Mg_{0.2}, Fe_{0.8}) O at more than 1 ns after the shock breakout. These could be explained by inhomogeneity of temperature and pressure or dissociation of (Mg,Fe)O during the shock release.

Zusammenfassung

In den letzten Jahrzehnten wurden mehr als 5800 Exoplaneten, darunter Super-Erden, eine Klasse von Gesteinsplaneten mit 2 bis 10 Erdmassen, entdeckt und bestätigt. Das Verständnis und die Modellierung der Struktur und Bildung von Super-Erden basieren stark auf dem Wissen über die Phasenstabilität und die physikalischen Eigenschaften relevanter Verbindungen unter extremen Bedingungen. (Mg,Fe)O ist eine der Hauptphasen, die den Erdmantel und den Mantel von Super-Erden bilden. Es war Gegenstand intensiver Untersuchungen, einschließlich struktureller und elektronischer Phasenübergänge. Die Eigenschaften der (Mg,Fe)O Mischkristallen unter extrem hohem Druck, d.h. dem Druck, der für das Innere von Planeten relevant ist, sind jedoch noch weitgehend unbekannt. Diese Studie zielt darauf ab, die strukturelle Phasenstabilität von (Mg,Fe)O und seinem Endglied FeO unter laserinduzierter Schockkompression bis zu einem Druck von über 200 GPa zu untersuchen. Die Pulver-Epoxid-Gemische, sogenannte Slurry-Proben, sowie Proben, welche mittels physikalischer Dampfabscheidung (PVD) hergestellt wurden, wurden in dieser Studie verwendet. Darüber hinaus wurde (Mg,Fe)O mit unterschiedlichen Fe-Zusammensetzungen hergestellt, um den Einfluss der Fe-Mg-Substitution auf das Phasenverhalten von (Mg,Fe)O zu untersuchen. Röntgenbeugung (XRD) entlang der Hugoniot-Zustände wurde gemessen und die Druckbedingungen wurden mit dem Velocity-Interferometer-System für beliebige Reflektoren (VISAR) und hydrodynamischer Simulation bestimmt.

In dieser Studie wurde FeO bis zum maximalen Druck von 250 GPa schockkomprimiert. Die B1-Struktur von FeO war bis 172 GPa stabil, und flüssiges FeO wurde ab 189 GPa beobachtet. Darüber hinaus konnte eine Volumenreduktion von FeO bei 120 bis 130 GPa beobachtet werden, die auf elektronische Übergänge wie den Übergang von Hochspin zu Niedrigspin in der FeO-B1-Struktur zurückzuführen sein könnte. Die Ergebnisse von (Mg,Fe)O zeigen, dass ein maximaler Druck von 270 GPa erreicht wurde. Die Hugoniot-Schockgeschwindigkeits (U_s)-Partikelgeschwindigkeits (U_p)-Beziehung von Slurry ($\text{Mg}_{0.9}, \text{Fe}_{0.1}$) O wurde erfolgreich als $U_s = 1.4355U_p + 4.5962$ bestimmt. Die XRD-Messung zeigte die Stabilität der B1-Struktur von (Mg,Fe)O in allen Zusammensetzungen bis zu 180 GPa. Unterschiede aufgrund der Fe- Zusammensetzung in (Mg,Fe)O konnten nicht festgestellt werden. Der B1-B2-Phasenübergang von ($\text{Mg}_{0.9}, \text{Fe}_{0.1}$) O konnte bei einem Druck von etwa 240 GPa beobachtet werden. Darüber hinaus wurden in ($\text{Mg}_{0.9}, \text{Fe}_{0.1}$) O und ($\text{Mg}_{0.2}, \text{Fe}_{0.8}$) O mehr als 1 ns nach dem Schockausbruch breite

XRD-Peakmerkmale mit mindestens zwei Peaks beobachtet. Diese könnten durch Inhomogenität der Temperatur und des Drucks oder die Dissoziation von (Mg,Fe)O während der Schockentlastung erklärt werden.

Acknowledgements

This work would not be completed if I did not receive many kinds of supports and I would like to take this opportunity to express my gratitude to all those who have been a part of this journey.

First of all, I would like to express my sincere gratitude to my supervisor Karen Appel for her constant support, inspiration, and exceptional guidance during all stages of my work. I am truly thankful for the opportunity she gave me to explore my ideas and for her constructive feedback. I would also like to thank my supervisor, Prof. Ronald Redmer, for the opportunity to work under his supervision and his great scientific support.

I would like to extend my gratitude to Marion Harmand for the valuable collaborative work and the great discussion, which significantly improved my research experience. I would also like to thank all of my collaborators for their support during the beamtime and the discussion including Thomas Tschentscher, Zuzana Konopkova, Markus Schoelmerich, Melanie Sieber, Victorien Bouffetier, Tommaso Vinci, Alessandra Benuzzi-Mounaix, Adrien Denoëud, Dimitri Khaghani, Hae Ja Lee, Eric Cunningham, Hai-En Tsai, Sergio Speziale, Christian Plueckthun, Sally Tracy, Arianna Gleason, Donghoon Kim, Ian Ocampo, Prof. Thomas Duffy, Prof. François Guyot, Raymond Smith, Maximilian Schörner, and Andy Krygier.

Moreover, I would also like to thank European XFEL for providing a supportive environment and the necessary resources to complete my research. I am deeply grateful to my HED group leader Ulf Zastra for his generous support and stimulating discussions. I would also like to thank the HED staffs for their support and collaboration. I am deeply thankful to my fellow Ph.D. students, especially Anand Dwivedi, Johannes Kaa, Carolina Carmada, Juan Pintor, and Sofia Balugani for the great discussion and their support.

I would like to acknowledge the LCLS and the LULI2000 facilities for granting the beamtimes under the proposal LX64 and the proposal 22-NS-E2, respectively. I would also like to acknowledge the Deutsche Forschungsgemeinschaft (DFG) for the funding support via the Research Unit FOR 2440 “Matter under Planetary Interior Conditions”.

Finally, I would like to express my deepest appreciation to my family for their unwavering support, love, and patience throughout the entire Ph.D. journey. Special thanks go to my partner Phudit, whose constant support, care, and belief in me played a key role in completing this work.

Contents

1	Introduction	1
1.1	Earth and super-Earth compositions and internal structure	1
1.2	Mineralogy of (Mg,Fe)O and its end-members	2
1.3	Dynamic compression experiments	5
1.4	Motivation and goals of this study	7
2	Synthesis and Preparation of (Mg,Fe)O	9
2.1	Physical vapor deposition (PVD)	9
2.2	Gas-mixing furnace	14
2.3	Slurry-target preparation	16
3	Experimental Methods of Shock Compression	19
3.1	Fundamental concepts of shock compression	19
3.2	VISAR diagnostics	22
3.3	Experimental setup at MEC, LCLS	25
3.4	Experimental setup at LULI	28
3.5	Hydrodynamic simulation	30
4	FeO	33
4.1	FeO structures under shock compression	33
4.2	Pressure determination of FeO under shock compression	38
4.3	Discussion	48
5	(Mg,Fe)O	55
5.1	Hugoniot EoS of slurry (Mg,Fe)O	55
5.2	(Mg,Fe)O structures under shock compression	68
5.3	Discussion	81

6	Conclusion and Future Perspectives	91
6.1	Conclusion	91
6.2	Implication for geology and planetary science	93
6.3	Future perspectives	94
A	Parameters from XRD and VISAR analysis	95
B	Example of input for MULTI hydrodynamic simulation	101
	Bibliography	104

List of Figures

1.1	The Earth interior cross-section including the dominant minerals of the mantle and core.	2
1.2	Phase diagram of FeO consisting of the high pressure polymorphs of FeO that are B1 (NaCl), B8 (NiAs), B2 (CsCl) and rB1 structures. Pressure and temperature at the phase boundaries are estimated and modified from the literature. The filled black circles represent results from the shock compression experiments.	4
2.1	Schematic diagram of the PVD system and the PVD machine at IMPMC: (1) vacuum pump, (2) Fe and Mg cathodes, (3) magnetrons, (4) a gas injection system, and (5) substrates on a rotating holder.	10
2.2	Elemental analysis of Fe-Mg-O from the EDS as a function of power on the Fe cathode (left) and the O ₂ flow-rates at the power on Fe cathode of 200W corresponded to the black rectangle of the left plot (right).	11
2.3	XRD of the samples deposited with power on the Fe cathode of 200W and O ₂ flow-rates of 9, 10.5, and 12 sccm. The black rectangle corresponds to (Mg,Fe)O.	12
2.4	XRD of the final sample compared to (Mg _{0.9} , Fe _{0.1})O and (Mg _{0.6} , Fe _{0.4})O from the reference	13
2.5	SEM image of PVD (Mg,Fe)O from the final deposition compared to PVD FeO.	14
2.6	The gas mixing furnace experiment at the Institute of Geosciences of the University of Potsdam: (a)-(b) the equipment of the vertical gas mixing furnace including heater, ceramic tube, water-chilled flanges (top and bottom), logging units for temperature and oxygen fugacity, and gas controller, (c) mixture before putting in the furnace, (d) (Mg _{0.6} , Fe _{0.4})O pellets, and (e) (Mg _{0.9} , Fe _{0.1})O pellets.	15

2.7	XRD of the synthesized powder of $(\text{Mg}_{0.9}, \text{Fe}_{0.1})\text{O}$ and $(\text{Mg}_{0.6}, \text{Fe}_{0.4})\text{O}$ compared to the reference	16
2.8	Configuration of the samples to put in a rolling-mill machine for (a) a slurry with black Kapton and (b) free-standing slurry.	17
2.9	Slurry samples imaged by the microscope with 1-mm resolution (left) and the SEM with 2.5- μm resolution (right).	18
2.10	XRD of $(\text{Mg}_{0.9}, \text{Fe}_{0.1})\text{O}$, $(\text{Mg}_{0.6}, \text{Fe}_{0.4})\text{O}$, $(\text{Mg}_{0.4}, \text{Fe}_{0.6})\text{O}$, and $(\text{Mg}_{0.2}, \text{Fe}_{0.8})\text{O}$ from the slurry targets.	18
3.1	Schematic of a shock wave propagation with the velocity U_s in a gas driven by a piston moving with a constant velocity U_p causing the sudden changes of gas density, pressure, and internal energy from ρ_0 , P_0 , and E_0 to ρ , P , and E	20
3.2	Hugoniot of an unspecified material in $(P, 1/\rho)$ space compared to isentrope (left) and (P, U_p) space (right).	21
3.3	Pressure profiles before and after a shock crossing the interface of material A and B when (a) $Z_A < Z_B$ and (b) $Z_A > Z_B$	22
3.4	Typical configuration of VISAR used for velocity measurement.	23
3.5	VISAR probing on three cases of the moving surfaces under shock-loading: (a) free surface, (b) interface of a transparent standard material and a studied material, and (c) shock front when it become reflective.	24
3.6	VISAR images and the corresponding velocity profiles from Neutrino software from the target parylene-N/FeO/sapphire window. The fringe shifts or velocity jumps were observe at the time when a shock breakout from FeO and Sapphire. The velocity is interpreted as the particle velocity in the sapphire window.	25
3.7	Experimental setup at the MEC instrument of the LCLS: (a) schematic of the experimental setup including target configuration, driven laser pulse-shape, XRD, and VISAR measurement, (b) inside of the target chamber at the MEC experimental hutch, and (c) the target holder viewed from the laser side (top) and VISAR side (bottom).	27

3.8	The X-ray diffraction set up at the LULI2000 laser facility: (a) the diffractometer box in which the north laser illuminated to a backlighter target and the south laser driven to a main target, (b) schematic of the diffractometer side-view where the X-ray incident angle is 30° to the target plane and (c) the target chamber at the LULI2000 laser facility.	29
3.9	Target design for the LULI experiment: configuration of the step target used for EoS measurement (left) and top view of the corresponding target (right).	31
3.10	Example of the MULTI simulation: a pressure map of the target 49- μm parylene-N, 5- μm FeO, and 25- μm sapphire at the corresponding time and initial position.	32
4.1	FeO sample configuration used in this study: (a) 49- μm Parylene-N (PN)/ 5- μm PVD-FeO/ 200-nm Al/ 25- μm sapphire, and (b) 50- μm black Kapton (BK)/ 5- μm PVD-FeO or 26-31 μm slurry-FeO. The 200-nm Al between FeO and sapphire in (a) serves as reflective surface for VISAR. . . .	34
4.2	Integrated XRD lineout of BK/PVD-FeO targets under shock-compression at various laser intensities. Diffraction was obtained by 13-keV X-rays and collected in the Quad 0 detector. The time is given as a relative time to the shock breakout. FeO ambient peaks include the reflection from (111), (200), and (220) planes. The compressed FeO peaks from (200) are labeled as reverted triangles and ambient Fe_2O_3 peaks are marked as a star. The dash lines show the position of Al, which are from a sample frame. . . .	35
4.3	Integrated XRD lineout of the BK/PVD-FeO targets under shock-compression at various laser intensities collected by the Quad 0 detector. They were measured by 17-keV X-rays close to shock breakout time. The FeO ambient peaks include the reflection from (111), (200), and (220) planes. The compressed (200) FeO and ambient Fe_2O_3 peaks are labeled as reverted triangles and stars, respectively. The dash lines show the position of Al, which are from the sample frame.	37
4.4	2D XRD raw images of the PN/FeO/sapphire target taken at ambient conditions and 0.1 ns before shock breakout. No FeO peak is observed during shock indicating the melting of FeO at a laser intensity of $7.1 \times 10^{12} \text{ W/cm}^2$. 38	

4.5	Integrated XRD of the BK/slurry-FeO targets under shock-compression at various laser intensities measured by 13-keV X-rays and collected by the Quad 0 detector. The FeO ambient peaks include the reflection from (111) and (200) planes. The compressed (111) and (200) FeO are labeled as red and black reverted triangles, respectively. The ambient Fe ₃ O ₄ peaks is observed at ambient. The dash lines show the position of Al, which are from a sample frame.	39
4.6	Volume of PVD and slurry FeO observed at the shots with different laser intensities.	40
4.7	Shock breakout-time from FeO of PN/FeO/Sapphire and BK/FeO targets shot with different laser intensities.	41
4.8	Example of impedance matching performed for the shot when the sapphire U_s is equal to 12.5 km/s.	42
4.9	Pressure of FeO of PN/PVD-FeO/Sapphire targets shot with corresponding laser intensities. The pressure was calculated from the impedance matching technique by using U_s in a sapphire as an input. The solid-liquid boundary of FeO is taken from the results as shown in Figure 4.4.	43
4.10	Examples of U_p -time plots at the FeO/Sapphire interface of the shots with laser intensities of 8.6×10^{12} and 5.0×10^{12} W/cm ² . They are compared between the results from hydrodynamic simulation and VISARs.	44
4.11	Shock breakout-time from FeO of PN/FeO/sapphire targets shot at different input laser intensities. The results are taken from hydrodynamic simulation and VISAR data.	45
4.12	Shock breakout-time from FeO of BK/FeO targets shot at different input laser intensities. The results are taken from hydrodynamic simulation and VISAR data	45
4.13	Examples of a pressure map and a corresponding pressure profile at the shock breakout time (5.44 ns) of the PN/FeO/sapphire performed by hydrodynamic simulation with the laser intensity of $0.45 \times 8.57 \times 10^{12}$ W/cm ²	46
4.14	Relation between pressure of FeO of PN/PVD-FeO/Sapphire targets and laser intensities calculated by hydrodynamic simulation.	47

4.15	Relation between pressure of FeO of BK/PVD-FeO targets and laser intensities calculated by hydrodynamic simulation. The solid-liquid boundary of FeO is taken from the XRD results as shown in Figure 4.3.	47
4.16	Relation between pressure and volume of FeO under shock compression compared to the results from DAC experiments.	49
4.17	Relation between pressure and compressed volume (V/V_0) of FeO under shock compression compared to the results from DAC and shock-compression experiments	49
4.18	Example of impedance matching of black Kapton and polycrystalline FeO or slurry FeO. Hugoniot of black Kapton and FeO are taken from the literatures, respectively. Hugoniot of slurry FeO is calculated based on the velocity-based mixing rules from the literature from Hugoniot of FeO and epoxy.	51
4.19	XFEL position on VISAR 1 and 2 from run 285 collected on the second day of the experiment, run 366 and run 367 collected on the third day of the experiment.	53
4.20	Shock breakout time from FeO of the BK/FeO targets. The data is labeled with the collected date: the first day (day 1) and the second day (day 2) of the experiment.	53
5.1	An example of the target configuration (left) and the corresponding VISAR image from VISAR2 (right). The red dash lines indicate breakout time from each layer of the target.	56
5.2	Relation between laser intensity and shock breakout time from Al and quartz (left) and shock propagation time in quartz (right).	57
5.3	Hugoniot $P-U_p$ relation of quartz from the literatures	57
5.4	Relation between pressure of quartz calculated from U_s and laser intensities.	58
5.5	VISAR images of run 18 and the extracted velocity profile from Neutrino software. The velocity profile corresponds to U_s in quartz.	59
5.6	Relation between U_s in slurry ($Mg_{0.9}, Fe_{0.1}$)O and ($Mg_{0.6}, Fe_{0.4}$)O and laser intensity shot on the targets with and without a quartz window.	60
5.7	Example of impedance matching technique performed for run 7 of slurry ($Mg_{0.9}, Fe_{0.1}$)O, when using a mirror reflection of the secondary Hugoniot	62
5.8	Example of impedance matching technique performed for run 7 of slurry ($Mg_{0.9}, Fe_{0.1}$)O, when using a mirror reflection of the principal Hugoniot.	63

5.9	Hugoniot of slurry (Mg _{0.9} , Fe _{0.1})O and slurry (Mg _{0.6} , Fe _{0.4})O plotted in U_s - U_p (left) and pressure- U_p (right). $U_s = 1.4355U_p + 4.5962$ was obtained from linear regression for U_s - U_p relation of slurry (Mg _{0.9} , Fe _{0.1})O.	65
5.10	XRD images of IP2 covering 2θ of approximately 35° to 85° used for calibration taken from the experiment (left) and the simulation (right).	66
5.11	Integrated XRD lineouts of (Mg _{0.9} , Fe _{0.1})O and (Mg _{0.6} , Fe _{0.4})O collected by IP2 at various laser intensities. Black reverted triangles are referred to as reflections from (111), (200), and (220) planes sorted from low to high angles of 2θ and red reverted triangles are compressed (200) peaks. A dash line is labeled as a collimator.	67
5.12	Integrated XRD lineouts of (Mg _{0.9} , Fe _{0.1})O under shock compression at various laser intensities collected by Quad 0 detector. The pressures correspond to the pressure reached at the fully shock-compression by using the corresponding laser intensities. (Mg _{0.9} , Fe _{0.1})O at ambient includes reflections from (111) and (200) planes shown as black dash lines. The compressed (111) and (200) peaks are labeled as black and red reverted triangles, respectively.	69
5.13	2D XRD images of the shots with a laser intensity of 1.16×10^{13} W/cm ² at 0.55 and 1.3 ns after the shock breakout time.	70
5.14	Integrated XRD lineouts of (Mg _{0.6} , Fe _{0.4})O under shock compression at various laser intensities collected by Quad 0 detector. The pressures correspond to the pressure reached at the fully shock-compression by using the corresponding laser intensities. (Mg _{0.6} , Fe _{0.4})O at ambient includes reflections from (111) and (200) planes shown as black dash lines. The compressed (111) and (200) peaks are labeled as black and red reverted triangles, respectively. Q and S are referred to as a target with a quartz or a sapphire window. Al peaks from a sample frame are at blue dash line positions.	71

5.15	Integrated XRD lineouts of $(\text{Mg}_{0.4}, \text{Fe}_{0.6})\text{O}$ under shock compression at a laser intensity of $1.16 \times 10^{13} \text{ W/cm}^2$ collected by Quad 0 detector. $(\text{Mg}_{0.4}, \text{Fe}_{0.6})\text{O}$ at ambient includes reflections from (111) and (200) planes shown as black dash lines. The compressed (111) and (200) peaks are labeled as black and red reverted triangles, respectively. All peaks from a sample frame are at blue dash line positions.	72
5.16	Integrated XRD lineouts of $(\text{Mg}_{0.2}, \text{Fe}_{0.8})\text{O}$ under shock compression at various laser intensities collected by Quad 0 detector. $(\text{Mg}_{0.2}, \text{Fe}_{0.8})\text{O}$ at ambient includes reflections from (111) and (200) planes shown as black dash lines. The compressed (111) and (200) peaks are labeled as black and red reverted triangles, respectively.	74
5.17	2D XRD images of the shots with a laser intensity of $1.16 \times 10^{13} \text{ W/cm}^2$ at 0.5 and 1.8 ns after the shock breakout time.	75
5.18	Volume and density of $(\text{Mg}_{0.9}, \text{Fe}_{0.1})\text{O}$, $(\text{Mg}_{0.6}, \text{Fe}_{0.4})\text{O}$, $(\text{Mg}_{0.4}, \text{Fe}_{0.6})\text{O}$, and $(\text{Mg}_{0.2}, \text{Fe}_{0.8})\text{O}$ under shock compression as a function of laser intensity.	75
5.19	Example VISAR1 and VISAR2 images from run 401 of the BK/epoxy target and the extracted velocity, reflectivity, and quality profile from Neutrino software. The black dash line is referred to as the shock breakout time from black Kapton.	76
5.20	Average shock velocity propagating through black Kapton and slurry $(\text{Mg,Fe})\text{O}$ as a function of laser intensity.	78
5.21	Shock breakout time from black Kapton as a function of laser intensity provided by VISAR measurement and hydrodynamic simulation.	78
5.22	U_s in slurry $(\text{Mg,Fe})\text{O}$ as a function of XRD density estimated from shock breakout time of black Kapton, which was calculated by hydrodynamic simulation with the adjustment of 0.6 to 0.8 ns.	79
5.23	Pressure- U_p relation of slurry $(\text{Mg}_{0.9}, \text{Fe}_{0.1})\text{O}$ and slurry $(\text{Mg}_{0.6}, \text{Fe}_{0.4})\text{O}$. Pressures are calculated from impedance matching with pressure in black Kapton and with U_s or U_p of a quartz or a sapphire window. Density of $(\text{Mg}_{0.9}, \text{Fe}_{0.1})\text{O}$ and $(\text{Mg}_{0.6}, \text{Fe}_{0.4})\text{O}$ are obtained from XRD probed at the shock breakout time from a slurry layer.	81
5.24	U_s - U_p relation of slurry $(\text{Mg}_{0.9}, \text{Fe}_{0.1})\text{O}$ and slurry $(\text{Mg}_{0.6}, \text{Fe}_{0.4})\text{O}$ from this study compared to the previous studies on polycrystalline $(\text{Mg,Fe})\text{O}$	83

5.25	Pressure- U_p relation of slurry ($Mg_{0.9}, Fe_{0.1}$) O and slurry ($Mg_{0.6}, Fe_{0.4}$) O from this study compared to the previous studies on polycrystalline (Mg,Fe)O and the calculated Hugoniot of slurry	85
5.26	Pressure-density relation from this study of shock-compression on slurry ($Mg_{0.9}, Fe_{0.1}$) O compared to the previous research of shock compression on polycrystalline ($Mg_{0.96}, Fe_{0.04}$) O	86
5.27	Pressure-density relation from this study of shock-compression on slurry ($Mg_{0.6}, Fe_{0.4}$) O compared to the previous research of shock compression on polycrystalline ($Mg_{0.6}, Fe_{0.4}$) O	87
5.28	Pressure-unit cell volume relation from this study of shock compression on slurry ($Mg_{0.9}, Fe_{0.1}$) O compared to the previous DAC studies.	88
5.29	Pressure-unit cell volume relation from this study of shock compression on slurry ($Mg_{0.6}, Fe_{0.4}$) O compared to the previous DAC studies.	89
B.1	The corresponding mesh tab of the MULTI simulation.	104

List of Tables

2.1	Amount of Fe_2O_3 and MgO used for synthesis of $(\text{Mg}_{0.9}, \text{Fe}_{0.1})\text{O}$ and $(\text{Mg}_{0.6}, \text{Fe}_{0.4})\text{O}$ powder in this experiment.	16
A.1	Results from XRD peak fitting of PVD- FeO from the experiment at the MEC of LCLS.	96
A.2	Results from XRD peak fitting and refinement of slurry- FeO from the experiment at the MEC of LCLS.	96
A.3	U_s, U_p and pressure of quartz and slurry $(\text{Mg}_{0.9}, \text{Fe}_{0.1})\text{O}$ and slurry $(\text{Mg}_{0.6}, \text{Fe}_{0.4})\text{O}$ obtained from the experiment at the LULI2000 facility	97
A.4	Results from peak fitting and pressure of slurry $(\text{Mg}_{0.9}, \text{Fe}_{0.1})\text{O}$ and $(\text{Mg}_{0.6}, \text{Fe}_{0.4})\text{O}$ obtained from the experiment at the LULI2000 facility	97
A.5	Parameters from XRD refinement of $(\text{Mg}, \text{Fe})\text{O}$ from the experiment at the MEC of LCLS.	98
A.6	Parameters from XRD peak fitting of $(\text{Mg}, \text{Fe})\text{O}$ from the experiment at the MEC of LCLS.	99
A.7	Pressure of slurry $(\text{Mg}_{0.9}, \text{Fe}_{0.1})\text{O}$ and $(\text{Mg}_{0.6}, \text{Fe}_{0.4})\text{O}$ obtained from impedance matching with pressure in black Kapton from hydrodynamic simulation.	99
A.8	Pressure of slurry $(\text{Mg}_{0.6}, \text{Fe}_{0.4})\text{O}$ obtained from impedance matching with U_p or U_s in windows obtained from VISAR.	100

Chapter 1

Introduction

1.1 Earth and super-Earth compositions and internal structure

In 1992, the discovery of first two planets outside our solar system was announced by Aleksander Wolszczan and Dale Frail [1]. Since then the number has been growing and more than 5600 exoplanets have been confirmed until now (as of the 25th of June, 2024). Exoplanets have been confirmed by several methods mainly transit and radial velocity that constitute approximately 90 percent of the discovery. Other than the detection, these methods can provide essential information such as size and mass of the object that is used for classification and characterization. Exoplanets are categorized into four types: gas giants, Neptune-like, super-Earth, and terrestrial.

Super-Earth is a class of exoplanets in which the mass is between 2 to 10 times of the Earth's mass. Until now, more than 1700 exoplanets were classified as super-Earths. Since the definition of a super-Earth references only to the mass, they can comprise a broad range of planetary compositions. For example, the super-Earth CoRoT-7b most likely has a large iron core and a silicate mantle [2], while 55 Cancri e possibly comprises a carbon-rich interior [3]. However, in this thesis, the term "super-Earths" are referred to typical super-Earths that are rocky planets.

Understanding and modeling the internal structure of super-Earths is essential for interpretation of the observed mass and size. To study the super-Earth interiors, one can start from the most known rocky planet that is our Earth. In the past decades, the internal structure of the Earth has been intensively investigated by theoretical and experimental studies with special focus on the mantle which encompasses 82% of the whole volume [5].

The Earth's mantle can be studied by seismic wave velocities that give constraints to theoretical calculations, modeling, and experimental data. The major phases of the upper and lower mantle are illustrated in Figure 1.1. The upper mantle dominantly consists of olivine which transforms to wadsleyite and ringwoodite at the depth of 410 and 660 km, respectively [6]. These phase transitions are observed by a sharp increase of seismic velocity at the boundary to the transition zone. Ringwoodite ($(\text{Mg, Fe})_2\text{SiO}_4$) dissociates into Bridgmanite ($(\text{Mg, Fe})\text{SiO}_3$) and ferropericlase with increasing pressure ($(\text{Mg, Fe})\text{O}$) that are dominant constituents of the lower mantle.

The Earth's mantle extends to the core-mantle boundary (CMB) at 2900 km depth which corresponds to 136 GPa [7]. For super-Earths with greater mass or larger size, the interior pressure rises. For example, the pressure at the CMB of a super-Earth which is five times of the Earth's mass in size ($5M_E$) is expected to be as high as 600 GPa [2][8]. To understand the interior of super-Earths, the knowledge of the mineralogy at relevant high pressure and temperature conditions is needed. This means that understanding of physical properties and phase stability of rock materials such as $(\text{Mg, Fe})\text{SiO}_3$ and $(\text{Mg, Fe})\text{O}$ at these conditions are consequently important.

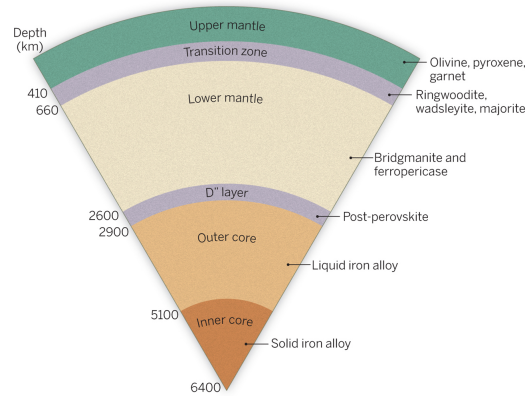


Figure 1.1: The Earth interior cross-section including the dominant minerals of the mantle and core. Modified after [4].

1.2 Mineralogy of (Mg,Fe)O and its end-members

$(\text{Mg,Fe})\text{O}$ is the second most abundant constituent of the Earth's lower mantle and also expected to be one of the main components of super-Earths. The Earth's mantle is mainly composed of bridgmanite and ferropericlase is assumed to be the second most common mineral with an abundance of approximately 16 to 20 percent. [9][10][11]. While theoretical and experimental studies show that the $(\text{Mg,Fe})\text{O}$ in the Earth's lower mantle should be Mg-rich $(\text{Mg,Fe})\text{O}$, some of the $(\text{Mg,Fe})\text{O}$ natural samples as inclusion of the diamonds were found to be Fe-rich $(\text{Mg,Fe})\text{O}$ [12]. As the main component, $(\text{Mg,Fe})\text{O}$ has been a subject of interest including its end-member FeO and MgO.

The magnesium end-member **MgO** crystallizes in the NaCl B1 structure at ambient

conditions. The high pressure phase of MgO is CsCl B2 structure and it was found that this structure gives a large decrease in viscosity compared to the B1 structure [13]. The shock compression study of MgO show the B1-B2 phase transition at a pressure above 400 GPa [14]. This result was confirmed with the recent study combined with X-ray diffraction (XRD) showing the B1-B2 structural phase transition at a pressure of 397 to 425 GPa and a temperature of approximately 9700 K [15]. Furthermore, the B2 structure of MgO was found to remain stable until 900 GPa [16]. These pressure ranges are expected to occur in $5M_E$ super-Earths or larger objects [2].

The FeO end-member undergoes various phase transitions under high pressure. Like MgO, the low pressure modification at low temperatures is the B1 phase. The B1 structure in FeO changes to the distorted rhombohedral structure (rB1) at approximately 16 GPa and 300 K and changes back to the B1 structure at approximately 45 GPa [17][18]. It was found that the B1 structure was stable over the pressure and temperature range of the Earth's lower mantle [19][20]. At the pressure of 110 to 150 GPa and the temperature of 1400 to 1900 K, the B1 structure undergoes a phase transition to the NiAs B8 structure [20]. The B1-B2 transition of FeO occurs at lower pressures than in MgO: it was found at above 240 GPa and 4000K [21]. Here, the density increase was 2 percent[21]. The stability of the B2 structure was observed above 300 GPa [22]. The melting curve of FeO was determined up to 77 GPa and 3100 K [23]. The liquid FeO was recently studied from the pressure of 13 GPa (2600 K) to 85 GPa (3800 K) [24]. The FeO phase diagram under high pressure representing the crystal structures of FeO polymorphs under high pressure is shown as Figure 1.2. Other than structural transition, the electronic transition of FeO B1 structure has been investigated. The transition from insulator to metal phases without structural transition was found at 70 GPa and 1900 K in diamond anvil cell (DAC) experiments [25]. This result of insulator-metal transition is similar to what was found in a shock compression study that measured a decrease in electrical resistivity along the Hugoniot at pressures above 72 GPa [26].

MgO and FeO can form a complete solid solution (**Mg,Fe**)O. Since (Mg,Fe)O is a main composition of the Earth's lower mantle and expected to play the same role in super-Earths, its physical and electrical properties control and affect the whole mantle. The knowledge of the stability and properties of (Mg,Fe)O at Earth's lower mantle conditions is thus of fundamental importance. In early DAC experiments at 85 GPa and 1000 K, $(Mg_{0.80}, Fe_{0.20})O$, $(Mg_{0.60}, Fe_{0.40})O$, and $(Mg_{0.50}, Fe_{0.50})O$ were firstly found to decompose into Fe-rich and Mg-rich oxide components [27][28]. This decomposition was also observed afterwards in

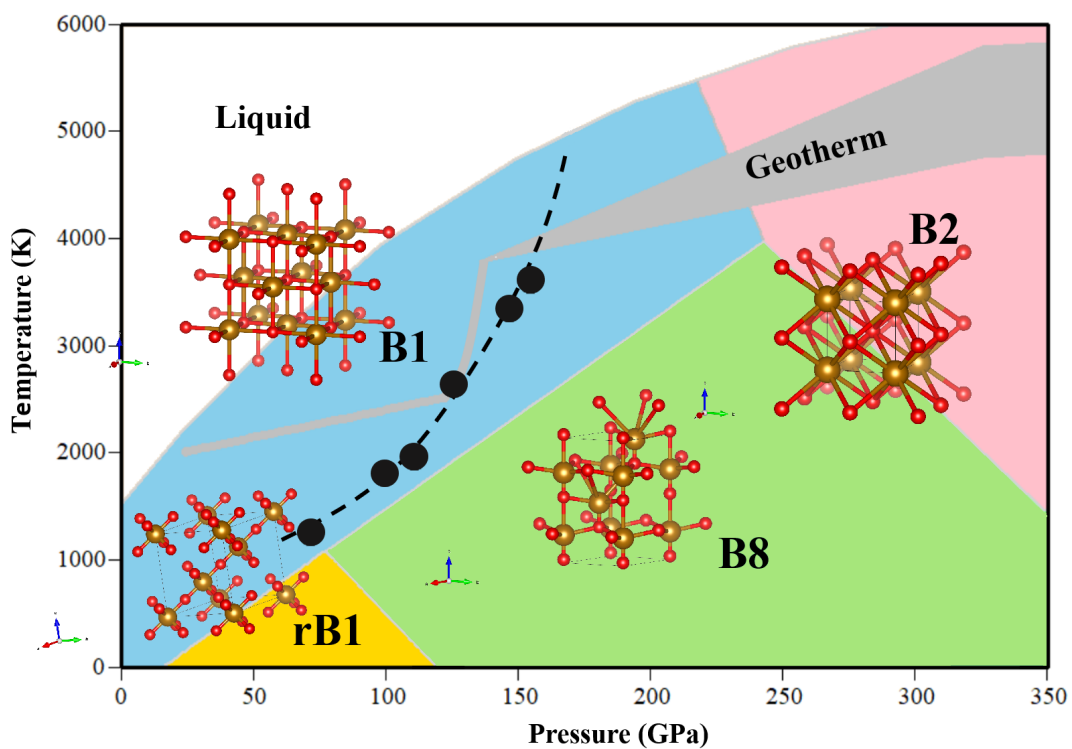


Figure 1.2: Phase diagram of FeO consisting of the high pressure polymorphs of FeO that are B1 (NaCl), B8 (NiAs), B2 (CsCl) and rB1 structures. Pressure and temperature are estimated and modified from the literature [22]. The filled black circles represent results from the shock compression experiments [26].

DAC experiments of $(\text{Mg}_{0.05}, \text{Fe}_{0.95})\text{O}$, but not observed in $(\text{Mg}_{0.20}, \text{Fe}_{0.08})\text{O}$ [29]. However, other DAC studies found no decomposition in $(\text{Mg}_{0.39}, \text{Fe}_{0.61})\text{O}$ and $(\text{Mg}_{0.25}, \text{Fe}_{0.75})\text{O}$ [30]. The shock compression of $(\text{Mg}_{0.60}, \text{Fe}_{0.40})\text{O}$ also showed no phase transition along its Hugoniot up to 200 GPa [31]. The spin crossover of Fe^{2+} in $(\text{Mg,Fe})\text{O}$ has been also a subject undergoing intense study. The change of 4 to 5 percent in volume induced by the spin transition of $(\text{Mg,Fe})\text{O}$ was reported [32]. Several studies of various compositions of $(\text{Mg,Fe})\text{O}$ showed that the spin crossover from high-spin to low-spin state occurs at approximately 40 to 60 GPa (e.g. [33][34][35][36][37][38][39]). Experiments on $(\text{Mg}_{0.8}, \text{Fe}_{0.2})\text{O}$ in a dynamic DAC showed a softening of the bulk modulus which was interpreted to origin from an iron spin transition. The Fe content in $(\text{Mg,Fe})\text{O}$ will affect the magnitude of the softening. This behaviour could be observed through seismic data [40]. A recent study showed that $(\text{Mg,Fe})\text{O}$ with mixed spin state dominates the Earth's lower mantle at a depth below 1000 km [41].

In contrast to FeO and MgO , the data of $(\text{Mg,Fe})\text{O}$ at ultra-high pressure i.e. more than 200 GPa is very limited. The knowledge of physical properties and phase stability of $(\text{Mg,Fe})\text{O}$ at the pressure-temperature conditions relevant to a super-Earth's interior is crucially important for developing and refining the planetary models.

1.3 Dynamic compression experiments

To simulate the relevant conditions inside super-Earths, one of the promising methods is dynamic compression including shock compression and ramp compression. Early researches of shock compression were performed with the gas-gun methods. These methods basically use a piston to force a light gas through a gun barrel that contains a projectile. The projectile is accelerated and hits a target inducing a high-pressure shock wave in the target material. In 1970s, the first shock compression generated by lasers was demonstrated at the time that the large laser facilities were established. Instead of using a projectile, a laser beam irradiates on a target, which consists of an ablator layer, to drive a shock wave into a target material. The first shock-compression experiment performed a strong laser-driven shock on aluminium and produced pressures of 0.6 and 1.8 TPa [42]. Ramp compression, which gives access to lower temperature paths compared to shock compression, have been also developed and performed using high power lasers [43].

Laser-driven dynamic compression techniques have become dominant in the present days as they provide higher pressures and repetition rates [44]. Several large-scale laser

facilities have provided platforms for dynamic compression experiments such as the National Ignition Facility (NIF), the OMEGA laser facility, the LULI2000 facility, and the Laser Mégajoule (LMJ). The laser energies ranging from a few kJ to MJ can be reached in these facilities. Other than large laser facilities, dynamic compression experiments are also conducted at large-scale X-ray facilities. The maximum laser energy up to 100J can currently be delivered among these facilities. The X-ray brilliance, which is defined as the number of photons emitted from a source per unit time, unit solid angle, unit area and unit bandwidth [45], and coherence are crucial for performing dynamic compression experiments. For example, high-compression states require a high laser intensity, which is achieved by high power laser focused on a small driven area: a small spot-size and divergence of X-ray beams is required to study the probed area. The synchrotron radiation facilities and the X-ray free-electron laser facilities (XFELs) integrated with a high power laser for dynamic compression experiments are the High Power Laser Facility (HPLF) at the ID24 beamline of the European Synchrotron Radiation facility (ESRF) [46], the Dynamic Compression Sector (DCS) of the Advanced Photon Source (APS) [47], the Matter in Extreme Conditions (MEC) instrument of The Linac Coherent Light Source (LCLS) [48], the BL3-EH5 experimental platform of the SPring-8 Angstrom Compact Free Electron Laser (SACLA) [49], and the High-Energy Density (HED) scientific instrument at the European XFEL [50][51]. Apart from laser energies and achievable pressures, one of the main difference between conducting dynamic compression experiments at large-scale laser facilities and synchrotron or XFEL facilities is X-ray time structures. X-rays at laser facilities are typically generated by illuminating a short-pulse laser on a backlighter target, such as Cu, Fe and V, to produce a few ns X-ray pulse duration. Synchrotron facilities can generally provide an X-ray pulse duration of 100 ps, while XFELs can deliver less than 100 fs X-ray pulse. This has to be considered for designing whether dynamic compression states can be hold during X-ray probing times.

Dynamic compression experiments are combined with X-ray techniques to probe material properties under dynamic compression. The techniques include XRD, X-ray absorption, and X-ray emission spectroscopy to review structural and electronic phase properties of materials under dynamic loading. Other than X-ray methods, other diagnostics such as Velocity Interferometer System for Any Reflector (VISAR) [52] are also performed in dynamic compression experiments. This technique was developed and used for pressure measurements during the shock propagation. Another diagnostic is pyrometry for thermal emission measurements that can be used for constraining temperature in shock compres-

sion experiments.

One of the major limitations of dynamic compression is rapid time scale [44]. Therefore, equilibrium states may not be reached and processes that need longer time such as chemical reactions may not occur [44]. In addition, laser-driven dynamic compression produces high strain rates and uniaxial loading causing non-hydrostatic conditions. These may result in a of phase transition with respect to static pressure and temperature conditions such as in Bi [53]. Therefore, understanding these effects on compression paths and final states are important for comparing to the results from static DAC compression that are more hydrostatic and to materials in planetary interiors.

1.4 Motivation and goals of this study

As (Mg,Fe)O has been considered as one of the major phases of the Earth's and super-Earth's mantles, the knowledge of physical properties and phase stability at high pressure-temperature conditions being comparable to these planetary interiors are particularly important for understanding their structure and formation. (Mg,Fe)O and its end-member FeO have been the subjects of intensive investigation including shock compression studies. Previous researches show the shock equation-of-state (EoS) of (Mg,Fe)O and FeO up to 200 GPa [26][31][39]. However, structural phases of FeO and (Mg,Fe)O along their Hugoniot have not been experimentally investigated until now. The liquid-solid boundary and solid-solid phase transition such B1 to B2 phase transition of (Mg,Fe)O also remain unclear. These data are crucially important for developing and refining the planetary models.

This study aims to investigate the structural phase stability of FeO as well as (Mg,Fe)O solid solution along their Hugoniot to above 200 GPa. The pressure and temperature conditions were achieved by shock compression experiments. At high pressures, the observation of the solid-liquid and the solid-solid phase transitions such as the B1-B2 phase transition is one of the objectives of this study. The other objective is to explore the effects of Fe-Mg substitution on (Mg,Fe)O phase behavior. This was achieved by performing shock compression experiments of (Mg,Fe)O with various composition ranging from (Mg_{0.2}, Fe_{0.8}) to (Mg_{0.9}, Fe_{0.1}).

Apart from that, this thesis includes the study of the slurry target behaviors under shock loading. Slurry target is one of the methods to prepare suitable targets of powder samples for dynamic compression experiments. However, there has never been a direct Hugoniot

EoS measurement from the experiments and the calculated Hugoniot of slurry targets has been validated only up to 100 GPa [54]. Therefore, the shock EoS of slurry (Mg,Fe)O at a pressure higher than 100 GPa is aimed to obtain from the experiments.

In this thesis, synthesis and preparation of (Mg,Fe)O for shock compression experiment is described in Chapter 2. Chapter 3 presents fundamental methods of shock compression including the essential diagnostic VISAR. This chapter also includes the two experimental setups and hydrodynamic simulation, which is an important tool for experimental design. Results of FeO and (Mg,Fe)O from the shock compression experiments are attached in Chapter 4 and Chapter 5, respectively. Chapter 6 includes conclusion and outlook of this study.

Chapter 2

Synthesis and Preparation of (Mg,Fe)O

(Mg,Fe)O originated from the Earth's lower mantle are found as inclusions in deep-earth diamonds [12]. This mineral was also found in meteorites [55][56] but does not occur in large quantities on the Earth's surface. Thus, access to natural samples is very limited. In this study, two methods of (Mg,Fe)O synthesis were implemented. This chapter includes the description of both methods to synthesize polycrystalline (Mg, Fe)O , i.e. physical vapor deposition (PVD) and gas mixing furnace techniques in Sections 2.1 and 2.2, respectively. Characterization of the samples was performed by energy-dispersive X-ray spectroscopy (EDS) and X-ray diffraction (XRD). In addition, the processes for preparing slurry targets used for dynamic compression experiments are presented in Section 2.3.

2.1 Physical vapor deposition (PVD)

Physical vapor deposition (PVD) is a method to deposit a thin-layer material on a substrate under vacuum. The terms of PVD describe a process in which a material transforms from a condensed phase to a vapor and then to a thin layer of a condensed phase [57][58]. In this study, the PVD deposition was performed at the Institute of Mineralogy, Physics of Materials and Cosmochemistry (IMPMC) of Sorbonne University in Paris, France. While PVD is an established technique, the deposition of oxides with mineral compositions is not and requires the development of suitable recipes. The schematic of the PVD processes and the PVD machine are depicted in Figure 2.1. The setup consists of several components: a vacuum chamber with a pump to ensure and maintain the vacuum conditions, Mg and Fe target-cathodes connected to magnetrons, a gas injection system, and substrates located on a rotating holder.

PVD processes require a high vacuum to achieve deposition and avoid contamination,

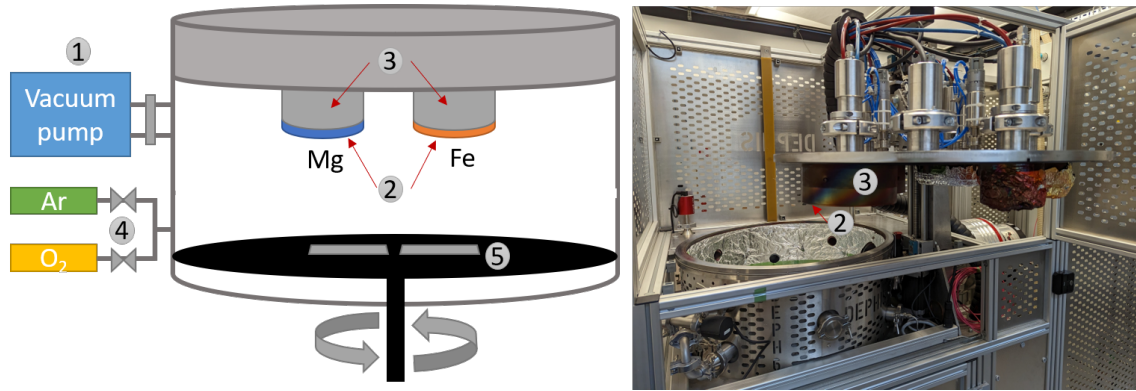


Figure 2.1: Schematic diagram of the PVD system and the PVD machine at IMPMC: (1) vacuum pump, (2) Fe and Mg cathodes, (3) magnetrons, (4) a gas injection system, and (5) substrates on a rotating holder.

so the chamber was pumped down to the pressure range of 10^{-6} to 10^{-7} mBar. To prepare for deposition, Ar gas and O_2 gas were injected into the chamber and substrates, which were a silicon wafer and a glass slide, were placed in the rotating holder with a rotation speed of 6 rounds per minute. The first step of PVD is the ionization of the Ar gas that creates positive argon ions Ar^+ . This process is initiated by applying the potential difference between the cathodes and the substrates: electrons in the Ar gas are accelerated away from the cathodes, causing collision to the nearby atoms and ionization. To increase the probability of ionizing interactions, the magnetrons behind the target cathodes are used for creating electric and magnetic fields that capture the electrons in close vicinity to the target cathodes. The Ar^+ collides with the target cathodes and the Mg and Fe atoms are ejected into the vacuum. At the same time, O_2 also reacts with the Fe and Mg atoms to create oxides. (Mg,Fe)O were deposited on the substrates along these processes. During deposition, the pressure inside the chamber increased to 10^{-3} mBar.

To acquire Mg-rich (Mg,Fe)O, the voltage power supplied to the Fe cathode and the O_2 gas flow rate were optimized. Test runs were performed, and the samples were then characterized by EDS and XRD to obtain information on composition and structure. The power on the Mg cathode was set to the maximum power at 550W for all the test runs, while the power on the Fe cathode was optimized in the range of 200 to 400W. The flow rate O_2 was adjusted between 9 and 12 sccm (or cm^3min^{-1}). The deposition times for all the test runs were 90 to 180 minutes.

The elemental analysis was performed for the test runs at the Scanning Electron Microscope (SEM)-Focused Ion Beam (FIB) microscopy facility of the IMPMC. The Zeiss Ultra55 with high-resolution Schottky thermal field emission gun (Schottky SEM-FEG) with the Bruker QUANTAX EDS-detector was used. Figure 2.2 shows the elemental anal-

ysis of Fe-Mg-O from the EDS as a function of power on the Fe cathode and O₂ flow-rates performed at the IMPMC. At higher power, a greater quantity of Fe was included in the sample: with a power of more than 250W, Fe dominated the sample composition with respect to Mg. Thus, the power on the Fe cathode was chosen to be less than 250W or at 200W for the deposition of Mg-rich (Mg,Fe)O. The O₂ flow-rates were also optimized by fixing the power on the Fe cathode to 200W. The results suggest that a higher amount of Mg was achieved with a higher O₂ flow rate. In contrast, the oxygen amount did not show significant differences when changing O₂ flow-rates in the range of 9 to 12 sccm.

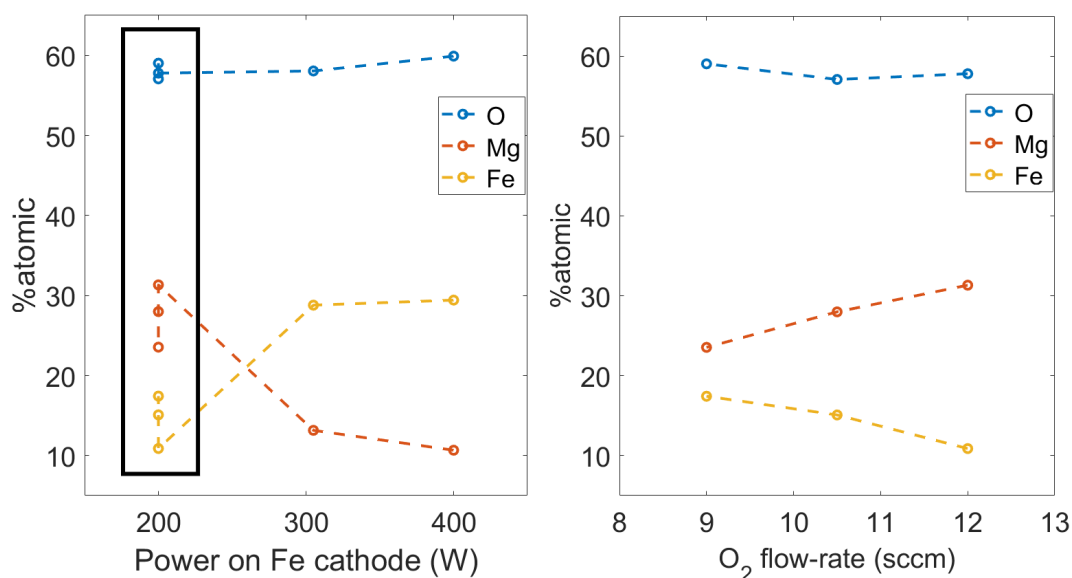


Figure 2.2: Elemental analysis of Fe-Mg-O from the EDS as a function of power on the Fe cathode (left) and the O₂ flow-rates at the power on Fe cathode of 200W corresponded to the black rectangle of the left plot (right).

In addition to EDS, XRD was performed for all test samples to identify the deposited compounds at the X-ray Diffraction platform of the IMPMC. The PANALYTICAL X'pert Pro Multi-Purpose Diffractometer (MPD) was used with Co anode, where the X-ray energy is 6.9 keV. The measurement was done in Bragg-Brentano geometry and the measurement time duration was one hour for each sample. Most of the XRD peaks were identified, as shown in Figure 2.3: there are Fe₂O₃ and Si (from a silicon wafer). The broad feature at $2\theta \approx 50^\circ$ (in the orange rectangle) is supposedly (Mg,Fe)O. The intensity of this feature varies with different flow rates of O₂ and disappears when the O₂ flow rate is equal to 12 sccm. This result suggests that the highest possible O₂ flow rate that provides the broad feature, i.e. to get Mg-rich (Mg,Fe)O, is 10.5 sccm. Therefore, the optimized parameters for the deposition are a Fe cathode power of 200W and O₂ flow-rate of 10.5 sccm.

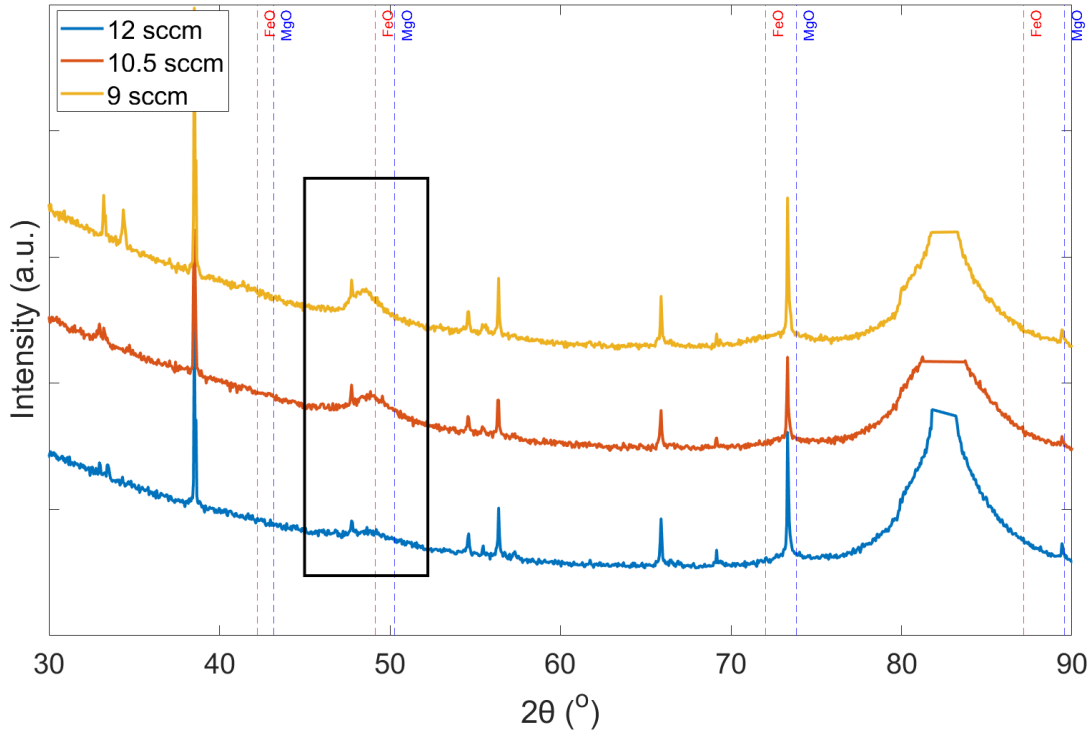


Figure 2.3: XRD of the samples deposited with power on the Fe cathode of 200W and O_2 flow-rates of 9, 10.5, and 12 sccm. The black rectangle corresponds to $(Mg,Fe)O$.

The deposition rate was calculated from the obtained thickness of the test run and used to estimate the deposition time. At a power of 200W on the Fe cathode, the deposition rate is as low as approximately 3 nm per minute. Thus, to obtain the required thickness of 10 μm , the deposition time was expected to be more than 50 hours. Moreover, the deposition time has to be divided into several cycles to keep the temperature sufficiently low. In this study, it was 17 cycles and the total deposition time was 41 hours 26 minutes. The process was stopped earlier than expected because of a damage to the Mg cathode. The thickness of the sample was in the range of 9 to 11 μm .

XRD of the $(Mg,Fe)O$ final deposition was measured for 3 hours 40 minutes at the IMPMC as shown in Figure 2.4. The results show that the XRD of the final deposition is clearly $(Mg,Fe)O$. There are some additional peaks compared to the XRD of $(Mg_{0.9}, Fe_{0.1})O$ and $(Mg_{0.6}, Fe_{0.4})O$ from reference [59]. The one at approximately 40° is identified as Mg. The deposition of pure Mg could occur during the last cycle, in which damages to the Mg cathode were observed. Another peak is labeled as BG (background): it could arise from the glass that is used as deposition substrate. The XRD peak position is more similar to $(Mg_{0.9}, Fe_{0.1})O$: additional EDS was performed to determine the composition.

Apart from the XRD measurement, the SEM and the EDS measurement were per-

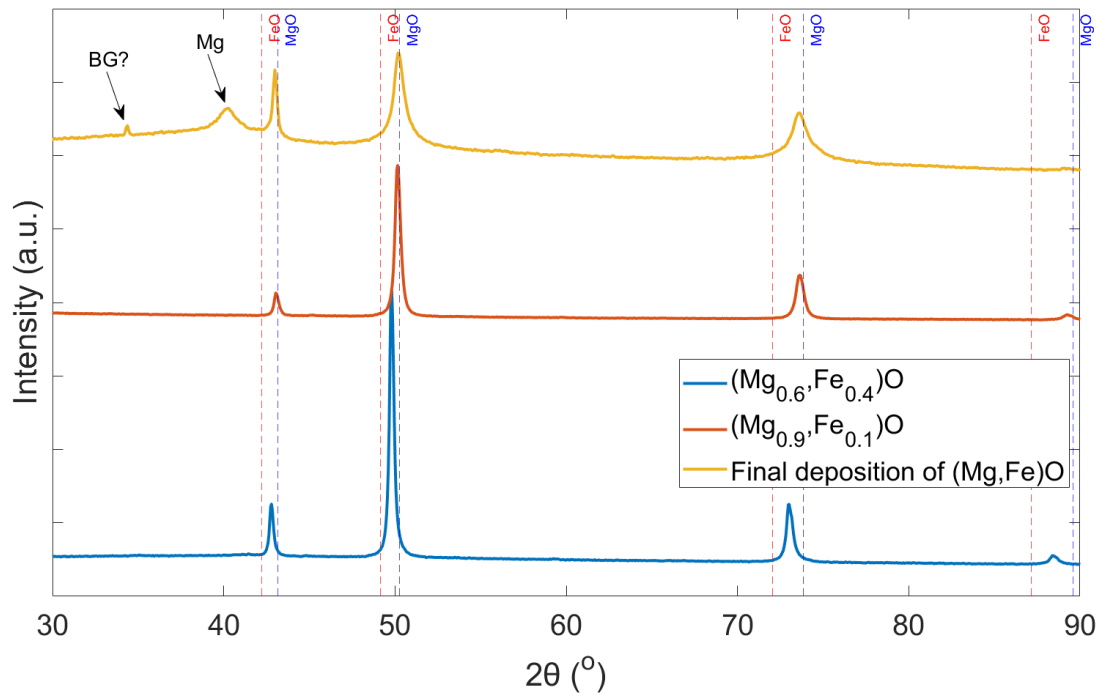


Figure 2.4: XRD of the final sample compared to $(\text{Mg}_{0.9}, \text{Fe}_{0.1})\text{O}$ and $(\text{Mg}_{0.6}, \text{Fe}_{0.4})\text{O}$ from the reference [59].

formed for the final deposition by using the FEI Quanta 650 FEG at the Sample Environment and Characterization (SEC) group of the European XFEL. Figure 2.5 (left) shows an image of (Mg,Fe)O final deposition taken by shot with 7 kV. The surface of the sample is quite homogeneous in the large area. The texture is also similar to Figure 2.5 (right), which is FeO and Fe_2O_3 . However, some darker and brighter parts with different textures are observed. Elemental analysis by EDS shows that the average atomic percentage of O, Mg, and Fe is 23-31%, 61-65%, and 9-11%, respectively: the EDS results suggest that the composition of (Mg,Fe)O is approximately $(\text{Mg}_{0.85}, \text{Fe}_{0.15})\text{O}$. The Mg and Fe are consistent for all the areas including brighter and darker parts. The O atomic percent is significantly lower than expected for (Mg,Fe)O and fluctuates. This was also observed in a PVD sample of FeO and Fe_2O_3 : the elemental composition of Fe and O are 57 to 62 at% and 37 to 42 at%, respectively.

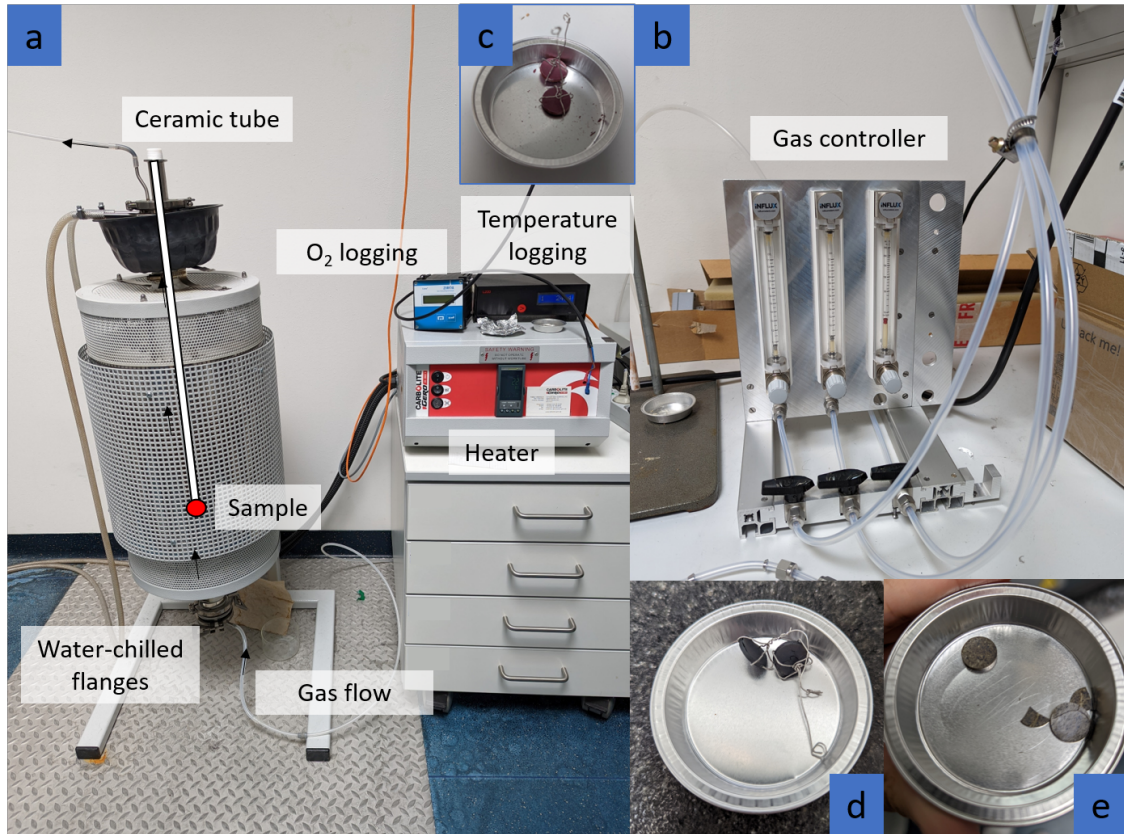


Figure 2.6: The gas mixing furnace experiment at the Institute of Geosciences of the University of Potsdam: (a)-(b) the equipment of the vertical gas mixing furnace including heater, ceramic tube, water-chilled flanges (top and bottom), logging units for temperature and oxygen fugacity, and gas controller, (c) mixture before putting in the furnace, (d) $(\text{Mg}_{0.6}, \text{Fe}_{0.4})\text{O}$ pellets, and (e) $(\text{Mg}_{0.9}, \text{Fe}_{0.1})\text{O}$ pellets.

took approximately 48 hours to obtain (Mg,Fe)O powder.

The synthesized powder of $(\text{Mg}_{0.9}, \text{Fe}_{0.1})\text{O}$ and $(\text{Mg}_{0.6}, \text{Fe}_{0.4})\text{O}$ is presented as Figure 2.7 $(\text{Mg}_{0.9}, \text{Fe}_{0.1})\text{O}$ is a green powder, while $(\text{Mg}_{0.6}, \text{Fe}_{0.4})\text{O}$ is darker due to a greater amount of Fe proportion. The XRD measurement was performed to identify phases of the synthesized powder. The PANalytical Empyrean diffractometer equipped with a Cu tube at the Institute of Geosciences of the University of Potsdam was used. The measurement was done in the Bragg-Brentano mode where the X-ray energy is 8.1 keV and the measurement time lasted one hour. The synthesis products were characterized by XRD compared to the reference [59] as shown in Figure 2.7. The results show that the synthesized powder are $(\text{Mg}_{0.9}, \text{Fe}_{0.1})\text{O}$ and $(\text{Mg}_{0.6}, \text{Fe}_{0.4})\text{O}$ without contamination. From the XRD, reflections from (200) plane of $(\text{Mg}_{0.9}, \text{Fe}_{0.1})\text{O}$ and $(\text{Mg}_{0.6}, \text{Fe}_{0.4})\text{O}$ are at approximately 42.76° and 42.44° , which corresponds to the volume of 75.5 \AA^3 and 77.1 \AA^3 , respectively. The density of $(\text{Mg}_{0.9}, \text{Fe}_{0.1})\text{O}$ and $(\text{Mg}_{0.6}, \text{Fe}_{0.4})\text{O}$ were calculated to be 3.82 g/cm^3 and 4.55 g/cm^3 .

Table 2.1: Amount of Fe_2O_3 and MgO used for synthesis of $(\text{Mg}_{0.9}, \text{Fe}_{0.1})\text{O}$ and $(\text{Mg}_{0.6}, \text{Fe}_{0.4})\text{O}$ powder in this experiment.

	$(\text{Mg}_{0.9}, \text{Fe}_{0.1})\text{O}$		$(\text{Mg}_{0.6}, \text{Fe}_{0.4})\text{O}$	
	Fe_2O_3 (159.7 g/mol)	MgO (40.3 g/mol)	Fe_2O_3 (159.7 g/mol)	MgO (40.3 g/mol)
Amount (mol)	0.05	0.90	0.20	0.60
Calculated weight (g)	0.1996	0.9068	0.7984	0.6046
Actual weight (g)	0.1990	0.9072	0.7953	0.6025

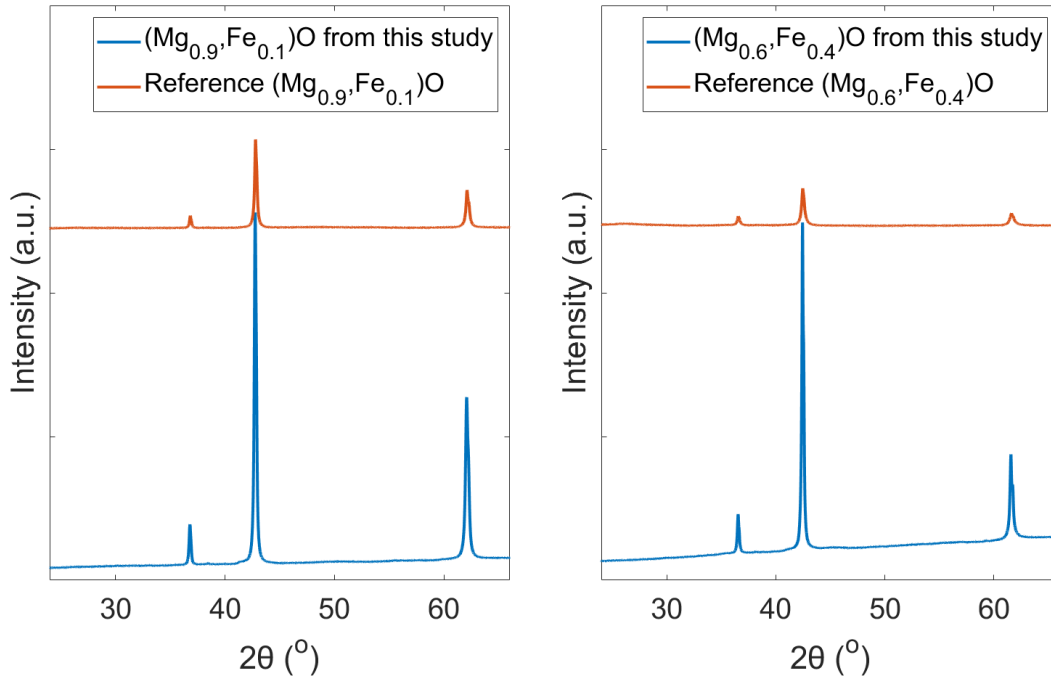


Figure 2.7: XRD of the synthesized powder of $(\text{Mg}_{0.9}, \text{Fe}_{0.1})\text{O}$ and $(\text{Mg}_{0.6}, \text{Fe}_{0.4})\text{O}$ compared to the reference [59].

2.3 Slurry-target preparation

Slurry targets are powder samples that are immersed in epoxy. These targets are one approach to prepare powder samples when the large crystals are not available to use for dynamic compression experiments, which require a sample as a solid thin layer consisting in a multi-layer target. This type of target was introduced to use in shock compression experiments in 2022 for NaCl and the XRD showed consistency with the results from single crystals and slurry targets for pressures up to 100 GPa [54]. In addition, dynamic compression experiments using high-repetition rate lasers require a large amount of targets to adequately supply. For example, Dipole-100x provided by HIBEF (Helmholtz International Beamline for Extreme Fields) User Consortium at the High Energy Density (HED) scientific instrument at the European XFEL can be operated with a repetition rate of up

to 1-10 Hz demanding thousands targets per hour. Slurry targets have become one of the alternative choices due to their capability to use as tape targets [61][54] and simple preparation methods compared to other target fabrication methods.

In this study, the recipe to prepare slurry targets was adapted from reference [54]. (Mg,Fe)O powder synthesized in section 2 and from the reference [59] were ground in a zirconia mortar for 30 minutes and baked in an oven overnight to remove any moisture. To prepare a glue for a mixture, Araldite2020 glue with a density of 1.12 g/cm^3 was put under vacuum to remove all air bubbles for approximately 10 minutes. The powder and glue were mixed as 1:1 by volume. The mixture was either smeared between a black Kapton and a Teflon layer or between two Teflon layers and was rolled into a planar film with a rolling-mill machine. As shown in Figure 2.8, two thick (200 μm) Teflon sheets were used for preventing a black Kapton and a thin Teflon from curling during rolling. The sample was then put between two glass slides and on a hot plate with $60 \text{ }^\circ\text{C}$ for 90 minutes before leaving it overnight: a rolling weight was also placed on the stack to ensure a homogeneous thickness.

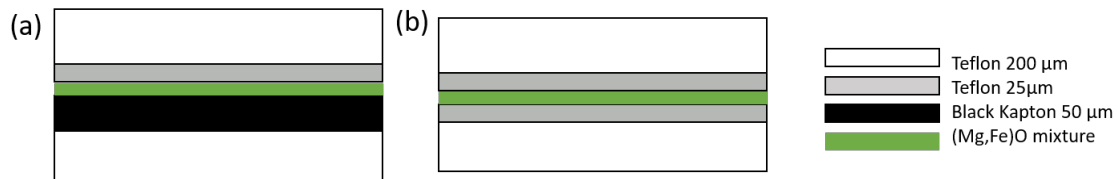


Figure 2.8: Configuration of the samples to put in a rolling-mill machine for (a) a slurry with black Kapton and (b) free-standing slurry.

The slurry targets were checked under a microscope, as shown in Figure 2.9. There were still a few voids in a sample, but most areas had an even and regular surface. However, the thickness of a whole piece was found to be inhomogeneous. To get the precise thickness for each target, the thickness of every single piece was measured before the experiment. In addition, the slurry target was imaged by the SEM at the SEC group of the European XFEL. The result in Figure 2.9 shows that the grain size of the powder in the slurry is below $1 \mu\text{m}$. Furthermore, the XRD measurement was performed for the slurry at the Institute of Geosciences of the University of Potsdam, as shown in Figure 2.10. The results show only the XRD peaks from (Mg,Fe)O powders with no contamination.

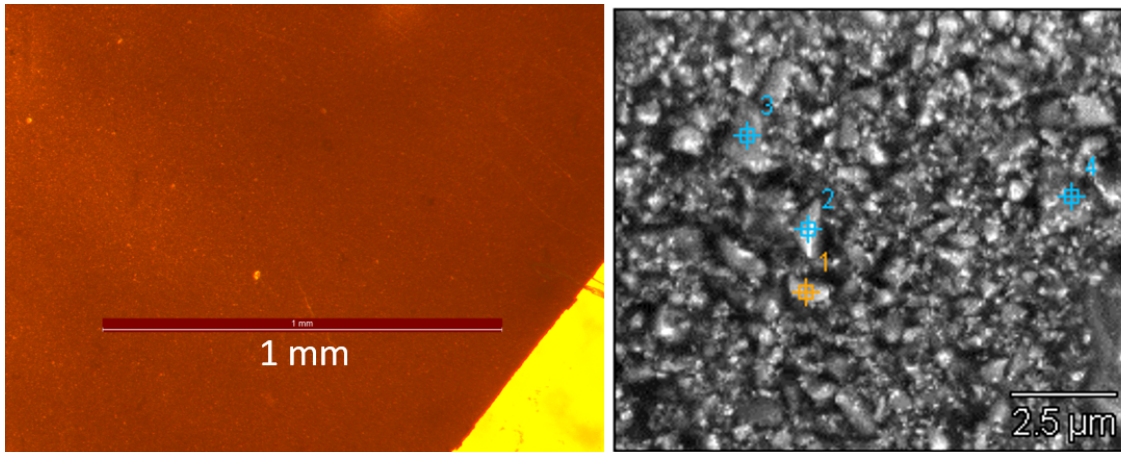


Figure 2.9: Slurry samples imaged by the microscope with 1-mm resolution (left) and the SEM with 2.5- μm resolution (right).

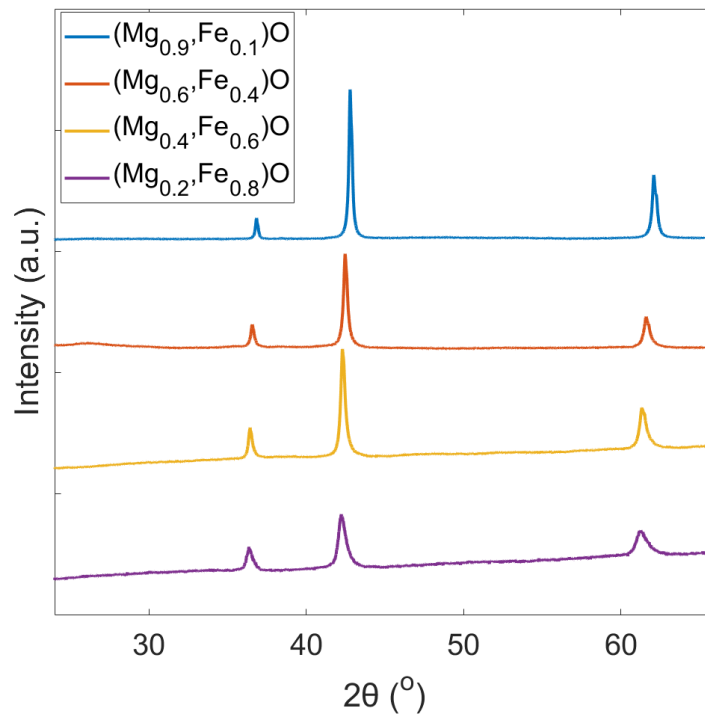


Figure 2.10: XRD of $(\text{Mg}_{0.9}, \text{Fe}_{0.1})\text{O}$, $(\text{Mg}_{0.6}, \text{Fe}_{0.4})\text{O}$, $(\text{Mg}_{0.4}, \text{Fe}_{0.6})\text{O}$, and $(\text{Mg}_{0.2}, \text{Fe}_{0.8})\text{O}$ from the slurry targets.

Chapter 3

Experimental Methods of Shock Compression

In this chapter, the methods of shock compression are described starting from fundamental concepts of shock wave propagation in materials in Section 3.1. Section 3.2 introduces one of the important optical diagnostics used in shock compression that is Velocity Interferometer System for Any Reflector (VISAR). It includes the experimental principles and interpretation of VISAR data. The two experimental stations at the Matter in Extreme Conditions (MEC) instrument of the Linear Coherent Light Source (LCLS) and the LULI2000 facility which were used in this study are presented in Sections 3.3 and 3.4. These descriptions include the experimental setup and target design. Furthermore, hydrodynamic simulations were performed for the experiments to constrain the experimental parameters and understand and constrain the results. These details are included in Section 3.5.

3.1 Fundamental concepts of shock compression

Propagation of a shock wave through a material causes sudden changes of pressure, density, and temperature. To describe the state of the material under shock wave loading, one can consider a scenario as shown in Figure 3.1: a piston moves to the right with a constant velocity U_p while driving a shock wave with a velocity U_s . The states of a gas compressed by a shock wave are suddenly changed to density ρ , pressure P , and internal energy (in energy per unit mass) E , while a gas on the right side of a shock wave front is unperturbed or stays as the initial states ρ_0 , P_0 , and E_0 . The relationship between the states on both sides of a shock wave in a laboratory frame can be described by the Rankine-Hugoniot

equations, where a conservation of mass, momentum, and energy governs the propagation of a shock wave as follows [62][63]:

$$\rho_0 U_s = \rho(U_s - U_p), \quad (3.1)$$

$$P - P_0 = \rho_0 U_s U_p, \quad (3.2)$$

$$E - E_0 = \frac{1}{2}(P + P_0) \left(\frac{1}{\rho_0} - \frac{1}{\rho} \right). \quad (3.3)$$

The initial states of a material have to be known, and the unknown variables are density ρ , pressure P , internal energy of the compressed material E , the shock velocity U_s , and the respective particle velocity of the compressed material U_p . When two variables of the equations are known or measured in an experiment, the others can be solved with equations 3.1, 3.2, and 3.3. However, the temperature is not constrained by these equations: it can be calculated from internal energy E or $E - E_0$ where the heat capacity has to be known along with the equation of state (EoS) [62].

The density of a material under shock loading at the corresponding pressure is one of the characteristic properties, which also include particle velocity, shock velocity, and temperature. These variables can be plotted as the Hugoniot of the material. For example, Figure 3.2 shows the Hugoniot plot in the spaces $(P, 1/\rho)$ and (P, U_p) . It is important to note that the Hugoniot plot is a series of end states of a respective material under shock loading: it is not a thermodynamic path like an isentrope.

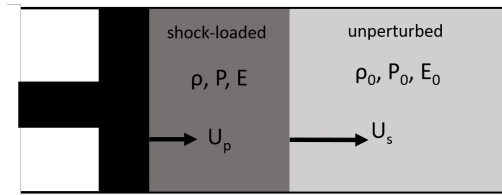


Figure 3.1: Schematic of a shock wave propagation with the velocity U_s in a gas driven by a piston moving with a constant velocity U_p causing the sudden changes of gas density, pressure, and internal energy from ρ_0 , P_0 , and E_0 to ρ , P , and E .

Impedance matching

The next step in studying a material under shock loading is to understand the propagation of the shock wave at an interface of two materials. At the boundary, pressure and particle velocity on both sides have to be continuous or equal during and after the shock propagation. Figure 3.3 shows the situations in which a shock wave travels from material A to material B depending on the shock impedance Z , which is a slope of a straight line be-

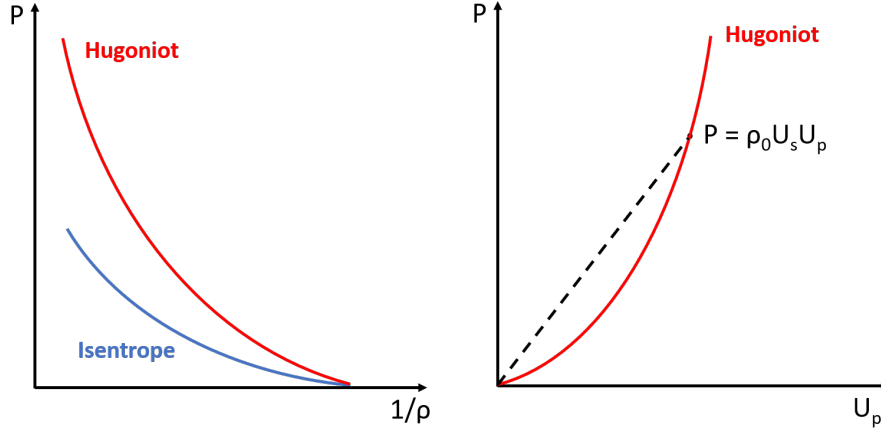


Figure 3.2: Hugoniot of an unspecified material in $(P, 1/\rho)$ space compared to isentrope (left) and (P, U_p) space (right).

tween the initial and final state of a single shock expressed in Figure 3.2 as the following equation:

$$Z = \rho_0 U_s. \quad (3.4)$$

There are two possible cases in which a shock wave propagates from a material A to B.

- If $Z_A < Z_B$ (Figure 3.3(a)), a shock wave of higher pressure transmits to B ($P_B > P_A$) and a shock wave reflects in A at the same pressure P_B . The new state of a material A after the reflected shock wave is calculated based on the initial state $(U_{p,A}, P_A)$. Therefore, the pressure P_B is graphically an intersection of the Hugoniot of a material B (H_B) and (H''_A), which is a mirror reflection of the secondary Hugoniot of a material A (H'_A).
- If $Z_A > Z_B$ (Figure 3.3(b)), a shock wave transmits to B resulting in a lower pressure ($P_B < P_A$) and a shock wave reflects in A at the same pressure. The pressure P_B is obtained from an intersection of the isentrope curve starting from P_A and the Hugoniot of a material B. However, due to an absence of EoS to find a release isentrope of some materials, the mirror Hugoniot in (P, U_p) is sometimes used instead: it is found to be quite accurate for materials A and B with similar shock impedance or a pressure up to 200 GPa [63].

The technique for solving pressures and particle velocity resulting from a shock wave propagation to a material with a different impedance is called impedance matching. This technique has been widely used for EoS measurements. For example, by choosing material A as a standard material in which the EoS or the Hugoniot curve is known like in quartz and sapphire, the Hugoniot curve of an unknown material as a material B can then be

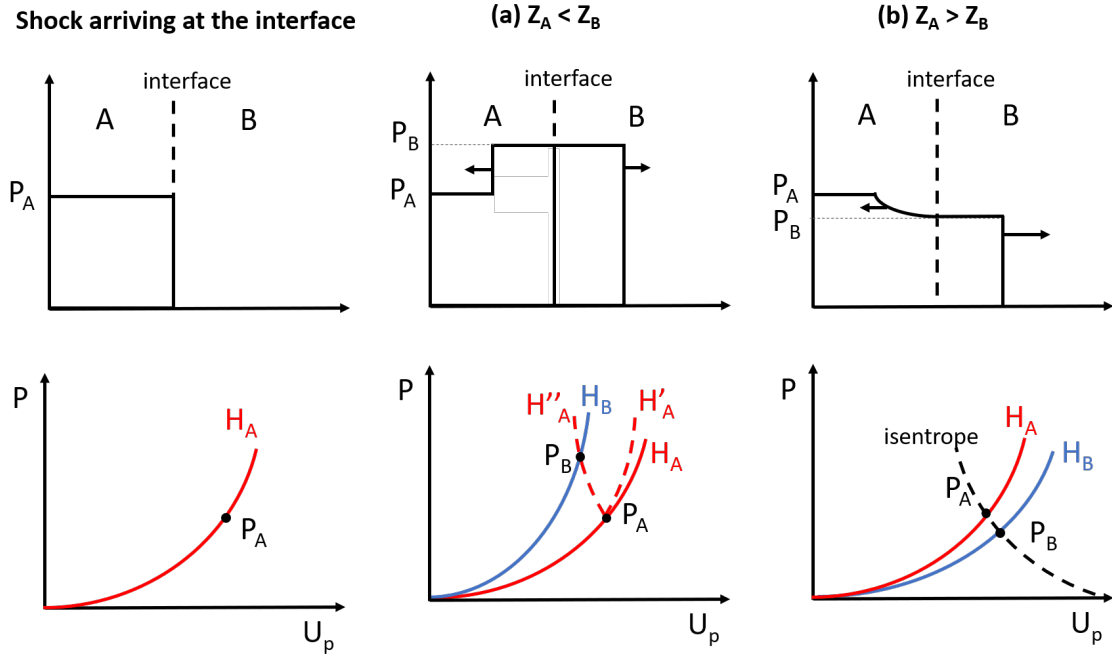


Figure 3.3: Pressure profiles before and after a shock crossing the interface of material A and B when (a) $Z_A < Z_B$ and (b) $Z_A > Z_B$

calculated with the measured particle velocity and shock velocity. In this study, the EoS measurement was also performed for two compositions of slurry (Mg,Fe)O, where their Hugoniot curves are unknown: single crystal quartz was chosen as a standard material. This experiment is described in Section 3.4 and 5.1.

3.2 VISAR diagnostics

VISAR is one of the important tools for measuring pressure in shock compression experiments. This method uses the knowledge of the Doppler effect: a reflected light from a moving surface governed by a shock wave propagation is recorded by an interferometer producing Doppler shifts or fringe shifts as a function of time. The fringe shifts are used for the calculation of the surface velocity and then related to the pressure during shock compression.

A typical interferometer as part of a VISAR system is shown in Figure 3.4. A probed beam is focused on the moving surface of a shocked sample, and a reflected beam is collected by a beam splitter A, which splits the beam into two parts. The two parts are recombined and interfere at a beam splitter B: the interference pattern is recorded by a streak camera. The time delay between the two arms is introduced by insertion of an etalon. After setting an equal path for two arms, an etalon with the thickness h is inserted in front of

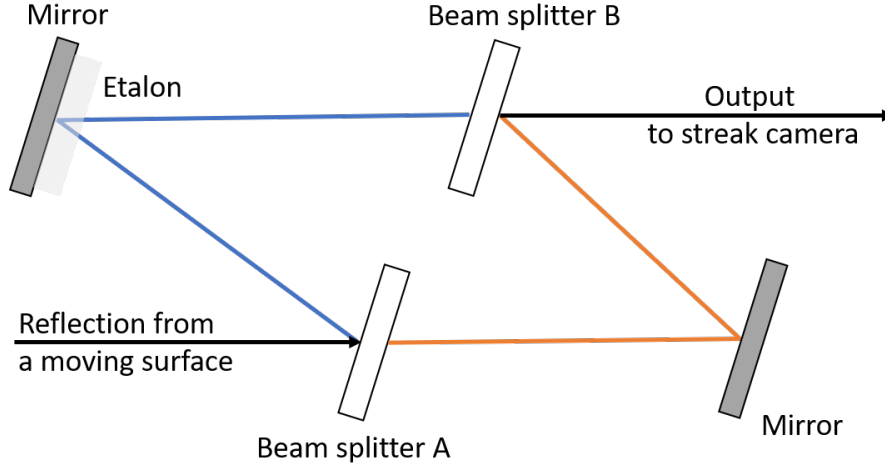


Figure 3.4: Typical configuration of VISAR used for velocity measurement.

a mirror in one arm. The focus is consequently shifted due to the refraction, so the mirror with the etalon has to move further to get an overlap image plane by the distance d :

$$d = h \left(1 - \frac{1}{n_{etalon}(\lambda_0)} \right), \quad (3.5)$$

where $n_{etalon}(\lambda_0)$ is the refractive index of the etalon at the probe wavelength λ_0 . Thus, the total optical time delay τ of the interferometer is calculated as follows:

$$\tau = \frac{2h}{c} \left(n_{etalon}(\lambda_0) - \frac{1}{n_{etalon}(\lambda_0)} \right). \quad (3.6)$$

The thickness and refractive index of an etalon relates to the sensitivity that is often expressed as the velocity per fringe (VPF):

$$VPF = \frac{\lambda_0}{2\tau(1 + \delta)}, \quad (3.7)$$

where δ is a correction term for the chromatic dispersion in the etalon. The VPF is one of input parameters used in VISAR analysis for calculation of the velocity from the fringe shift.

The thicker etalon provides more sensitivity as expressed in equations 3.6 and 3.7, so a lower velocity is required for one fringe-shift. For example, fused-silica etalons with thicknesses of 11.006 and 50.140 mm, when using a probe laser with wavelength of 532 nm, give VPFs of 4.513 and 0.991 km/s, respectively. However, if the thick etalon is used to get high sensitivity or high accuracy, more than one fringe shift can be recorded when the velocity jump is very high. This leads to the difficulty to decide on the surface velocity.

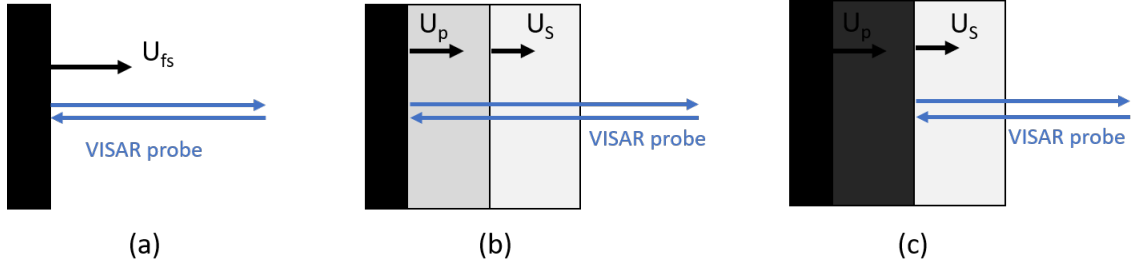


Figure 3.5: VISAR probing on three cases of the moving surfaces under shock-loading: (a) free surface, (b) interface of a transparent standard material and a studied material, and (c) shock front when it become reflective.

Therefore, typically two VISARs with different etalon thicknesses are used to get a unique velocity of a probed surface.

The VISAR can probe different moving surfaces in the sample which depends on target and experimental design and the recorded velocity needs an adjusted interpretation. Figure 3.5 shows three cases that are usually measured by VISAR [64]. The reflection from an interface of a studied material and a free surface shown in Figure 3.5(a) gives a free-surface velocity U_{fs} . It can be related to the particle velocity of the studied material U_p by $U_{fs} = 2U_p$. This is a good approximation for liquids and with up to 3 percent error for solids [65][66]. However, it provides a greater error if the Hugoniot elastic limit (HEL) of the solids is less than 10 percent of the peak pressure [66]. The second case in Figure 3.5(b) is a reflection at the interface of a transparent standard material and a studied material, where the recorded velocity is a particle velocity of the standard material U_p . Figure 3.5(c) shows another case when a transparent material becomes optically reflective during shock loading: the reflection takes place at the shock front itself, so the fringe shifts result from the shock velocity in the material.

An example of VISAR images and the corresponding velocity profile from Neutrino software (Copyright (C) 2013 Alessandro Flacco, Tommaso Vinci All Rights Reserved) are shown as Figure 3.6. Here, the two VISARs with a VPF of 4.513 and 0.991 km/s were performed. The sample configuration is 49- μm parylene-N/ 5- μm FeO/ 200-nm aluminium coating/ 25- μm Sapphire: FeO is the studied material, while sapphire is used as a standard reference material or a pressure window. The thin-layer aluminium is at the interface between FeO and sapphire and serves as a reflecting layer for the VISAR measurement. In this case, the sapphire window was still transparent during shock loading. Thus, the first fringe shift corresponds to the U_p of the sapphire window. At the time of the shock breakout from the sapphire, the second fringe shift is observed. Here, the travel time of the shock wave in a sapphire are also recorded. Furthermore, not only the velocity

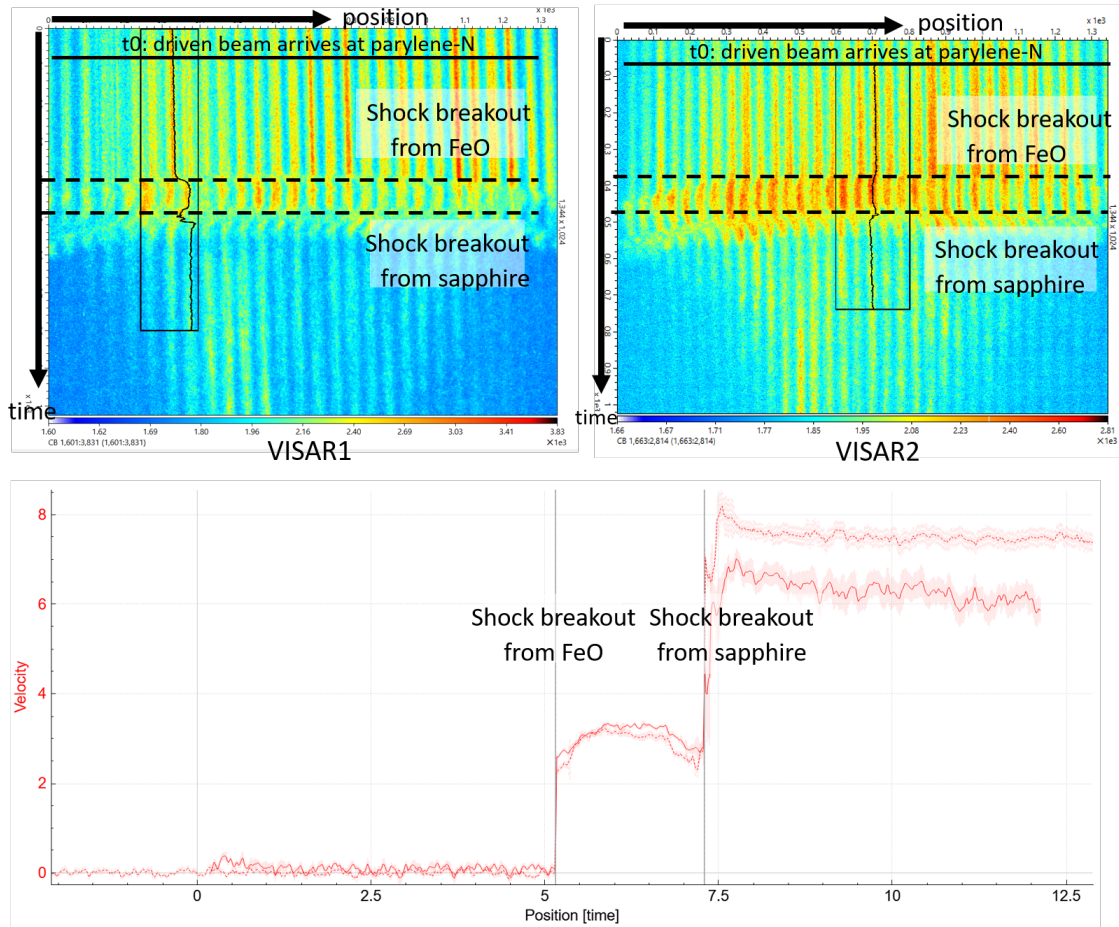


Figure 3.6: VISAR images and the corresponding velocity profiles from Neutrino software from the target parylene-N/FeO/sapphire window. The fringe shifts or velocity jumps were observed at the time when a shock breakout from FeO and Sapphire. The velocity is interpreted as the particle velocity in the sapphire window.

but also the reflectivity changes can be interpreted from the VISAR image.

3.3 Experimental setup at MEC, LCLS

The shock compression experiment of (Mg,Fe)O and FeO was carried out in February 2022 under the proposal LX64 at the MEC instrument at LCLS. This experiment aimed to investigate phase transitions and the solidus-liquidus boundaries of (Mg,Fe)O and FeO along their Hugoniot to megabar pressures. Several compositions of (Mg,Fe)O with different Fe contents ranging from 10% to 80% were used to determine the effects of Fe-Mg substitution on their phase behavior. Additionally, two different target types of physical vapor deposition (PVD) and FeO slurry samples were used to observe the differences and effects on the Hugoniot.

The MEC instrument provides an experimental platform for studying transient mate-

rials under ultrahigh pressure by combining high-power laser with the X-ray free-electron laser (XFEL). Further details of the instrument capabilities at the MEC can be found in the reference [48]. The experimental setup of this study is shown in Figure 3.7. To perform the shock compression experiment, an optical laser with a flat top shape was driven onto a target surface, which is typically a CH ablator layer at the front of the target sandwich. The thermal expansion of the ablator launches a shock wave in the sample that compresses the sample in a very short time. The sample during shock compression was probed by the XFEL at a given time delay. Thus, the states of the samples, i.e. the structure and density in this case, along the Hugoniot were investigated as the X-ray diffraction was measured in transmission mode. The corresponding pressure, particle velocity, and shock velocity were obtained from VISAR measurements.

The long pulse laser system of the MEC, which is a frequency-doubled Nd:glass system with the wavelength of 527 nm, was used as drive laser. The pulse energy was contributed from four-arm combination of lasers and the maximum peak power can be up to 10 GW at a pulse length of up to 10 ns with flat-top shape. The laser can be operated at a rate of one full energy shot per 7 minutes or up to half energy shot per 3.5 minutes. Here the 5-ns flat-top laser pulse was used and it was focused to a spot size of 300 μm diameter. However, as shown in Figure 3.7, the laser pulse used in this experiment was not ideally flat-topped. Therefore, the generated shock waves were not stable, which needs to be taken into account in the data analysis.

The samples during shock compression were probed with two diagnostics: XRD and VISAR techniques. The XRD measurement was performed with X-ray energies of 13 and 17 keV. The X-ray beam was focused to a spot size of 150- and 45- μm diameter, respectively. Four ePix detectors with a 50- μm pixel size were used: the 2θ coverage was approximately 20 to 75 degrees. Two VISAR arms with a probe laser wavelength of 532 nm were used for this experiment. The thickness of the etalons was chosen to be either 25.034 or 50.140 mm for VISAR1 which results in a corresponding sensitivity of 1.984 or 0.991 km/(s · fringe), respectively. An etalon with the thickness of 11.006 mm, corresponding to a sensitivity of 4.513 km/(s · fringe), was inserted for VISAR2. The Hamamatsu C7700s optical streak camera was used for recording the VISAR data.

The targets were designed on the basis of hydrodynamic simulation using the achievable parameters at MEC. As shown in Figure 3.7, the general target configuration was a sandwich of CH ablator / sample / sapphire window. The CH ablator layer was either 50- μm black Kapton or 49- μm parylene-N. As mentioned above, two types of the sam-

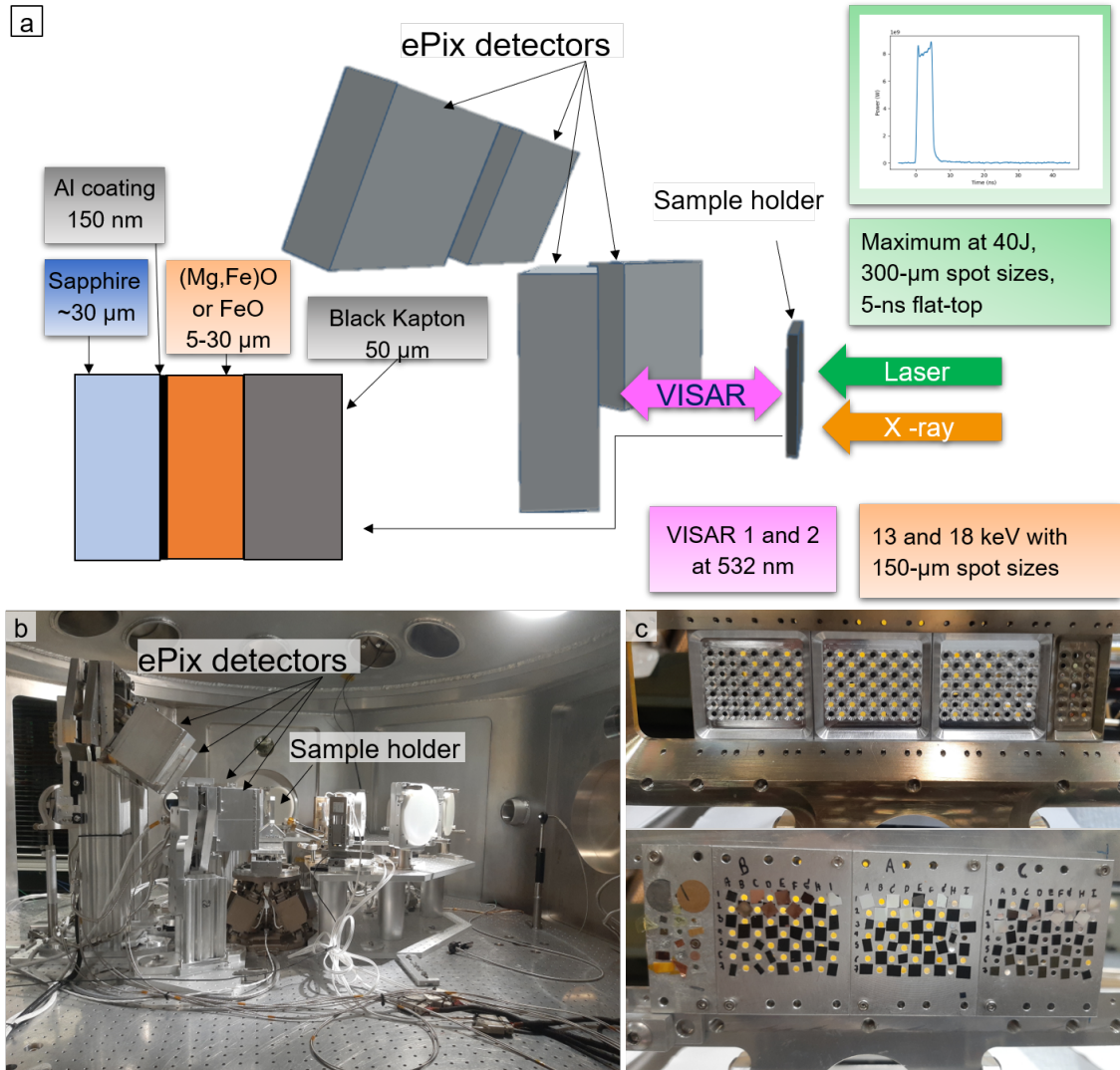


Figure 3.7: Experimental setup at the MEC instrument of the LCLS: (a) schematic of the experimental setup including target configuration, driven laser pulse-shape, XRD, and VISAR measurement, (b) inside of the target chamber at the MEC experimental hutch, and (c) the target holder viewed from the laser side (top) and VISAR side (bottom).

ples that are slurry and PVD were used. Both samples were produced directly onto black Kapton, and parylene-N was also deposited directly onto the PVD samples. Therefore, no glue layer was applied between the CH ablator and the sample. The PVD FeO was produced by Dephis company in Etupes, France, and the deposition of a parylene-N layer was performed at the IMPMC laboratory at Sorbonne University in Paris.

Some of the targets were equipped with a sapphire window used for VISAR measurement and pressure determination. The windows were coated with 200-nm aluminium at the Magnetism and Coherent Phenomena Group at DESY. The thin-layer aluminium served as reflecting surface for the VISAR system. The 25- μm sapphire window with aluminium coating was glued to the black Kapton/slurry samples, while the PVD samples were deposited directly to the sapphire windows.

3.4 Experimental setup at LULI

The dynamic compression experiment of (Mg,Fe)O was conducted at the LULI2000 laser facility in March 2023. The purpose of this experiment included in the thesis was to investigate the Hugoniot of the slurry ($\text{Mg}_{0.9}, \text{Fe}_{0.1}$)O and ($\text{Mg}_{0.6}, \text{Fe}_{0.4}$)O, at the pressure of more than 100 GPa. The X-ray diffraction (XRD) was measured to observe the structural changes along the Hugoniot. Additionally, the (Mg,Fe)O PVD and slurry targets were used to compare the differences of the Hugoniot between the pure and the mixture material.

The experimental setup of this experiment is shown in Figure 3.8. Two independent green lasers with the wavelength of 527 nm were used: the temporal laser shape can be adjusted with a pulse length of 0.5 to 15 ns while delivering up to 500 J/beam [67]. One laser, which is referred to as the north laser, was used for generation of X-rays. The pulse length was approximately 1 ns and the spot size was 120 μm : the intensity was in the range of 10^{15} W/cm². This beam illuminated to a backlighter target, which was Fe in this case, to produce a plasma emitting quasi-monochromatic X-ray radiation (He_α) with an energy of 6.7 keV. The produced X-ray was characterized by a von Hamos spectrometer. The other laser, which is named the South laser, was focused on a main target to drive shock compression. The duration of the pulse was 1 to 1.5 ns and the spot size was 1300 μm . The two lasers need approximately one and a half hours for cooling and recharging between each shot, so up to six targets can be shot per day during operation time.

The produced X-ray beam from the backlighter was collimated at the incident angle of 30° into the diffractometer which is arranged like a box around the sample. The outside

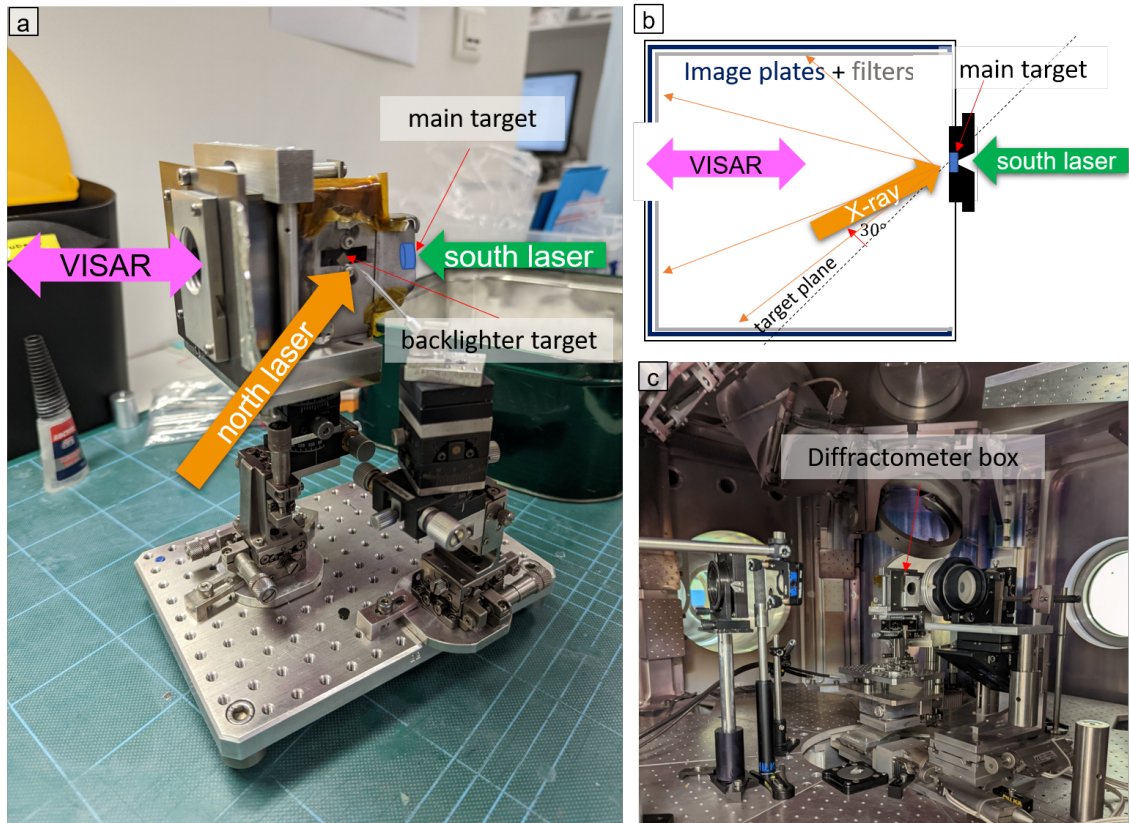


Figure 3.8: The X-ray diffraction set up at the LULI2000 laser facility: (a) the diffractometer box in which the north laser illuminated to a backlighter target and the south laser driven to a main target, (b) schematic of the diffractometer side-view where the X-ray incident angle is 30° to the target plane and (c) the target chamber at the LULI2000 laser facility.

of the diffractometer box is shielded with WC to prevent X-ray leakage [67]. As shown in Figure 3.8(b), the diffractometer works in reflection geometry. The diffracted X-ray from the target during shock compression was collected with five image plates (IPs) and the pixel size was $50 \mu\text{m} \times 50 \mu\text{m}$. In this experiment, the Fuji Biological Analysis System (BAS) MS IPs were used. This type of IPs provide the highest X-ray sensitivity in the photon energy range of 5 to 100 keV compared to the other types [68][69]. The sensitivity of IPs was measured as the number of emitted photon-stimulated luminescence (PSL) per incident photon energy and it was approximately 7 to 8 mPSL/photon at the X-ray energy of 7 to 8 keV for the BAS-MS IPs [68][69]. The IPs were attached to all sides of the box except the target side and the obtained 2θ coverage was 33° to 152° . In addition, to suppress a parasitic X-ray background, black plastic filters were inserted into several parts of the box, such as the collimator and in front of the IPs [67]. In addition to X-ray diffraction, VISAR measurements were also performed: VISAR ω and VISAR 2ω were operated at 1064 and 532 nm with a VISAR sensitivity of 3.44 and 4.955 km/(s · fringe), respectively.

Step targets were used for EoS measurements of slurry of (Mg,Fe)O. The target design is shown in Figure 3.9. The thickness of each layer as well as the total thickness of the target had to be measured to estimate the thickness of the glue layer and perform further calculations. The first layer is 10- μm parylene-N deposited on 50- μm aluminium foil, which was used as a pusher. The third layer is a quartz window with a thickness of 28 μm : it was used as standard material for the VISAR measurement at high pressure. The last layer is the sample in which the backside is coated with 1- μm aluminium. This layer is only mounted on one half of the sample package to get the shock-wave travel-time in the sample, which was then used for calculation of the shock-wave velocity. The particle velocity of the sample was obtained from impedance matching with the quartz window. Thus, the Hugoniot of the sample can be calculated from the measured particle velocity and shock velocity.

3.5 Hydrodynamic simulation

Hydrodynamic simulation is an important tool that allows understanding shock propagation and target response during shock loading. In general, in this work, the simulation was used for refining the experimental design such as target design and estimation of the achievable conditions with the available parameters. Moreover, it can help with interpre-

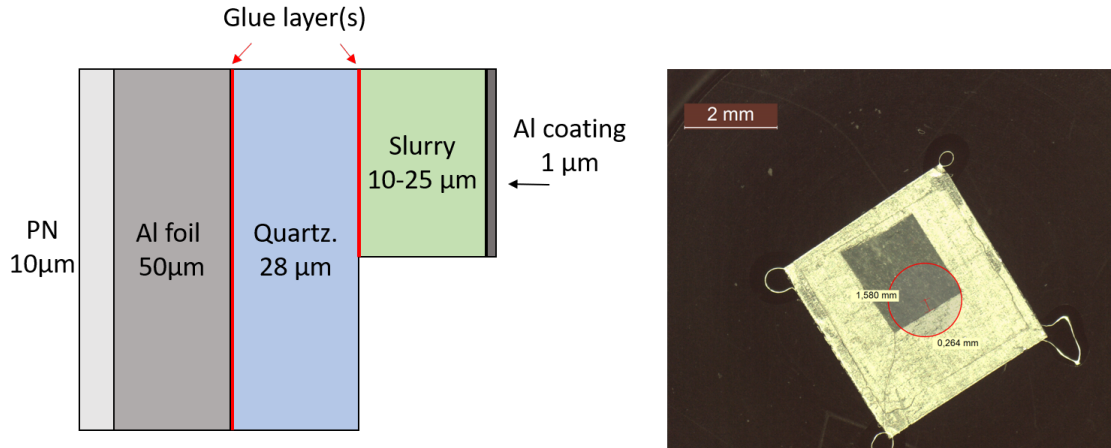


Figure 3.9: Target design for the LULI experiment: configuration of the step target used for EoS measurement (left) and top view of the corresponding target (right).

tation and benchmarking of the experimental data.

In this study, the MULTI simulation software (MULTIgroup radiation transport in MULTIlayer foils) [70] was applied. MULTI is a one-dimensional Lagrangian code that can solve the planar hydrodynamic equation coupled to the radiation transfer equation [70]. It simulates by dividing each layer into a number of meshes defined by a user. Each mesh is identified with an initial position, and its corresponding state is a function of time and initial position. The driven laser profile input to the simulation can be defined as a typical shape such as Gaussian and rectangular, or as a laser profile extracted from the experiment. The properties of each target layer have to be known, such as thickness, equation of state, opacity, and thermal conductivity. These parameters are normally provided by SESAME tables (Los Alamos National Laboratory). The MULTI code limits up to 10 layers of the target with three different materials.

An example of the MULTI simulation is shown in Figure 3.10. The target consists of three layers that are 49- μm parylene-N, 5- μm FeO, and 25- μm sapphire, respectively. The laser profile is 5-ns flat-top with the intensity of $4.285 \times 10^{12} \text{ W/cm}^2$. The result suggests the XRD probing time or the X-ray time delay of 4.2 to 4.6 ns to get a fully compressed structure of FeO with the maximum pressure at 250 GPa (2.5 Mbar). The laser intensity of the simulation ($I_{\text{numerical}}$) has to be calibrated with the laser intensity of the experiment $I_{\text{experiment}}$ to get accurate results. The calibration is typically done by performing several shock-compression shots on one-layer targets of an ablator such as black Kapton and parylene-N. $I_{\text{numerical}}$ is optimized to match the breakout time shot at $I_{\text{experiment}}$ to get the parameter n , where $I_{\text{numerical}} = nI_{\text{experiment}}$ and $0 < n < 1$.

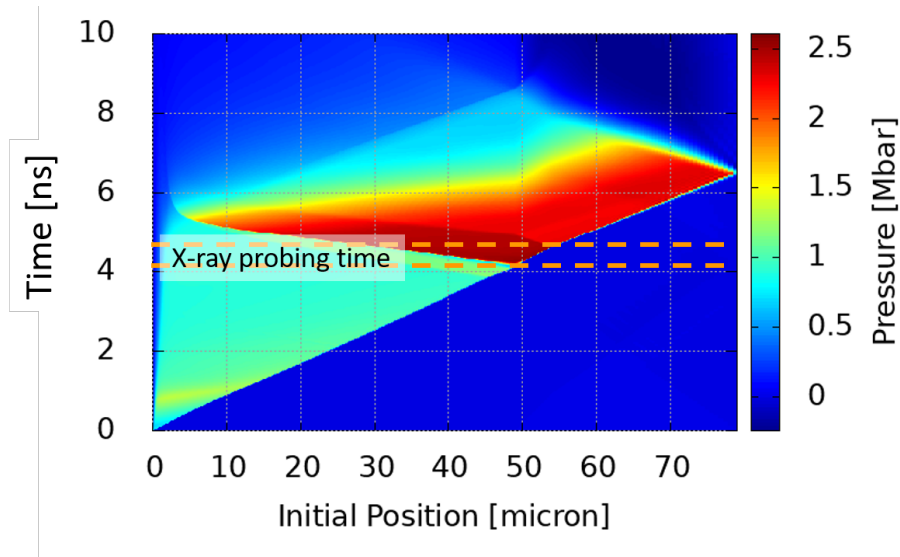


Figure 3.10: Example of the MULTI simulation: a pressure map of the target 49- μm parylene-N, 5- μm FeO, and 25- μm sapphire at the corresponding time and initial position.

Chapter 4

FeO

In this chapter, the results from the shock compression experiment of FeO is presented. The main goal of this experiment is to probe structural phase transition of FeO under shock loading towards a pressure of more than 200 GPa . This includes an investigation of FeO solid-liquid boundary along its Hugoniot. Section 4.1 presents the results from XRD measurement showing FeO structures during shock compression. Calculation of the pressure from VISAR analysis and hydrodynamic simulation is described in section 4.2. This chapter also includes the discussion on the results and compared to the previous studies in section 4.3.

4.1 FeO structures under shock compression

The shock compression experiment was performed at the MEC end-station of LCLS in February 2022. The experimental setup is described in Section 3.3. Two types of PVD FeO targets were used: 50- μm black Kapton (BK)/ 5- μm FeO and 49- μm Parylene-N (PN)/ 5- μm FeO/ 25- μm sapphire, as shown in Figure 4.1. The 200-nm Al between FeO and sapphire was used as a reflective surface for the VISAR. The slurry targets were prepared with the configuration 50- μm BK/FeO. The thickness of slurry FeO varied between 26 and 31 μm .

The XRD of FeO at ambient and under shock compression was recorded by four ePix detectors named as Quad 0 to 3. Figure 4.2 shows the azimuthally integrated XRD of the PVD FeO in the BK/FeO targets collected from Quad 0, which covers the Q range of 1.8 to 3.4 \AA^{-1} or the 2θ of 16 to 34 degrees at the X-ray energy of 13 keV. At ambient conditions, the XRD shows (111) and (200) peaks of B1 FeO at Q values of 2.6 and 3.0 \AA^{-1} . These are equivalent to the lattice parameter a of 4.2 \AA , which is smaller compared

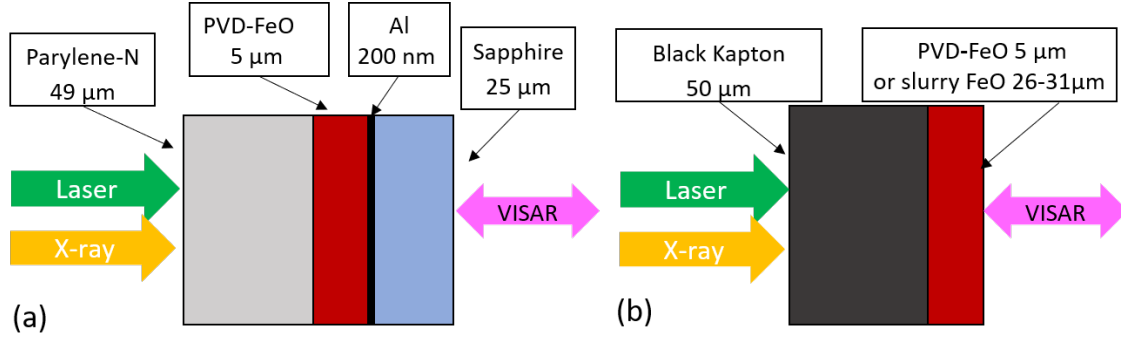


Figure 4.1: FeO sample configuration used in this study: (a) 49- μm Parylene-N (PN)/ 5- μm PVD-FeO/ 200-nm Al/ 25- μm sapphire, and (b) 50- μm black Kapton (BK)/ 5- μm PVD-FeO or 26-31 μm slurry-FeO. The 200-nm Al between FeO and sapphire in (a) serves as reflective surface for VISAR.

to powder FeO from previous research [18][19][71]. The compression could arise from the residual stress during the deposition [72]: it is discussed in section 5.3. Furthermore, XRD at ambient conditions shows additional peaks identified as Fe_2O_3 , which could occur due to the oxidation of FeO.

The PVD FeO was shot with different laser intensities aiming at different pressures along the Hugoniot. The shock breakout time of each shot was calculated from the corresponding VISAR, which is described in Section 4.2: the time was compared to the X-ray delay to indicate when the XRD was taken compared to the shock breakout. This relative time is labeled for each XRD as shown in Figure 4.2. From the results, only the solid B1 and the liquid FeO were observed throughout all experimental conditions. At laser intensities of 5.6×10^{12} and 6.5×10^{12} W/cm^2 , FeO was stable in B1 solid phase. The pressure was released as FeO became decompressed within 0.5 ns after shock breakout. At the time of 2.8 ns after the shock breakout, the lattice parameter of FeO was approximately 4.33 Å. This value is bigger than lattice parameters of the ambient PVD FeO, which indicates ambient pressure and high temperature conditions. At higher laser intensities, B1 FeO became molten at the time close to the shock breakout time. At 0.9 ns after shock breakout, liquid FeO crystallized to B1-structure at the conditions of the laser intensity 8.5×10^{12} W/cm^2 . In contrast to the shots at the laser intensity of 1.2×10^{13} W/cm^2 , FeO was still liquid at 1.0 ns after the shock breakout.

XRD patterns measured at the time of shock breakout represent the conditions on its Hugoniot. Figure 4.3 shows the integrated XRD lineout of FeO measured close to shock breakout with 17-keV X-rays. These were recorded by Quad 0, which cover the Q range of 2.3 to 4.8 \AA^{-1} . The ambient peaks of FeO B1 structure are labeled as (111), (200), and (220) peaks that correspond to the Q value of 2.6, 3.0 and 4.2 \AA^{-1} . The ambient peaks

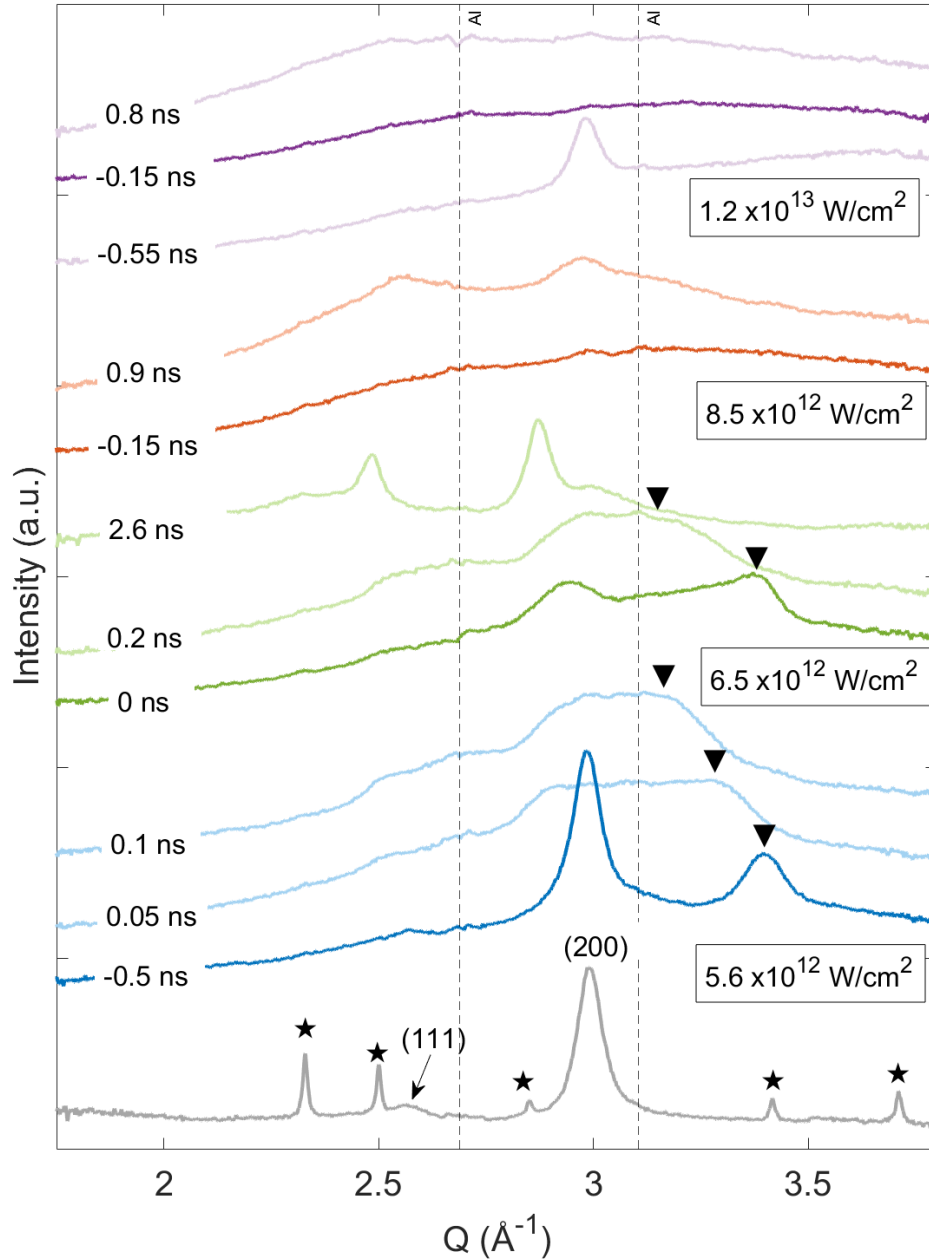


Figure 4.2: Integrated XRD lineout of BK/PVD-FeO targets under shock-compression at various laser intensities. Diffraction was obtained by 13-keV X-rays and collected in the Quad 0 detector. The time is given as a relative time to the shock breakout. FeO ambient peaks include the reflection from (111), (200), and (220) planes. The compressed FeO peaks from (200) are labeled as reverted triangles and ambient Fe_2O_3 peaks are marked as a star. The dash lines show the position of Al, which are from a sample frame.

were observed together with the high-pressure (200) peaks of FeO when the XRD was probed before the shock breakout. The results show that FeO stayed in the B1-structure phase up to a laser intensity of $7.5 \times 10^{12} \text{ W/cm}^2$ and was molten during shot at a laser intensity of $8.8 \times 10^{12} \text{ W/cm}^2$.

The XRD of the PN/FeO/sapphire targets was also collected during shock compression. Unfortunately, only a few shots were measured before or at the shock breakout time. At the laser intensity of $7.1 \times 10^{12} \text{ W/cm}^2$, FeO in the PN/FeO/sapphire was already molten 0.1 ns before shock breakout, as shown in Figure 4.4. In contrast, FeO in the BK/FeO target was still solid at the same intensity, as shown in Figure 4.3. This shows the different conditions created by the two ablator materials that were used, i.e. black Kapton and Parylene-N.

Slurry FeO was measured by XRD at ambient and under shock loading at laser intensities of 6.1×10^{12} , 8.7×10^{12} , and $1.2 \times 10^{13} \text{ W/cm}^2$, as shown in Figure 4.5. At ambient conditions, the XRD pattern includes the (111), (200) FeO and also Fe_3O_4 peaks. In contrast to the PVD targets, the compressed (111) peaks of FeO is also observable together with the (200) peak. The results shows that slurry FeO remains stable as B1 structure at shots with the laser intensities of 6.1×10^{12} and $8.7 \times 10^{12} \text{ W/cm}^2$. Liquid FeO was observed at the maximum laser intensity $1.2 \times 10^{13} \text{ W/cm}^2$.

Lattice parameters as well as volume of PVD-FeO under shock compression were obtained by performing the peak fitting with Pseudo-Voigt function in the Origin software package (Origin(Pro), Version 2022. OriginLab Corporation, Northampton, MA, USA). The (200) FeO peak was chosen for the peak-fitting because it is a major peak being observable in the shots taken with 17-keV X-rays, where the XRD intensity is very low. A *Le bail* refinement using the GSAS-II software package [73] was also performed for the slurry targets since not only (200) but also (111) peaks at high pressure were observed in the Quad 0 detector. A peak fitting was done in addition and compared to the results of the refinement. The results show less than 1% difference between a (200) peak fitting and a refinement. The summary of the results from refinement as well as from peak fitting are shown in Tables A.1 and A.2 in the Appendix A.

The unit cell volumes of PVD and slurry FeO shot at corresponding laser intensities were compared as shown in Figure 4.6. At the same intensities, the unit cell volumes of FeO in BK/slurry targets are bigger than the ones from BK/PVD-FeO targets. In addition, slurry FeO required higher laser intensity for melting. This suggests the possible difference of Hugoniot between pure FeO and FeO-epoxy mixture. The details are discussed in

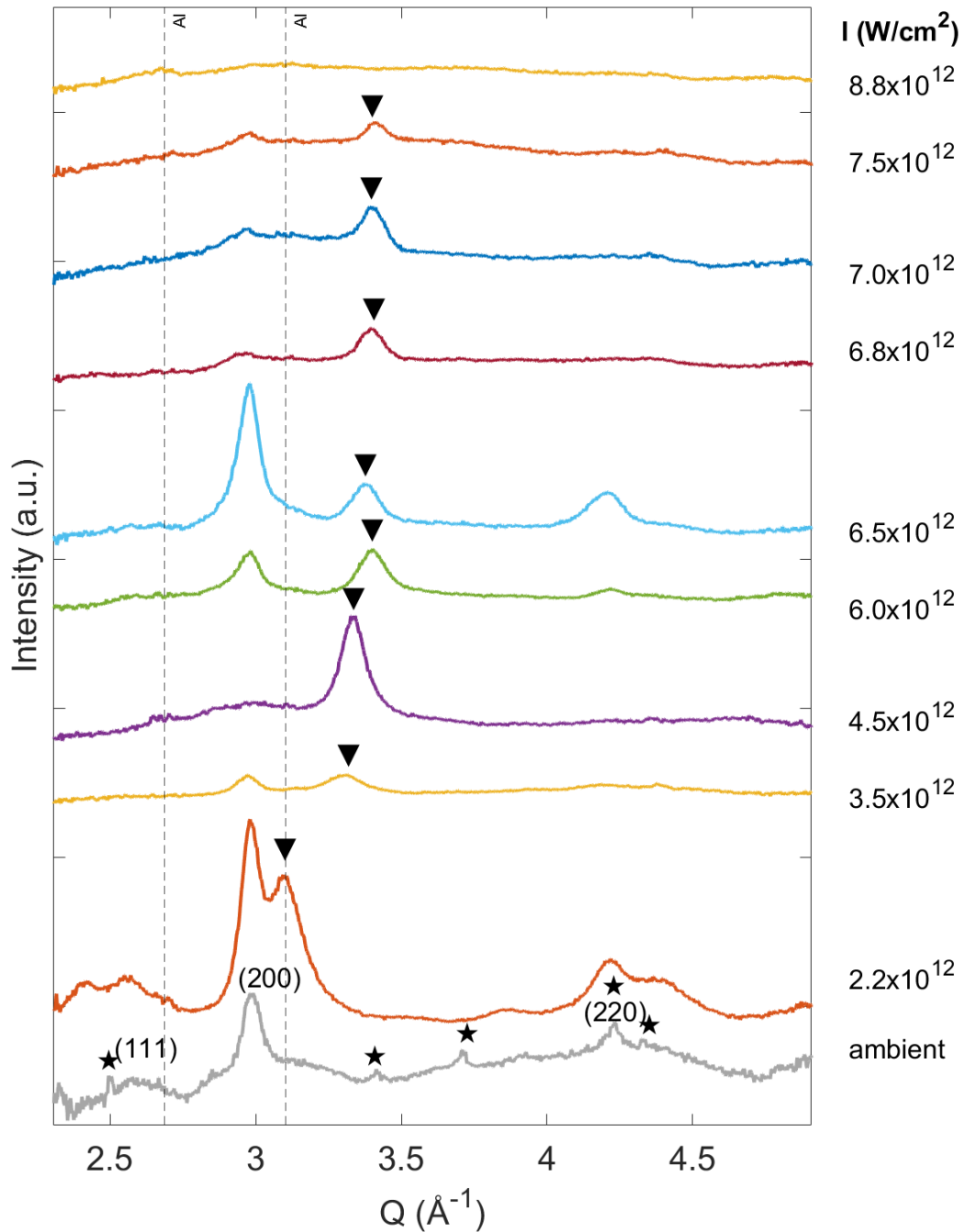


Figure 4.3: Integrated XRD lineout of the BK/PVD-FeO targets under shock-compression at various laser intensities collected by the Quad 0 detector. They were measured by 17-keV X-rays close to shock breakout time. The FeO ambient peaks include the reflection from (111), (200), and (220) planes. The compressed (200) FeO and ambient Fe_2O_3 peaks are labeled as reverted triangles and stars, respectively. The dash lines show the position of Al, which are from the sample frame.

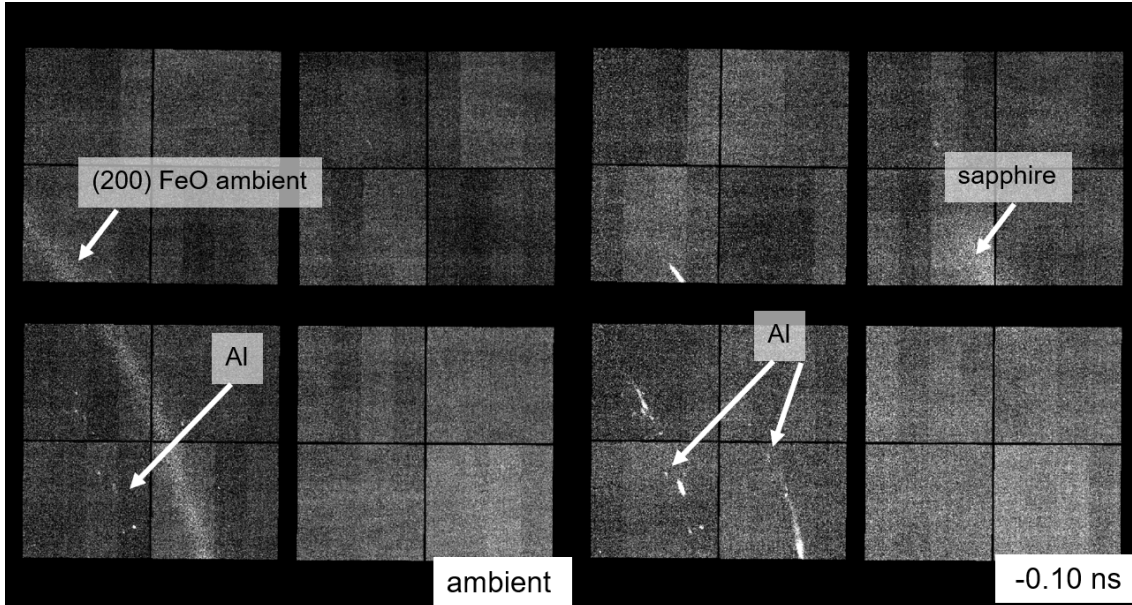


Figure 4.4: 2D XRD raw images of the PN/FeO/sapphire target taken at ambient conditions and 0.1 ns before shock breakout. No FeO peak is observed during shock indicating the melting of FeO at a laser intensity of $7.1 \times 10^{12} \text{ W/cm}^2$.

Section 4.3.

4.2 Pressure determination of FeO under shock compression

VISAR analysis

In this study, the pressure of FeO under shock compression in PN/FeO/sapphire targets was determined by VISAR analysis. At high pressure conditions, it requires a pressure window to get an information on the pressure from VISAR, while the free surface velocity is possibly observed at low pressures. Sapphire (Al_2O_3 single crystal) was chosen as a pressure window because it has similar shock impedance like FeO [26][74]. The Hugoniot elastic limit (HEL) of sapphire is at approximately 20 GPa [74] and it becomes opaque at shock pressures above 100 GPa [75].

The first step of VISAR analysis was to indicate the shock breakout time from FeO for the PN/FeO/sapphire and the BK/FeO targets at each laser intensity. Examples of the VISAR images from the PN/FeO/sapphire are shown in Figure 3.6. The horizontal axis corresponds to the position, where the field of view of the streak camera is $265 \mu\text{m}$. The vertical axis shows the time and t_0 is the time when a drive laser arrives at the target surface

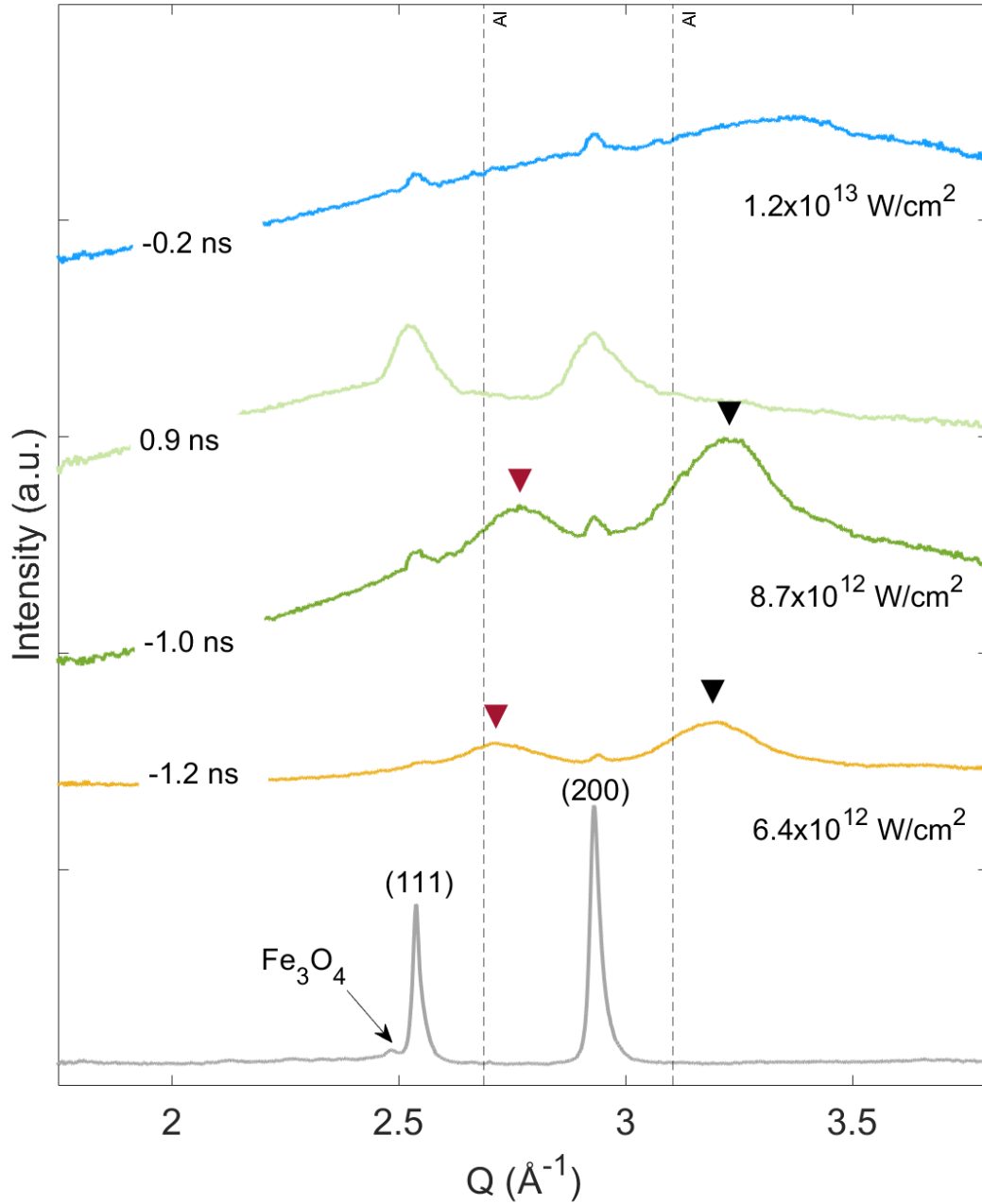


Figure 4.5: Integrated XRD of the BK/slurry-FeO targets under shock-compression at various laser intensities measured by 13-keV X-rays and collected by the Quad 0 detector. The FeO ambient peaks include the reflection from (111) and (200) planes. The compressed (111) and (200) FeO are labeled as red and black reverted triangles, respectively. The ambient Fe₃O₄ peaks is observed at ambient. The dash lines show the position of Al, which are from a sample frame.

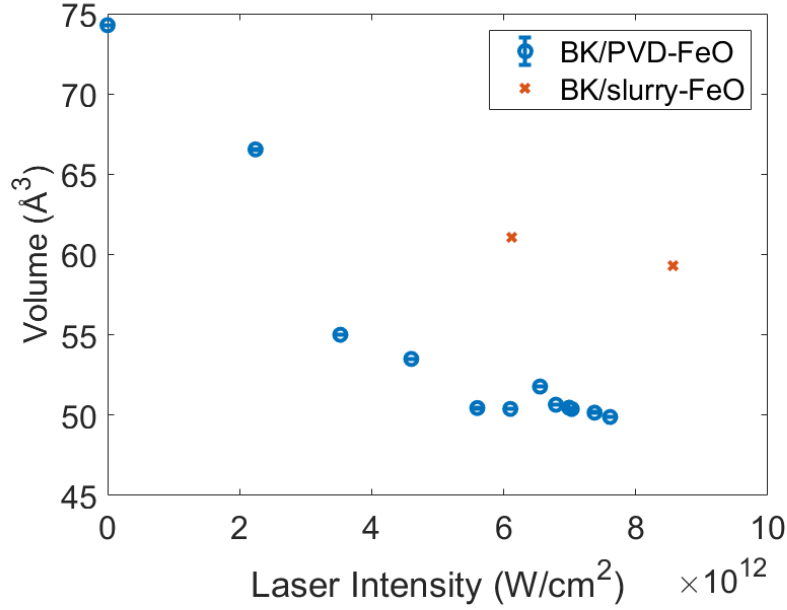


Figure 4.6: Volume of PVD and slurry FeO observed at the shots with different laser intensities.

i.e. black Kapton or Parylene-N in this case. The relation of shock breakout time from FeO and the laser intensity is plotted in Figure 4.7. The results show that Parylene-N as an ablator gives an earlier shock breakout by approximately 1 ns at the same laser intensity compared to black Kapton. The thickness of black Kapton and Parylene-N is almost the same, so the Parylene-N gave the greater shock velocity i.e. the higher shock pressure in FeO at the same laser intensity.

To calculate the pressure of FeO in the PN/FeO/sapphire target, the particle velocity (U_p) or shock velocity (U_s) of the sapphire has to be known from the VISAR. In this study, Neutrino software (Copyright (C) 2013 Alessandro Flacco, Tommaso Vinci All Rights Reserved) was used for VISAR analysis. An example of a typical VISAR image and the corresponding velocity profile from this experiment is already shown in Figure 3.6 (Section 3.2). The U_p was obtained by matching the U_p profile extracted from VISAR 1 and 2. The U_s was determined from a travel time of the shock wave in the sapphire obtained from VISAR. The pressure of FeO was then calculated by the impedance matching technique, where the Hugoniot of both FeO [76] and sapphire [74] were used.

An example of the impedance matching performed for the sapphire U_s of 12.5 km/s is depicted as Figure 4.8. The U_s in sapphire was converted to a U_p of 3.91 km/s by the following equation:

$$U_s = a_0 + a_1 U_p, \quad (4.1)$$

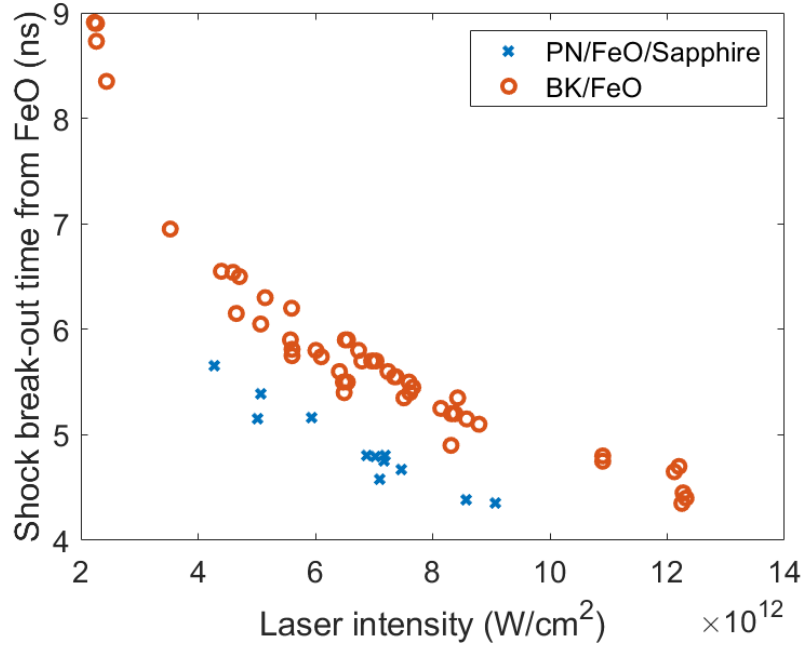


Figure 4.7: Shock breakout-time from FeO of PN/FeO/Sapphire and BK/FeO targets shot with different laser intensities.

where $a_0 = 8.729$, and $a_1 = 0.965$ [74]. The corresponding pressure of sapphire can be calculated from equation 3.2, where the density of sapphire is 4.2 g/cm^3 . Another way of obtaining shock conditions is to calculate by fitting the Hugoniot data $P(U_p)$ from the reference [74]. The Hugoniot of sapphire from the fitting is expressed as follows:

$$P_{sap}(U_{p,sap}) = -0.9112 + 36.7276U_{p,sap} + 3.6078U_{p,sap}^2 \quad (4.2)$$

The corresponding pressure of sapphire is 198.25 GPa, when U_p is 3.91 km/s. These U_p and pressure values also represent the state of FeO at the boundary when the shock was transmitting from FeO to sapphire. To find the state of FeO just before the shock transmitting i.e. at the shock breakout, the mirror Hugoniot of FeO was drawn to cross the Hugoniot of sapphire at this point. To calculate the mirror Hugoniot, the Hugoniot $P(U_p)$ of FeO is firstly expressed as followed:

$$P(U_p) = b_0 + b_1U_p + b_2U_p^2. \quad (4.3)$$

The Hugoniot data of FeO [76] was fitted with the above equation: b_0 , b_1 , and b_2 are 14.4601, 12.7889, and 9.7940, respectively. The mirror Hugoniot crossing at the $(U_{p,sap}, P_{sap})$

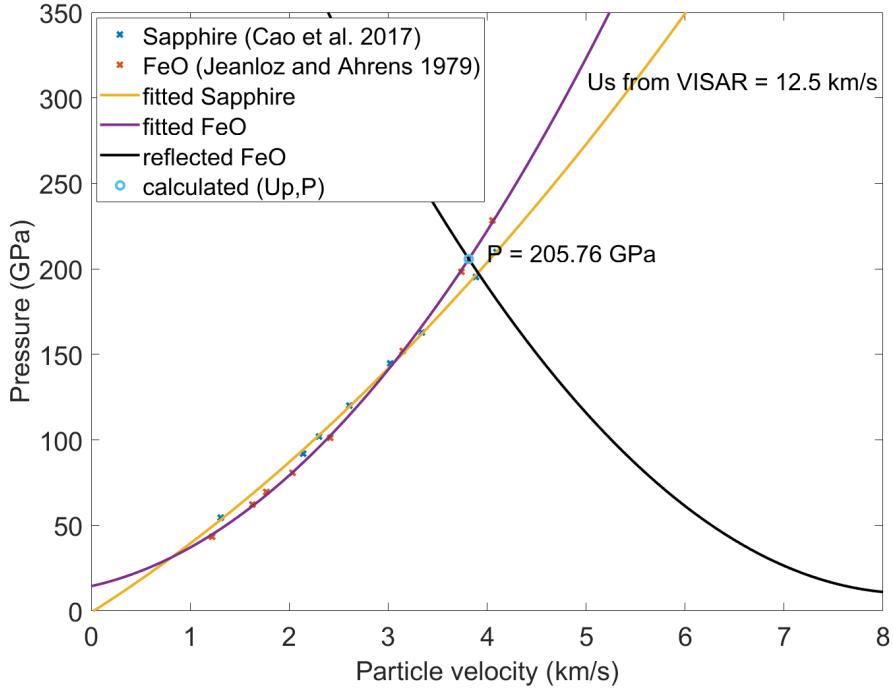


Figure 4.8: Example of impedance matching performed for the shot when the sapphire U_s is equal to 12.5 km/s.

can be calculated from the translation of $P(U_p)$ of FeO to the left by the distance d , where

$$d = U_{p,sap} - \frac{-b_1 - \sqrt{b_1^2 - 4b_2(b_0 - P_{sap})}}{2b_2}. \quad (4.4)$$

Therefore, the mirror Hugoniot of FeO $P_m(U_p)$ can be written as the following equation:

$$P_m(U_p) = b_0 - db_1 + d^2b_2 + (b_1 - 2db_2)U_p + b_2U_p^2. \quad (4.5)$$

U_p and P of FeO at the breakout time are calculated from the intersection point of the Hugoniot and the mirror Hugoniot of FeO. $U_{p,FeO}$ at the shock breakout is then calculated from

$$U_{p,FeO} = \frac{-db_1 + d^2b_2}{2db_2}. \quad (4.6)$$

P_{FeO} is then calculated by substituting $U_{p,FeO}$ in equation 4.3. In this example, $U_{p,FeO}$ and P_{FeO} are 3.81 km/s and 205.76 GPa, respectively. In this case, a shock wave with a lower pressure is transmitting from FeO to sapphire.

The relation between laser intensity and pressure of FeO in the PN/PVD-FeO/sapphire target calculated from the impedance matching technique is illustrated in Figure 4.9. The error-bar is related to the thickness uncertainty of the sapphire windows. The results show

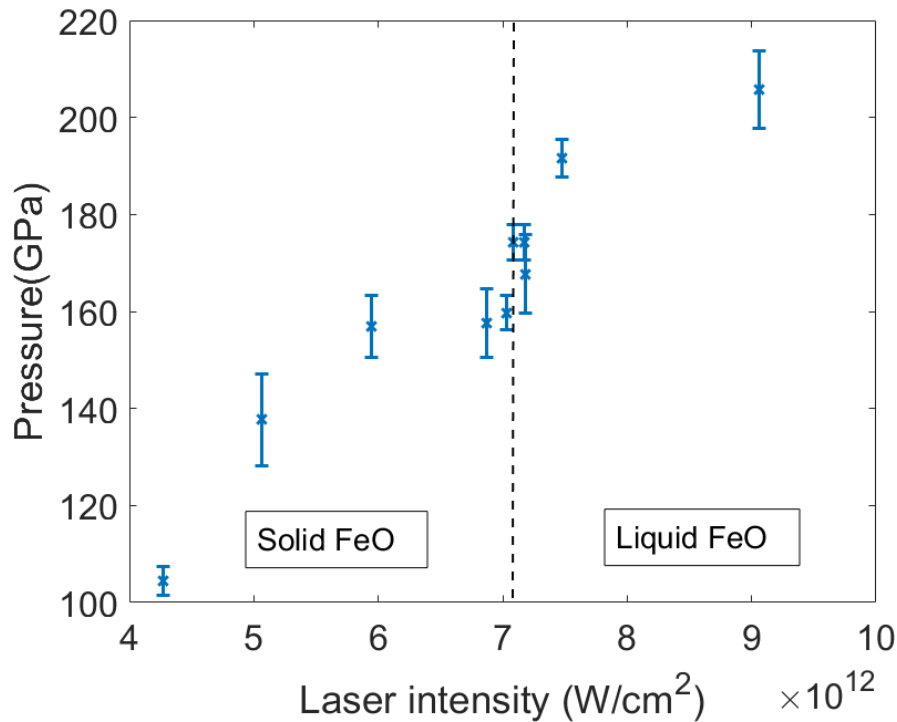


Figure 4.9: Pressure of FeO of PN/PVD-FeO/Sapphire targets shot with corresponding laser intensities. The pressure was calculated from the impedance matching technique by using U_s in a sapphire as an input. The solid-liquid boundary of FeO is taken from the results as shown in Figure 4.4.

that a maximum pressure of approximately 210 GPa was reached with a laser intensity of $9.1 \times 10^{12} \text{ W/cm}^2$. Regarding to the XRD results as shown in Figure 4.4, liquid FeO is observed at the laser intensity of $7.1 \times 10^{12} \text{ W/cm}^2$. The pressure corresponding to this laser intensity is in the range of 160 to 180 GPa and infers the FeO solid-liquid boundary along its Hugoniot.

Hydrodynamic simulation

The pressure of FeO in the BK/PVD-FeO targets cannot be directly obtained from VISAR due to unavailability of the free surface velocity. Thus, the pressure was instead obtained from hydrodynamic simulation in this study. The MULTI code was used for both targets with the EoS of black Kapton, Parylene-N, and sapphire taken from Kapton EoS, which is a modified SESAME 7710 of parylene, SESAME tables 7591, and 7411, respectively. The FeO EoS was obtained from the quotidian equation of state (QEOS). All the simulations were performed by inputting the laser pulse shapes from the experiment and the actual thickness of each layer as shown in Appendix B. To simulate the conditions being comparable to the experiment, a numerical intensity ($I_{\text{numerical}}$) was first optimized to

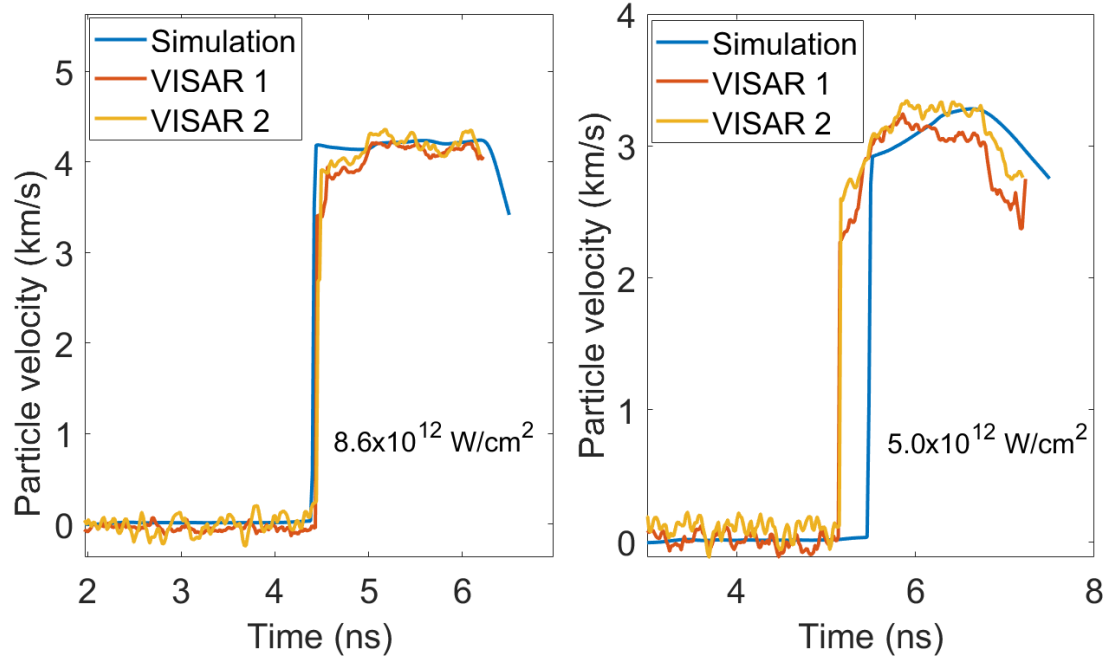


Figure 4.10: Examples of U_p -time plots at the FeO/Sapphire interface of the shots with laser intensities of 8.6×10^{12} and 5.0×10^{12} W/cm². They are compared between the results from hydrodynamic simulation and VISARs.

match the corresponding intensity from the experiment ($I_{\text{experiment}}$). The laser intensity given from the experiment cannot be perfectly 100% transferred to the sample. For instance, some parts of the laser were cut at or outside of a phase plate. The U_p profile of the FeO-sapphire interface was used as a constraint as shown in Figure 4.10. The results by using the laser intensities of 8.6×10^{12} and 5.0×10^{12} W/cm² show that U_p the simulation matches the VISAR data when $I_{\text{numerical}} = 0.45I_{\text{experiment}}$.

The shock breakout time from the simulation was compared to the result from VISAR. For PN/FeO/sapphire target, the shock breakout times from the simulation are consistent with the result from VISAR, as shown in Figure 4.11: the differences are less than 0.15 ns, and only one outlier is observed with 0.3 ns difference. In contrast, a larger difference is observed for the results from the BK/FeO targets: breakout times from the simulation are up to 0.4 ns later than the ones calculated from VISAR for the laser intensity range between 3×10^{12} and 1.2×10^{13} w/cm², as shown in Figure 4.12. At the laser intensity of 2×10^{12} , a discrepancy of 1 ns was observed when using $I_{\text{numerical}} = 0.45I_{\text{experiment}}$: this indicates the different $I_{\text{numerical}}$ used for the simulation at the low laser intensity. Thus, $I_{\text{numerical}}$ was optimized to match the BO time and $I_{\text{numerical}} = 0.275I_{\text{experiment}}$ was instead used for simulation at 2×10^{12} .

The pressure of FeO in PN/FeO/sapphire and BK/FeO targets was obtained from the

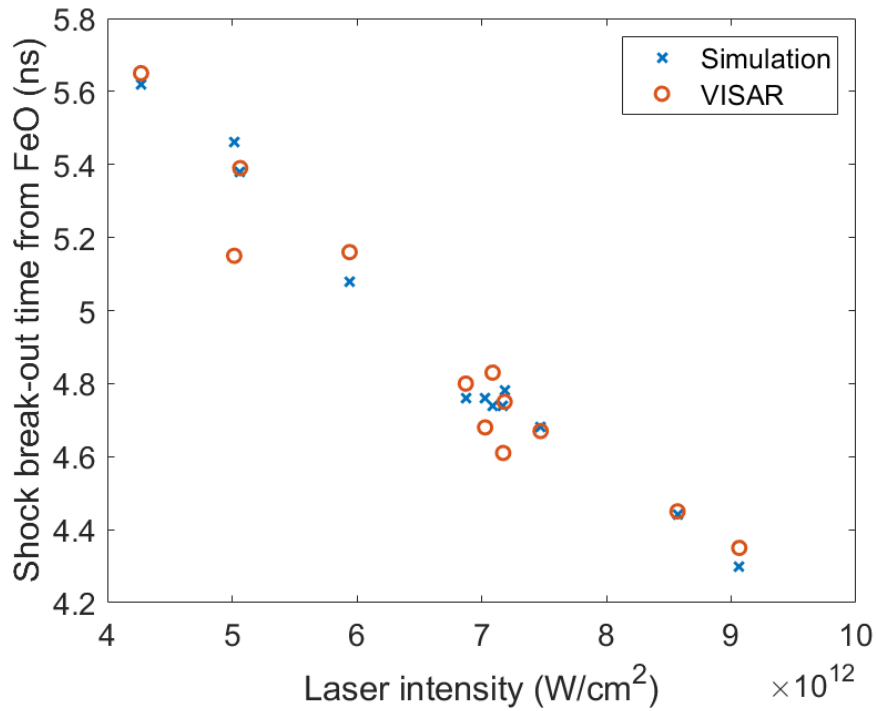


Figure 4.11: Shock breakout-time from FeO of PN/FeO/sapphire targets shot at different input laser intensities. The results are taken from hydrodynamic simulation and VISAR data.

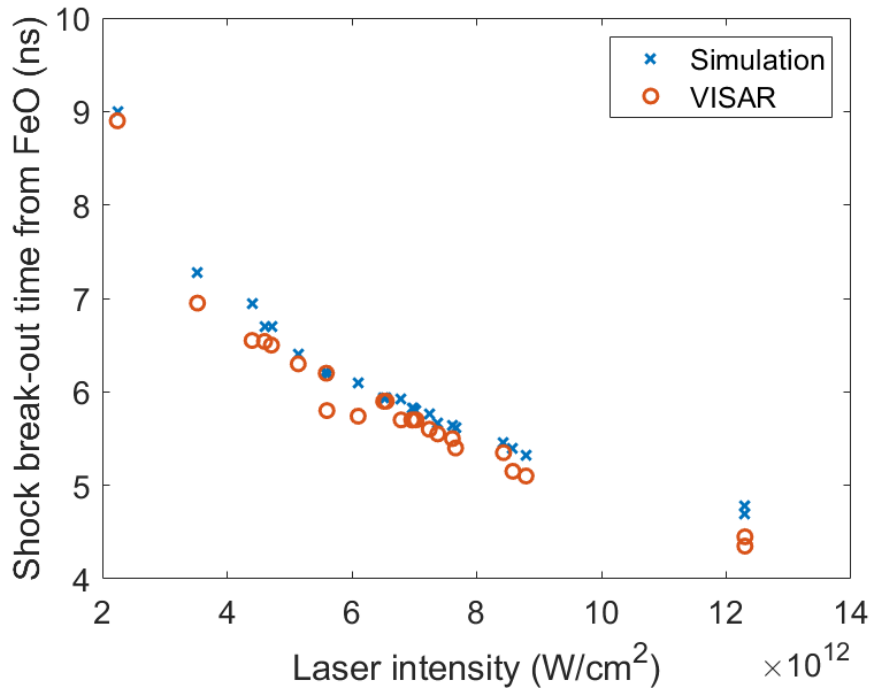


Figure 4.12: Shock breakout-time from FeO of BK/FeO targets shot at different input laser intensities. The results are taken from hydrodynamic simulation and VISAR data

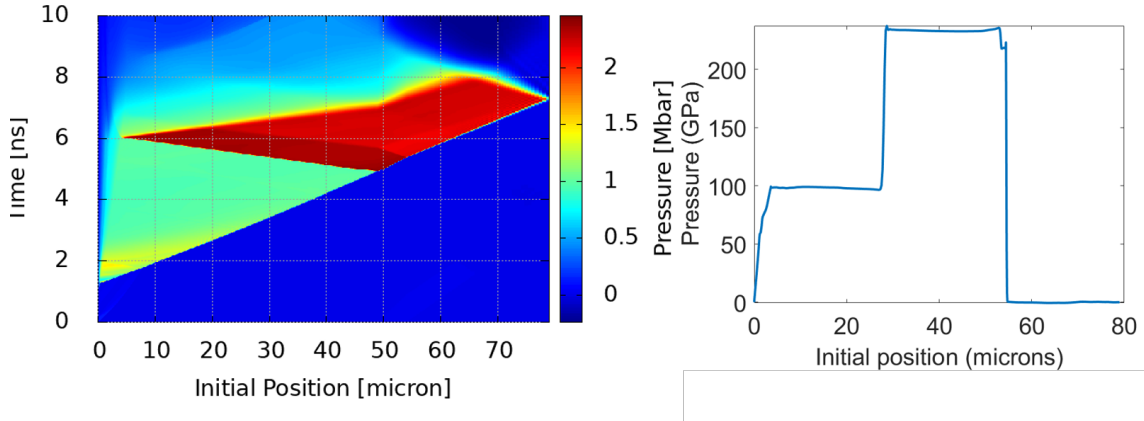


Figure 4.13: Examples of a pressure map and a corresponding pressure profile at the shock breakout time (5.44 ns) of the PN/FeO/sapphire performed by hydrodynamic simulation with the laser intensity of $0.45 \times 8.57 \times 10^{12} \text{ W/cm}^2$.

hydrodynamic simulation. Figure 4.13 shows an example pressure map of the PN/FeO/sapphire target when inputting the laser intensity of $0.45 \times 8.57 \times 10^{12} \text{ W/cm}^2$. The starting time when a laser arrive at the Parylene-N was delayed by 1 ns to include a rising part of the laser shape. The shock breakout time from FeO is 4.44 ns (or 5.44 ns in the map). The pressure lineout at the breakout is also depicted in Figure 4.13. The peak pressure at the initial position of 49 to 54 μm , which corresponds to FeO, is 223.5 GPa.

The pressure of FeO in PN/FeO/sapphire targets from the simulation is shown in Figure 4.14 and is compared to the pressure calculated from the impedance matching technique using U_p and U_s . The results show that the pressure from the simulation matches better with the pressure calculated from U_p compared to the ones calculated from U_s . This is because the optimization is constrained by U_p profile. The pressure calculated from U_s showing the lower values could arise from the difference EoS using for the impedance matching and the simulation.

Figure 4.15 shows the calculated pressure of FeO in the BK/FeO targets from the simulation. The maximum pressure of FeO in BK/FeO target is approximately 230 GPa when the laser intensity is at $1.2 \times 10^{13} \text{ W/cm}^2$. The solid-liquid boundary of FeO was identified based on the XRD results as shown in Figure 4.3, where FeO was molten at the laser intensity of $8.8 \times 10^{12} \text{ W/cm}^2$. The pressure at the boundary is 172 to 189 GPa that overlaps with the result from PN/FeO/sapphire targets of Figure 4.9, where the solid-liquid boundary was shown to be at 160 to 180 GPa.

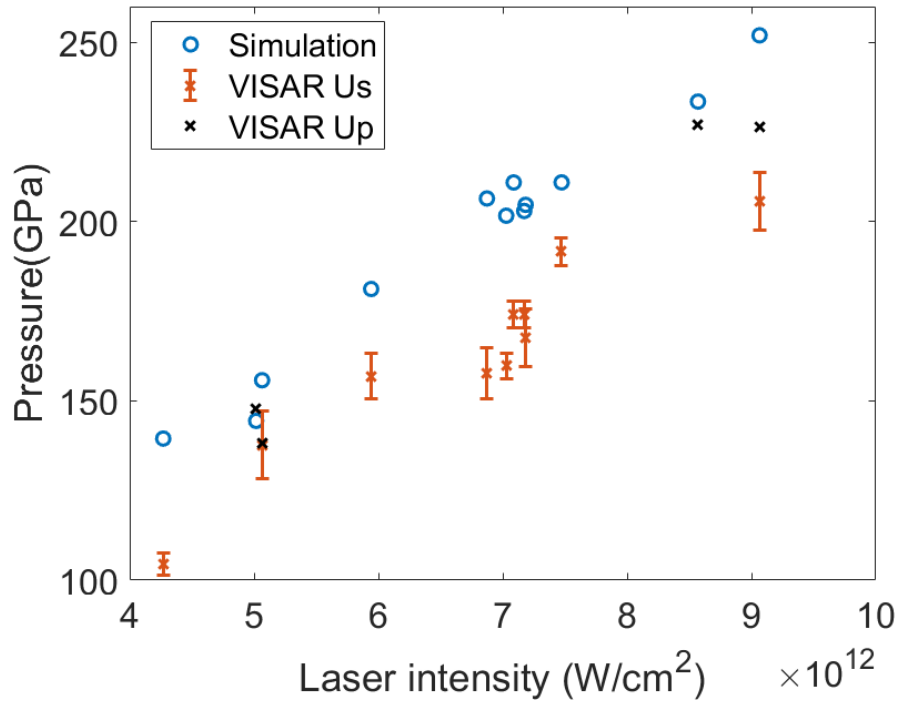


Figure 4.14: Relation between pressure of FeO of PN/PVD-FeO/Sapphire targets and laser intensities calculated by hydrodynamic simulation.

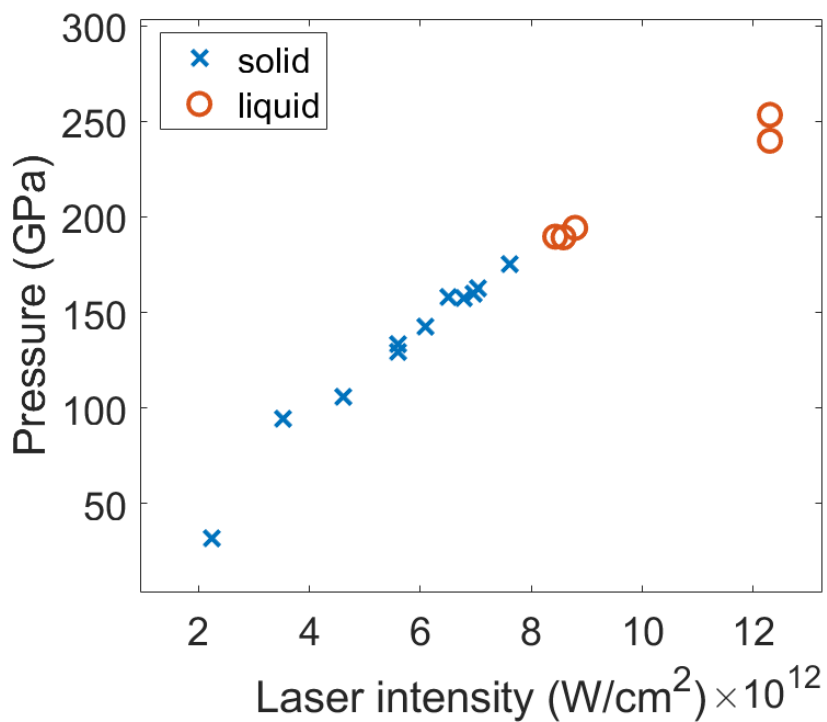


Figure 4.15: Relation between pressure of FeO of BK/PVD-FeO targets and laser intensities calculated by hydrodynamic simulation. The solid-liquid boundary of FeO is taken from the XRD results as shown in Figure 4.3.

4.3 Discussion

In this chapter, the results from shock compression experiment of FeO are presented. PVD FeO with a unit cell parameter of 4.20 Å was used as a starting material. In general, FeO has non-stoichiometry compositions and is written as Fe_{1-x}O , where $0.04 < x < 0.12$ at ambient pressure [77][78]. The chemical composition can be calculated from the following equation [78][79]:

$$a = 3.856 + 0.478(1 - x) \quad (4.7)$$

Here $x = 0.28$ was obtained for the PVD FeO with $a = 4.20$ Å, but it is not in the range of x at ambient. Therefore, this small unit cell parameter cannot only be caused by the FeO defect. In addition, it was the result of residual stress occurring during deposition [72]. Consequently, the chemical composition as well as the density of this PVD FeO cannot be directly calculated from the equation 4.7.

The volume of shock-compressed FeO was obtained from XRD measurement, while the pressure of FeO under shock compression was calculated from hydrodynamic simulation as described in Sections 4.1 and 4.2, respectively. The relationship between volume obtained from the XRD measurement and the pressure of shock-compressed FeO from hydrodynamic simulation is plotted as Figure 4.16. They are compared with those of the DAC experiments [19][71]. The results show that the volumes of shock-compressed FeO from this study are smaller compared to the DAC experiments including the one at 300K. However, PVD FeO samples have a smaller lattice parameter compared to the other experiments, where a of FeO was approximately 4.3 Å. To better understand and interpret it, the compressed volume (V/V_0) of FeO is plotted as a function of pressure as shown in Figure 4.17. The results of V/V_0 and pressure show agreement with those of both DAC experiments at high temperature and the shock compression experiment.

The smaller volume of FeO at approximately 120 to 130 GPa was observed. Since no structural phase transition was detected, it could occur from electronic transitions such as metalization and spin transition. A decrease in resistivity indicating metalization of $\text{Fe}_{0.94}\text{O}$ under shock loading was observed at above 72 GPa and 1200K [26]. The spin transition of B8 FeO was founded in the DAC experiment with 2.5% reduction of volume at ambient and small reduction at high temperature [80]. The recent ab-initio calculation suggested that the high-spin to low-spin transition of B1 FeO occurs at a pressure-temperature ranging from 100 to 200 GPa and 0 to 4000K [81]. However, observation of

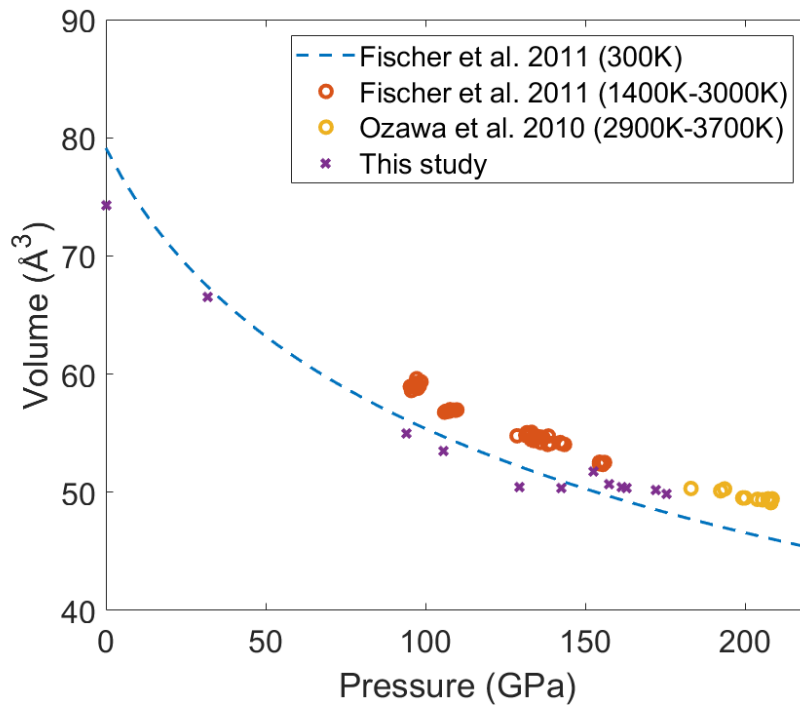


Figure 4.16: Relation between pressure and volume of FeO under shock compression compared to the results from DAC experiments [19][71].

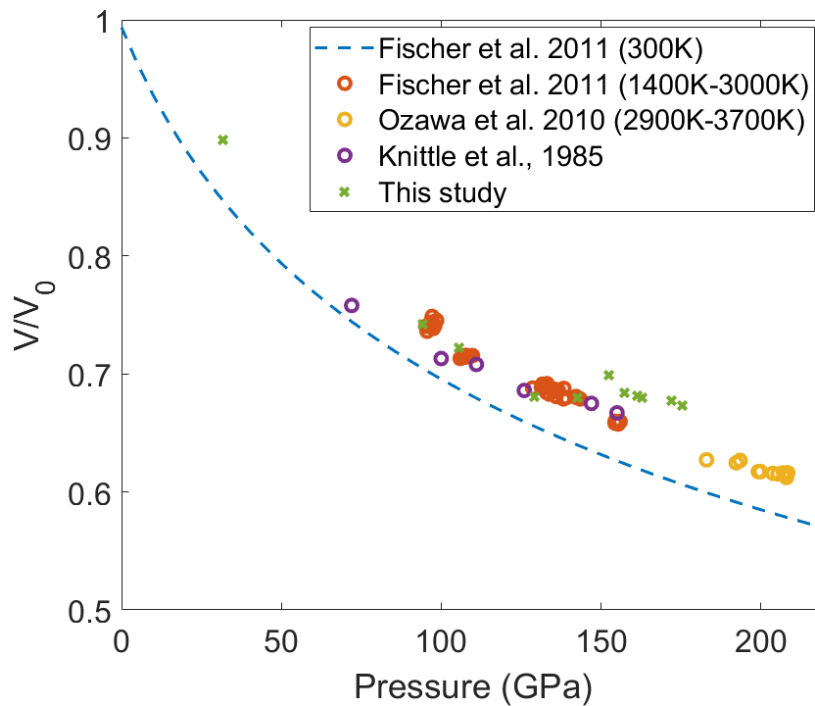


Figure 4.17: Relation between pressure and compressed volume (V/V_0) of FeO under shock compression compared to the results from DAC experiments [19][71] and shock-compression experiment [26].

denser FeO could also be possibly caused by technical problem. For instance, the effective laser power could be higher at this point. Thus, further shock compression experiments of FeO at this pressure with additional X-ray spectroscopy measurements will be helpful for the interpretation.

In this study, the maximum FeO pressure was reached at 250 GPa. The XRD shows that solid B1 FeO was stable up to a pressure of 172 GPa and liquid FeO was observed at a pressure of above 189 GPa. The solid-liquid boundary of FeO along the Hugoniot was thus defined at 172 to 189 GPa. The literature [22] shows the intersection of FeO Hugoniot and melting line at approximately 200 GPa, which was inferred from extrapolation of the shock compression data [26] and the melting curve [82] of $\text{Fe}_{0.94}\text{O}$. The result from this study shows FeO solid-liquid boundary at a lower pressure by approximately 10 GPa.

Apart from the PVD targets, the shock compression on the FeO slurry targets was performed. The results show larger unit cell volume at the same laser intensities. In addition, the slurry target required a higher laser intensity to reach the solid-liquid boundary of FeO compared to the PVD target. The possible explanation is that the Hugoniot of the slurry and the PVD FeO are different. This scenario could be described by impedance matching of black Kapton and polycrystalline FeO or slurry FeO, as shown in Figure 4.18. The Hugoniot of black Kapton and FeO are taken from the literatures [83] [76], respectively. Hugoniot of slurry FeO is calculated based on the velocity-based mixing rules from the literature [54] from Hugoniot of FeO [76] and epoxy [84]. The scenario is started by driving the laser intensity, which is $4.0 \times 10^{12} \text{ W/cm}^2$ in this case, and the pressure in a black Kapton before a shock wave enters to a next layer of the target is approximately 42 GPa. The pressure of the next layer depends on a materials: the pressure is expected to be higher in polycrystalline FeO compared to slurry FeO when using the same laser intensity. More description on the Hugoniot of the slurry and validation of the calculated Hugoniot of the slurry are discussed in Section 5.3.

Uncertainty of VISAR measurement and hydrodynamic simulation

This study demonstrates the calculation of the pressure of FeO under shock compression from hydrodynamic simulation. The results were constrained by two parameters from VISAR, i.e. U_p and shock breakout time. Therefore, the uncertainty of the calculated pressure relies on the precision of the VISAR measurement and the correctness of the parameters and EoS used for the simulation.

The shock breakout times of FeO were measured where the starting time (t_0) was

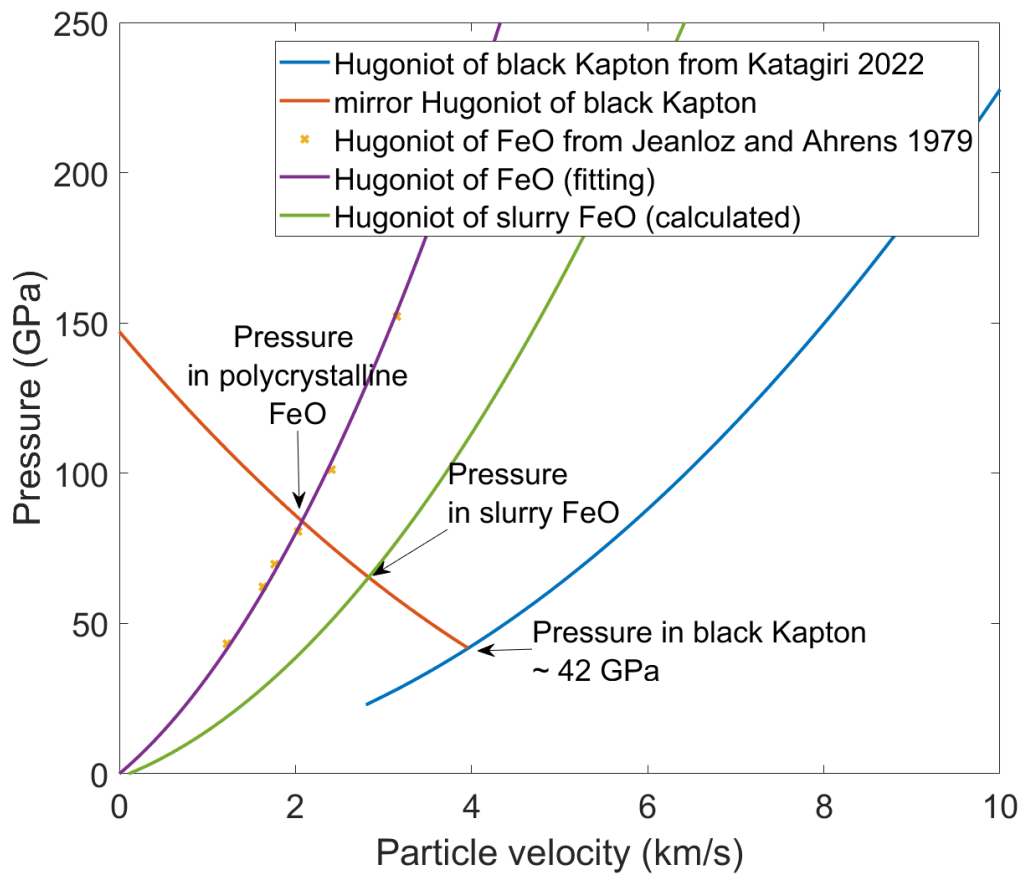


Figure 4.18: Example of impedance matching of black Kapton and polycrystalline FeO or slurry FeO. Hugoniot of black Kapton and FeO are taken from the literatures [83] [76], respectively. Hugoniot of slurry FeO is calculated based on the velocity-based mixing rules from the literature [54] from Hugoniot of FeO [76] and epoxy [84].

calibrated to the time when a shock wave arrived at the first surface of targets that are Parylene-N or black Kapton in this study. t_0 was calibrated for different streak windows of both VISAR legs at the beginning of the experiment and was used as a reference for the whole experiment. Thus, uncertainty of the shock breakout-time measurement can arise from changes in t_0 during the experiment. These changes could originate from different sources such as a target-frame displacement and a time offset in VISAR. The movement causing a systematic error was taken into account during the experiment in this study. Thus, the X-ray position on the VISAR image when the delay time $t=0$ was measured: it was expected to be the same as t_0 measured at the beginning of the experiment and the difference accounted for the t_0 changes. The comparison between the X-ray position from run 285, which was collected on the second day of the experiment, run 366 and run 367, which were collected on the third day of the experiment, is displayed in Figure 4.19. It shows that the X-ray positions on the VISAR image from both runs shifted with respect to t_0 measured at the beginning of the experiment. The X-ray signal of run 285 came later than t_0 by approximately 0.15 to 0.30 ns, whereas X-rays of run 366 and 367 start 0.05 to 0.30 ns earlier than t_0 . In addition, the shifts were different between VISAR 1 and VISAR 2 in the same run. These infer the t_0 change due to the time offset of the VISAR images between days or shots.

The t_0 change could also be observed from systematically different shock-breakout times when shooting on the same type of target with the same laser intensity. As shown in Figure 4.7, shock breakout time of FeO of the BK/FeO targets obtained from VISAR 2 with the streak window of 20 ns shows the differences at the same laser intensity. Differences could occur during data collection on different days of the experiment, where t_0 could be changed. As shown in Figure 4.20, the breakout times from the first day labeled as blue crosses were later than the second-day breakout-time labeled as red circles. The offset between two days was approximately 0.3 ns, and fluctuation on a same day is also observed. Thus, the uncertainty of t_0 is estimated at ± 0.3 ns. Apart from t_0 , these differences could additionally result from other causes such as changes in effective laser intensities during the experiment. A random error from shot-to-shot could also arise from a target such as an uneven thickness of a sample and a position of each target glued on a target frame, where the first surface plane of a target is not at the t_0 position.

Unlike the BK/FeO, the systematic shifts of the shock breakout time from FeO of the PN/FeO/Sapphire targets was not obviously observed, as shown in Figure 4.7. This could be because most of the data were collected consecutively on the first day of the experiment.

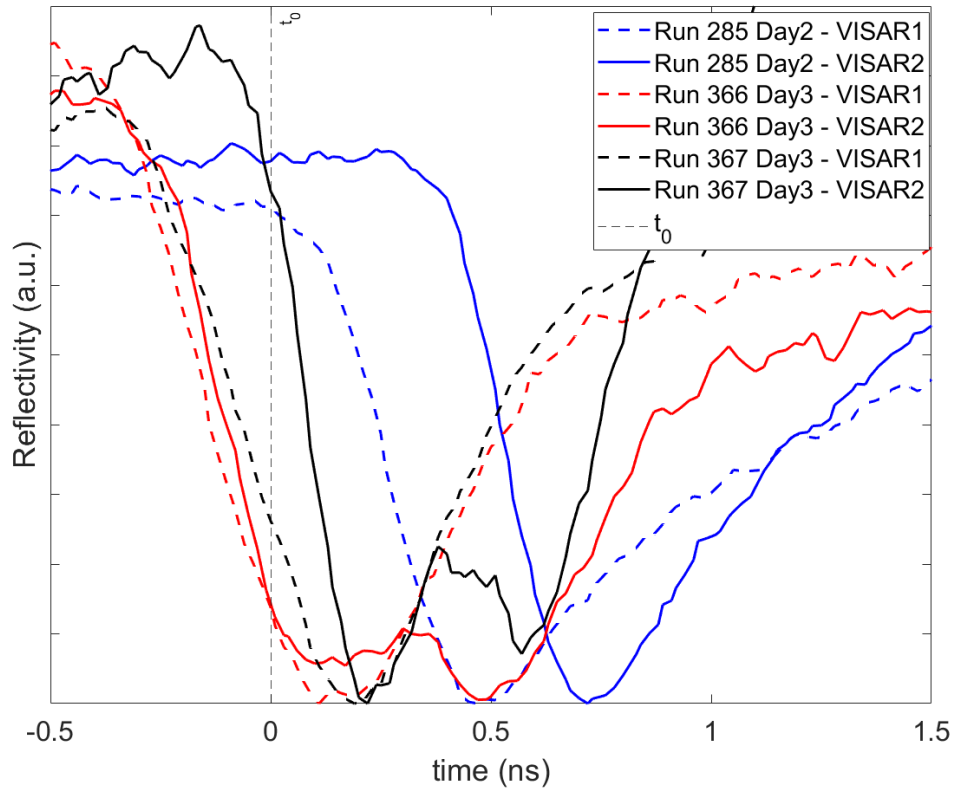


Figure 4.19: XFEL position on VISAR 1 and 2 from run 285 collected on the second day of the experiment, run 366 and run 367 collected on the third day of the experiment.

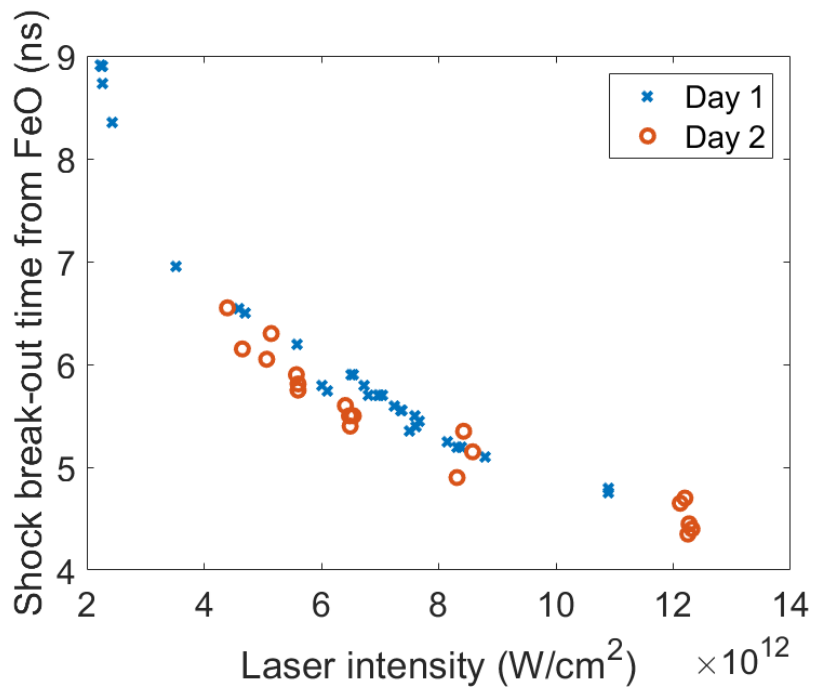


Figure 4.20: Shock breakout time from FeO of the BK/FeO targets. The data is labeled with the collected date: the first day (day 1) and the second day (day 2) of the experiment.

Only two data points were obtained on the second day: one at $5.0 \times 10^{12} \text{ W/cm}^2$ is shifted, while the other at $8.6 \times 10^{12} \text{ W/cm}^2$ follows the same trend as the other points. The shock breakout times calculated from hydrodynamic simulation were also consistent with most of the VISAR data as shown in Figure 4.11: one data point with the largest shift at $5.0 \times 10^{12} \text{ W/cm}^2$ was collected on the second day. Therefore, to compare the shock breakout time calculated from hydrodynamic simulation to the ones from VISAR, the t_0 shift should be taken into account.

To calculate pressure of FeO in the BK/FeO targets in this study, the numerical laser intensity calculated from equation $I_{\text{numerical}} = 0.45I_{\text{experiment}}$ was used for the shots with laser intensities greater than $3 \times 10^{12} \text{ W/cm}^2$. The calculated shock breakout times were 0.1 to 0.4 ns later compared to the VISAR data as shown in Figure 4.12. This is mainly because of the t_0 shift, which is estimated at $\pm 0.3 \text{ ns}$. The additional fluctuation of t_0 could also occur. Moreover, the shifts could originate from the Kapton EoS that is not completely comparable with the black Kapton used for the experiment. However, this should cause only a small uncertainty in the calculated pressure since the pressure at the solid-liquid boundary of FeO from hydrodynamic simulation and VISAR is consistent. It suggests that the pressure of FeO in the BK/FeO targets calculated from hydrodynamic simulation is valid and the uncertainty is acceptable.

Chapter 5

(Mg,Fe)O

The main goal of this section is to investigate (Mg,Fe)O under shock compression including its Hugoniot and the corresponding structural phase changes. Two shock compression experiments were performed at the LCLS MEC and the LULI2000 facility. In this thesis, only the results of the slurry targets (Mg, Fe)O are included starting from the Hugoniot EoS measurement in Section 5.1. The XRD results showing (Mg, Fe)O structures in various compositions under shock compression are presented in Section 5.2. The discussion and comparison with the literature are attached in Section 5.3.

5.1 Hugoniot EoS of slurry (Mg,Fe)O

The Hugoniot EoS of slurry (Mg,Fe)O is a key to understanding and interpreting the results in our shock compression experiment, as the slurry targets were used as main targets. The calculation of the Hugoniot of slurry materials from pure material and epoxy has been proposed and used up to approximately 100 GPa [54]. However, no EoS of the slurry targets from direct measurement has been available until now. For (Mg,Fe)O, the EoS of polycrystalline (Mg,Fe)O under shock compression were studied up to 200 GPa in two compositions: $(\text{Mg}_{0.94}, \text{Fe}_{0.06})\text{O}$ [39] and $(\text{Mg}_{0.6}, \text{Fe}_{0.4})\text{O}$ [31]. Therefore, the main goal of this experiment is to obtain Hugoniot EoS of the slurry $(\text{Mg}_{0.9}, \text{Fe}_{0.1})\text{O}$ and $(\text{Mg}_{0.6}, \text{Fe}_{0.4})\text{O}$. The results were compared to the crystalline and calculated slurry (Mg, Fe)O.

The Hugoniot EoS measurement of the slurry $(\text{Mg}_{0.9}, \text{Fe}_{0.1})\text{O}$ and $(\text{Mg}_{0.6}, \text{Fe}_{0.4})\text{O}$ was carried out at the LULI2000 facility. The experimental setups are described in Section 3.4 and the target design is illustrated as Figure 3.9. The slurry targets were prepared with the powder synthesized in Section 2.2. The targets were shot with different laser intensities ranging from 4.0×10^{12} to 4.0×10^{13} W/cm² to cover a large pressure range and to reach

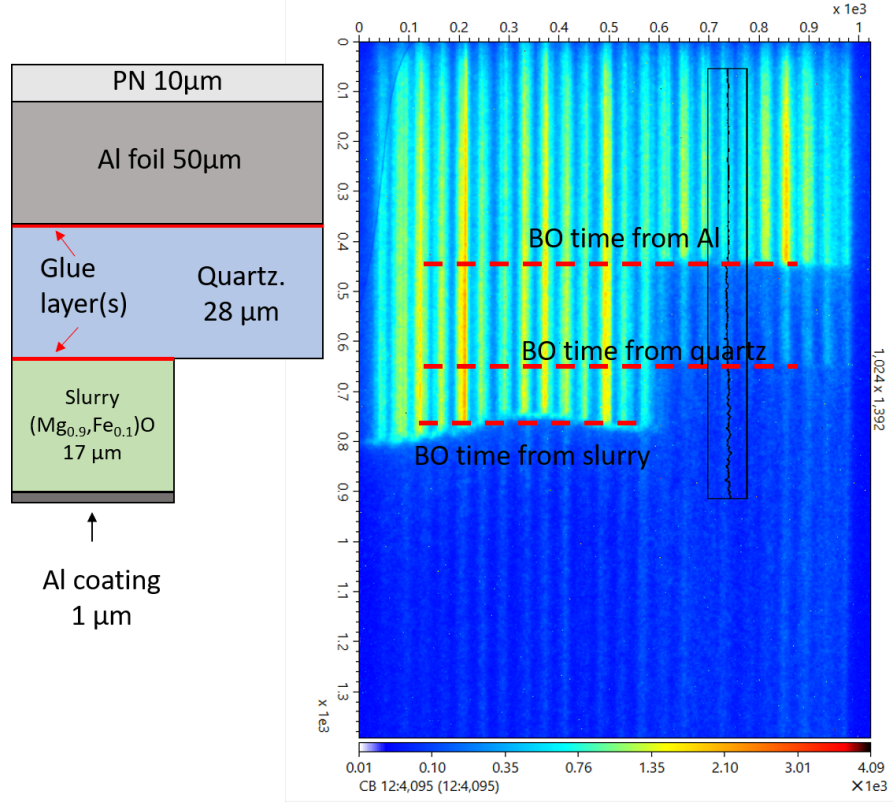


Figure 5.1: An example of the target configuration (left) and the corresponding VISAR image from VISAR2 (right). The red dash lines indicate breakout time from each layer of the target.

a high pressure above 200 GPa inside the slurry (Mg, Fe)O.

An example of the VISAR image from VISAR2 compared to the target configuration is shown in Figure 5.1. On the right side, the shock propagation time in quartz was obtained from the breakout times from Al and quartz. As shown in Figure 5.2, the breakout times from Al and quartz plotted with laser intensities are consistent: the breakout times become earlier when increasing the laser intensity. The shock propagation time and the quartz thickness were then used for the calculation of U_s in quartz. These values can provide further information such as U_p and the pressure of the quartz, since the Hugoniot of the quartz is known. Examples of the Hugoniot of quartz taken from the literature [85][86][87][84] are plotted in Figure 5.3. In this study, the Hugoniot EoS of quartz from Knudson et al. 2013 [87] was used as it fits the data at both low and high pressures. The U_s - U_p relation is as follows:

$$U_s = 1.754 + 1.862U_p - (3.364 \times 10^{-2}) U_p^2 + (5.666 \times 10^{-4}) U_p^3. \quad (5.1)$$

The pressure of the quartz at the different laser intensities was calculated as shown in Fig-

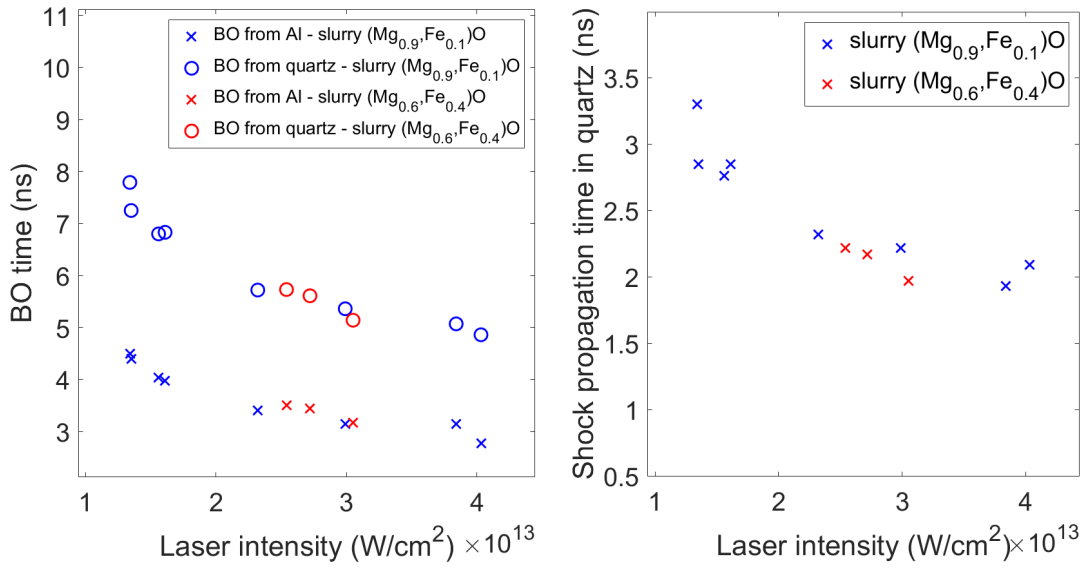


Figure 5.2: Relation between laser intensity and shock breakout time from Al and quartz (left) and shock propagation time in quartz (right).

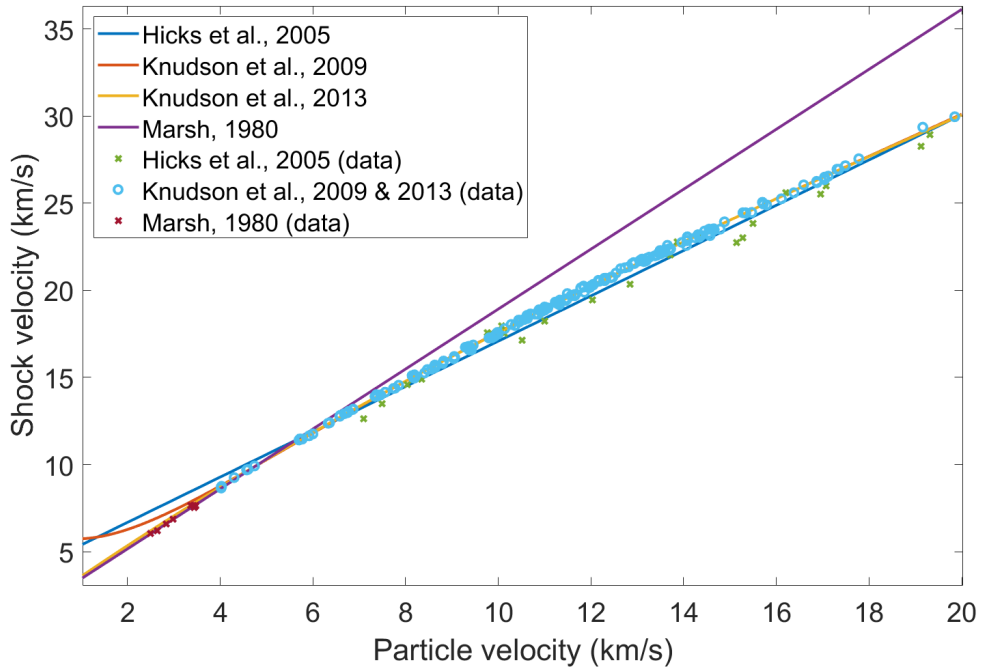


Figure 5.3: Hugoniot $P-U_p$ relation of quartz from the literatures [85][86][87][84].

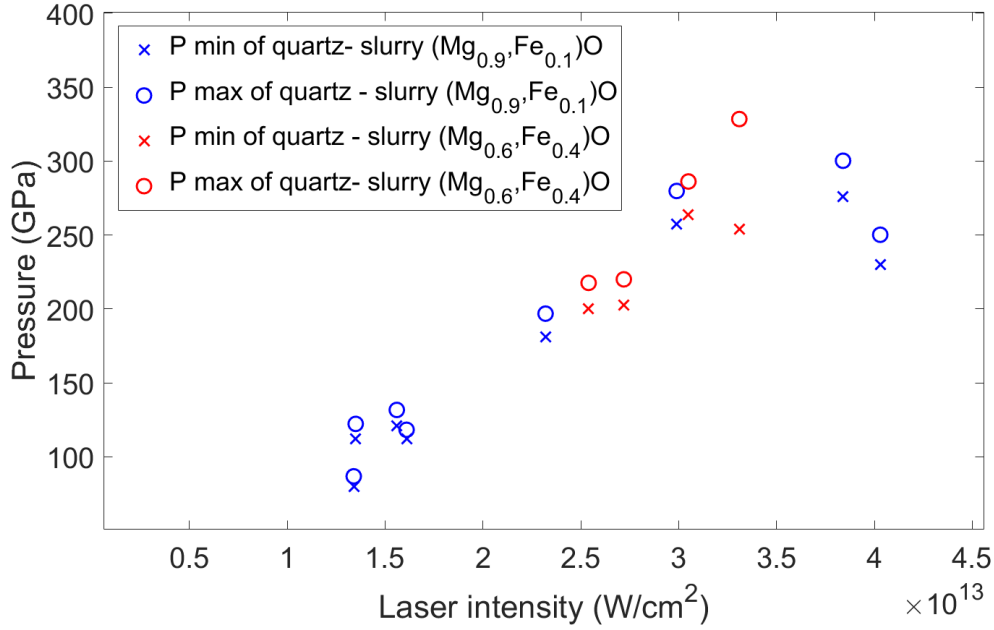


Figure 5.4: Relation between pressure of quartz calculated from U_s and laser intensities.

Figure 5.4. The maximum pressure at approximately 350 GPa of quartz was reached with the laser intensity of 4×10^{13} W/cm 2 . At a pressure and temperature of approximately 200 GPa and 10000K along the Hugoniot of quartz, the shock reflectivity in quartz, which is in bonded liquid phase, becomes 2% and increases at higher pressures and temperatures [88]. In this experiment, at quartz pressures greater than 250 GPa, U_s in quartz was recorded by reflection of a shock front in five runs. An example of a U_s profile extracted from VISARs in Neutrino software is shown in Figure 5.5. The refractive indices of quartz at 1064 and 532 nm are 1.534 and 1.547 [89], respectively. These values were used as input in the Neutrino software to correct for a true velocity from the apparent velocity. The U_s in quartz from the profile ranges from 13.4 to 16.0 km/s. It also shows a decay in U_s while propagating through the quartz. Therefore, the velocity at the interface before entering the slurry (Mg, Fe)O is 13.4 km/s. This velocity was used for impedance matching of the five runs in the next step since it gives a more accurate pressure for the slurry (Mg,Fe)O. In addition, the U_s calculated from the shock propagation time in quartz (1.93 ns) and thickness (28 μm) is 14.5 km/s, which is approximately an average U_s from the velocity profile. The uncertainty of the thickness of the quartz could also be estimated from these average U_s in quartz extracted from the velocities profile of the five runs: the thickness ranges from 27 to 28 μm i.e. 27.5 ± 0.5 μm .

The shock breakout time of the slurry (Mg,Fe)O can be obtained from the left side of the VISAR image as shown in Figure 5.1. An uneven breakout time was observed which

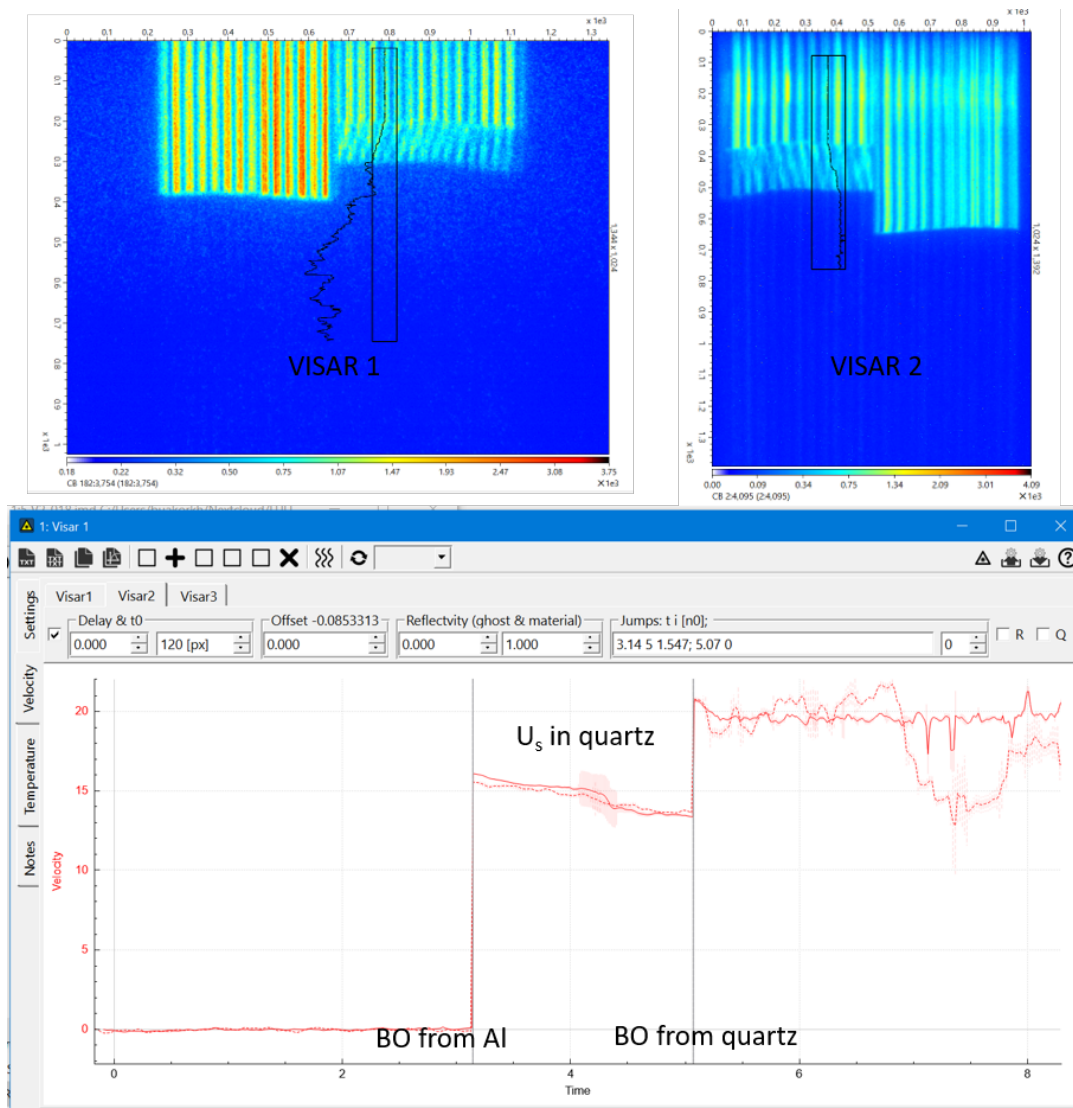


Figure 5.5: VISAR images of run 18 and the extracted velocity profile from Neutrino software. The velocity profile corresponds to U_s in quartz.

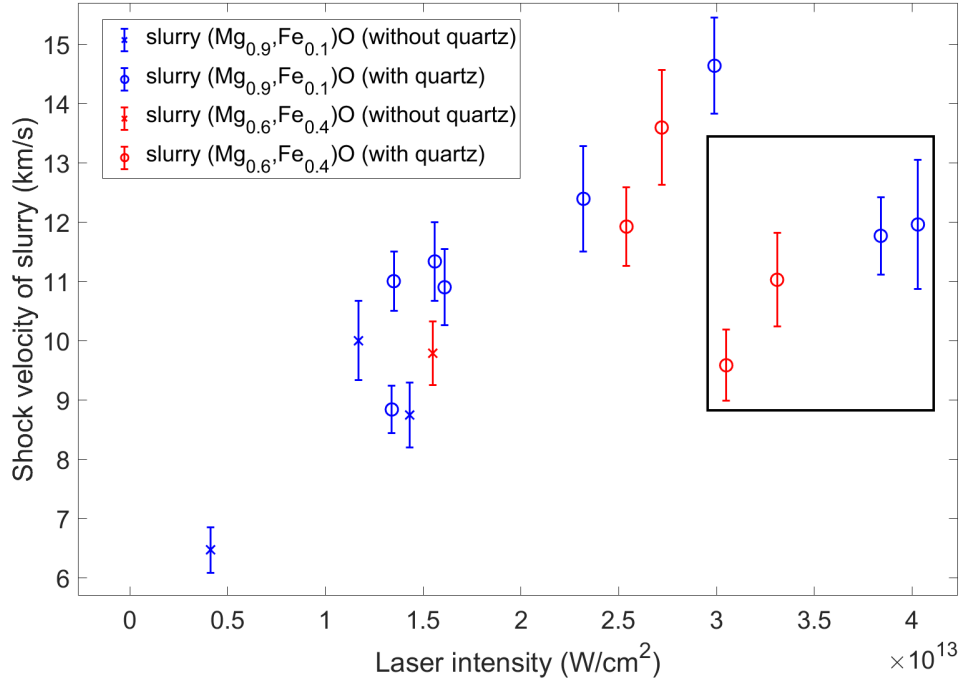


Figure 5.6: Relation between U_s in slurry ($\text{Mg}_{0.9}, \text{Fe}_{0.1}\text{O}$) and ($\text{Mg}_{0.6}, \text{Fe}_{0.4}\text{O}$) and laser intensity shot on the targets with and without a quartz window.

could either be caused by inhomogeneity of slurry thickness or a shock-wave non-planarity or both. The earliest time was chosen as the representative shock breakout time. U_s were then calculated from shock propagation time and the corresponding slurry thickness. The results are plotted as a function of laser intensity as shown in Figure 5.6. The results show that U_s in the slurry (Mg, Fe)O becomes greater while increasing the laser intensity to the laser intensity of $3.5 \times 10^{13} \text{ W/cm}^2$ for the slurry ($\text{Mg}_{0.9}, \text{Fe}_{0.1}\text{O}$) and $3.0 \times 10^{13} \text{ W/cm}^2$ for slurry ($\text{Mg}_{0.6}, \text{Fe}_{0.4}\text{O}$), which correspond to a pressure in quartz of up to approximately 300 GPa. At higher laser intensity, the shock velocities are dropping. To interpret this behaviour, the pressure and U_p of the slurry at these points are needed.

The U_p in quartz, which is calculated from U_s with equation 5.1, and U_s in slurry (Mg,Fe)O were used for the pressure calculation in slurry (Mg,Fe)O. An example of the impedance matching performed in slurry ($\text{Mg}_{0.9}, \text{Fe}_{0.1}\text{O}$) is shown in Figure 5.8. Here U_s in the slurry ($\text{Mg}_{0.9}, \text{Fe}_{0.1}\text{O}$) is 10.67-12.00 km/s and U_s in quartz is 9.78-10.14 km/s, which corresponds to U_p in quartz of 4.67-4.90 km/s. First, the Hugoniot $U - s - U_p$ from equation 5.1 is calculated as pressure (P)- U_p space using Rankine-Hugoniot shock equation 3.2 as follows:

$$P = \rho_0 (a_0 U_p + a_1 U_p^2 + a_2 U_p^3 + a_3 U_p^4), \quad (5.2)$$

where an initial pressure (P_0) is zero. An initial density (ρ_0) is 3.174 g/cm^3 for slurry

(Mg_{0.9}, Fe_{0.1})O and 3.766 g/cm³ for slurry (Mg_{0.6}, Fe_{0.4})O. a_0 , a_1 , a_2 and a_3 are 1.754, 1.862, -3.364×10^{-2} , and 5.666×10^{-4} , respectively, regarding to equation 5.1. This Hugoniot P- U_p of quartz is plotted as a red line in Figure 5.8. The calculated U_p and the pressure in quartz were obtained from VISAR and are written as $U_{p,qtz}$ and P_{qtz} , respectively. At the pressure P_{qtz} , the density of quartz (ρ_1) can be calculated from equation 3.1 rearranged as follows:

$$\rho_1 = \frac{\rho_0 U_{s,quartz}}{U_{s,quartz} - U_{p,quartz}} \quad (5.3)$$

The mirror reflection of the secondary Hugoniot with the initial condition ρ_1 crossing the P- U_p Hugoniot at ($U_{p,qtz}$, P_{qtz}) can be calculated as follows:

$$P = c_0 + c_1 U_p + c_2 U_p^2 + c_3 U_p^3 + c_4 U_p^4, \quad (5.4)$$

where

$$c_0 = \rho_1 (a_0 k + a_1 k^2 + a_2 k^3 + a_3 k^4), \quad (5.5)$$

$$c_1 = -\rho_1 (a_0 + 2a_1 k + 3a_2 k^2 + 4a_3 k^3), \quad (5.6)$$

$$c_2 = \rho_1 (a_1 + 3a_2 k + 6a_3 k^2), \quad (5.7)$$

$$c_3 = -\rho_1 (a_2 + 4a_3 k), \quad (5.8)$$

$$c_4 = \rho_1 a_3. \quad (5.9)$$

k is calculated from $k = U_{p,quartz} + U_1$. U_1 is obtained by solving for U_p of equation 5.2, when $P = P_{qtz}$ and substituting ρ_0 with ρ_1 .

Since there are maximum and minimum U_s in quartz from uncertainty of the quartz thickness, the corresponding ($U_{p,qtz}$, P_{qtz}) range between the minimum ($U_{p,qtz,min}$, $P_{qtz,min}$) and maximum values ($U_{p,qtz,max}$, $P_{qtz,max}$). Therefore, the two mirror Hugoniot lines that cross at ($U_{p,qtz,min}$, $P_{qtz,min}$) and ($U_{p,qtz,max}$, $P_{qtz,max}$) are plotted as a solid green and blue line in Figure 5.8. Then, the Rayleigh line with the slope calculated from the slurry density and U_s in the slurry from VISAR, i.e. slope = $\rho_0 U_{s,slurry}$, is drawn to cross the mirror Hugoniot. It crosses at ($U_{p,slurry}$, P_{slurry}) and $U_{p,slurry}$ is calculated by solving for U_p from the following equation:

$$0 = c_0 + (c_1 - \rho_0 U_{s,slurry}) U_p + c_2 U_p^2 + c_3 U_p^3 + c_4 U_p^4. \quad (5.10)$$

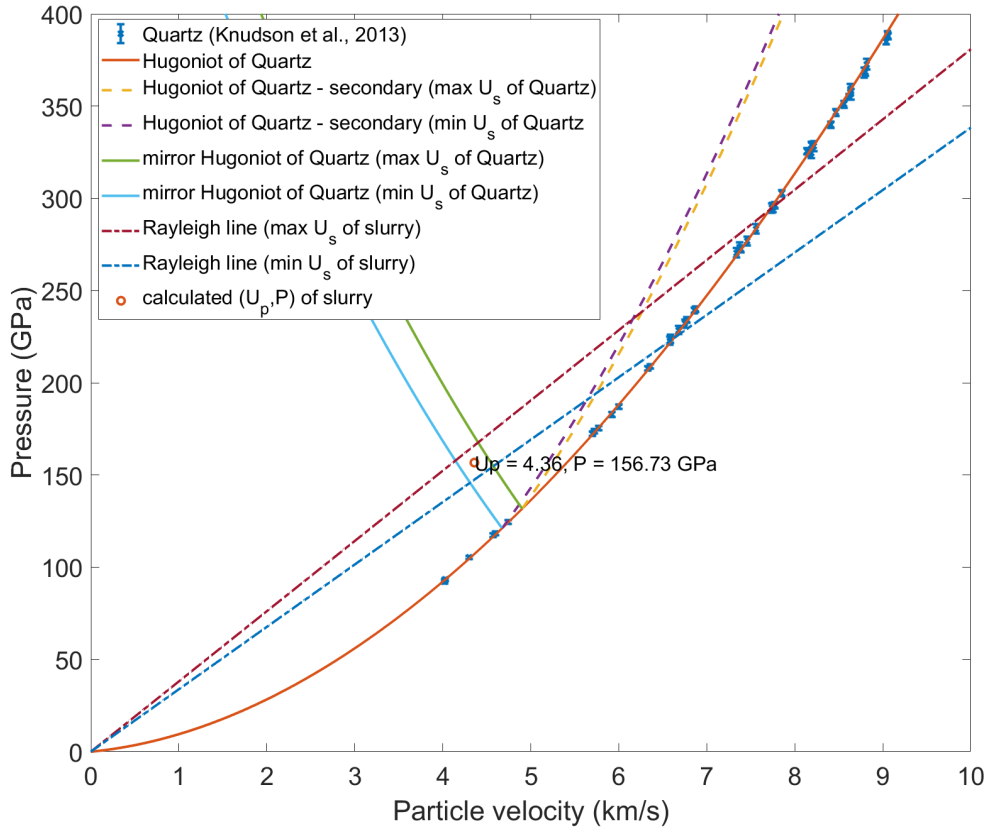


Figure 5.7: Example of impedance matching technique performed for run 7 of slurry (Mg_{0.9}, Fe_{0.1})O, when using a mirror reflection of the secondary Hugoniot

Then, P_{slurry} can be calculated from equation 3.2 as follows:

$$P_{slurry} = \rho_0 U_{s,slurry} U_{p,slurry}. \quad (5.11)$$

Because two $U_{s,slurry}$ and two $U_{p,qtz}$ are obtained from VISAR, there are four crossing points $(U_{p,slurry}, P_{slurry})$ of the Rayleigh lines and the mirror Hugoniot lines. The average value of $(U_{p,slurry}, P_{slurry})$ and the related error bar are calculated from these. For example, $U_{p,slurry}$ and P_{slurry} calculated from impedance matching shown in Figure 5.7 are 4.36 ± 0.22 km/s and 156.73 ± 10.91 GPa, respectively. Table of $(U_{p,slurry}, P_{slurry})$ calculated for all the runs is attached as Table A.3 in Appendix A.

Apart from the method described above, impedance matching was also implemented using a mirror reflection of the principal Hugoniot instead of the secondary Hugoniot and the results were compared. An example of impedance matching is illustrated in Figure 5.8. $U_{p,slurry}$ and P_{slurry} from the impedance matching are 4.25 ± 0.24 km/s and 152.78 ± 10.07 GPa. The results show a small difference of calculated $U_{p,slurry}$ and P_{slurry}

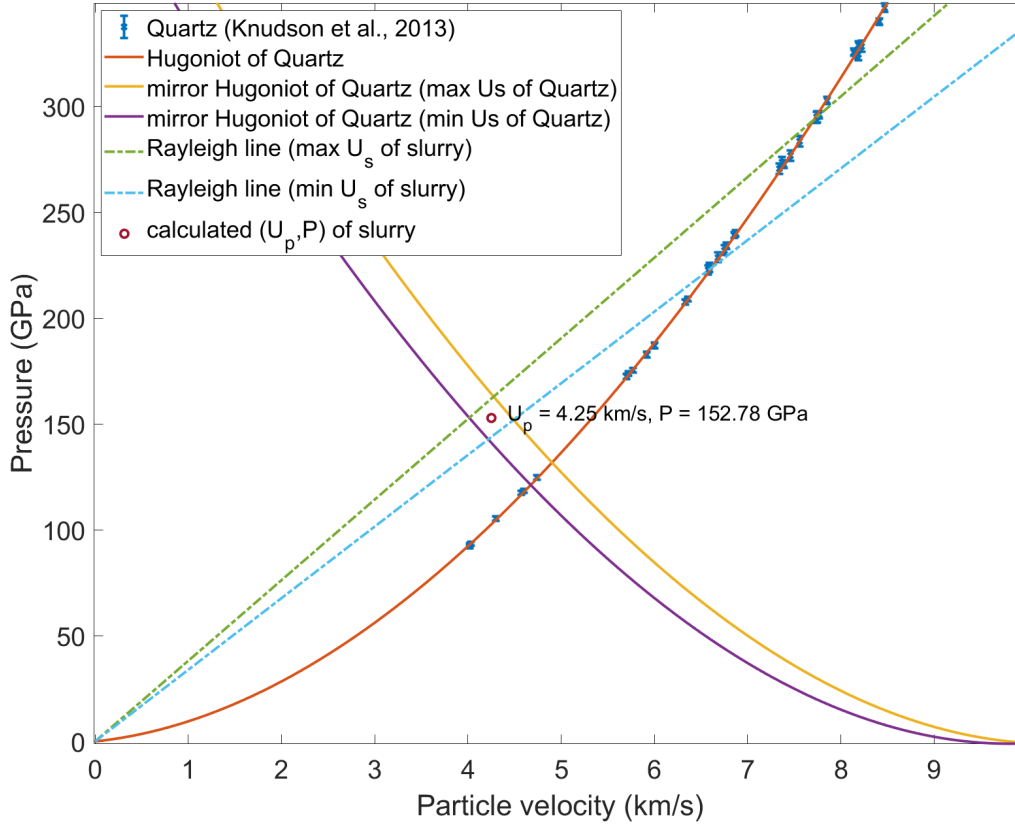


Figure 5.8: Example of impedance matching technique performed for run 7 of slurry $(\text{Mg}_{0.9}, \text{Fe}_{0.1})\text{O}$, when using a mirror reflection of the principal Hugoniot.

when using different mirror Hugoniot curves at this pressure.

The obtained Hugoniot relations plotted as U_s-U_p and $P-U_p$ spaces of slurry $(\text{Mg}_{0.9}, \text{Fe}_{0.1})\text{O}$ and slurry $(\text{Mg}_{0.6}, \text{Fe}_{0.4})\text{O}$ calculated from impedance matching using the mirror reflection of principal and secondary Hugoniot are depicted in Figure 5.9. The results show a small difference from the error bar for the entire $U_{p,slurry}$ and P_{slurry} range, so one can use either method for further calculations. The impedance matching technique using the mirror reflection of the secondary Hugoniot was chosen for the data presented here. The results of Figure 5.9 show that the maximum pressure was reached at approximately 300 GPa. A discontinuity of both U_s-U_p and $P-U_p$ Hugoniot data is observed in slurry $(\text{Mg}_{0.9}, \text{Fe}_{0.1})\text{O}$ at U_s above 15 km/s, which corresponds to a pressure of 250 to 300 GPa. For slurry composition $(\text{Mg}_{0.9}, \text{Fe}_{0.1})\text{O}$, U_s-U_p linear regression was performed before the discontinuity. In general, U_s-U_p relations with no phase transition can be described as a linear relation as follows [90]:

$$U_s = C_0 + SU_p. \quad (5.12)$$

C_0 is the bulk sound speed at zero pressure for pure materials and S is an empirical pa-

parameter typically in a range of 1.1 to 1.6 [90][91]. In case of porous material, mixtures, alloys, and materials with a large strength effect, C_0 varies. For example, porosity causes smaller C_0 compared to a volume sound speed at zero pressure [91]. For single crystal (Mg_{0.9}, Fe_{0.1})O, the bulk sound speed was measured to be 6.57 km / s [36]. In our case, the bulk sound speed of the slurry (Mg_{0.9}, Fe_{0.1})O is unknown and is expected to be lower than that of the single crystal. The following U_s - U_p relation is obtained with $R^2 = 0.8873$ for U_s up to 15 km/s:

$$U_s = 1.4355U_p + 4.5962. \quad (5.13)$$

$C_0 = 4.5962$ km / s, which is less than the bulk sound speed of (Mg_{0.9}, Fe_{0.1})O as expected. For the slurry (Mg_{0.6}, Fe_{0.4})O, it is very difficult to find a suitable curve using the current data set. Data at low pressures are needed for interpretation.

In addition to VISAR, XRD measurements were performed for some shots of both slurry compositions, i.e. (Mg_{0.9}, Fe_{0.1})O and (Mg_{0.6}, Fe_{0.4})O. The purpose of this study was to obtain information on the structures and density of (Mg,Fe)O along its Hugoniot. To analyze the data, XRD calibration was first performed in PyFAI software [92] and Dioptas software [93]. Here, Au which was part of the different target types used for ramp compression shots, was used as an internal standard material. The multilayer target consists of Ti/ CVD-diamond/ Au/ slurry (Mg_{0.9}, Fe_{0.1})O/ Al/ CVD-diamond/Al(half). XRD images of the experiment and the simulation at ambient conditions from one of the five image plates are shown as Figure 5.10 . The image shows IP2 that covers 2θ of approximately 35° to 85° . The calibration was quite difficult, as only two peaks of Au were clearly observed. Calibrations had to be performed for each run, as the peaks could be shifted because IPs were taken in and out for readout between shots. Therefore, reference peaks such as the ambient (Mg, Fe)O had to be checked for each run before analysis. The volume and density of (Mg_{0.9}, Fe_{0.1})O and (Mg_{0.6}, Fe_{0.4})O in the ambient environment should be the same as those mentioned in Section 2.2.

Integrated XRD lineouts of three shock compression shots of (Mg_{0.9}, Fe_{0.1})O are plotted in Figure 5.11. Laser intensities as well as X-ray probing times of the corresponding shot are labeled as relative time to the shock breakout time. The X-ray pulse length is approximately 1.5 ns, so the probing time is shown as a time duration. The ambient (Mg_{0.9}, Fe_{0.1})O XRD from IP2 includes the reflections from (111), (200), and (220) planes. The most intense peak (200) was chosen for peak fitting with the pseudo-Voigt function in the Origin software package. The (200) peak of (Mg_{0.9}, Fe_{0.1})O was observed at 52.3° which corresponds to the volume and density of 74.7^3 and 3.86 g/cm³. The results

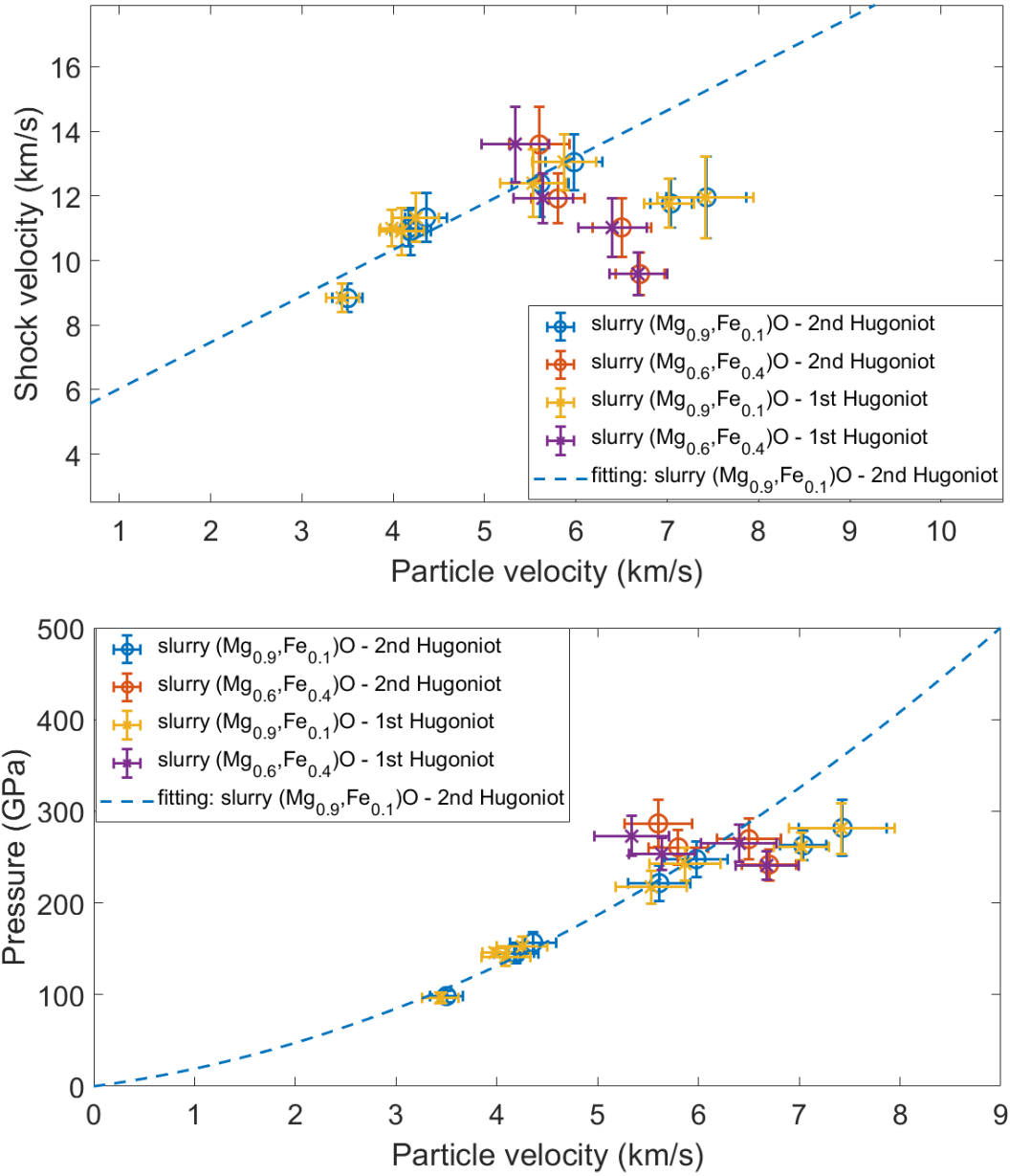


Figure 5.9: Hugoniot of slurry (Mg_{0.9}, Fe_{0.1})O and slurry (Mg_{0.6}, Fe_{0.4})O plotted in U_s - U_p (left) and pressure- U_p (right). $U_s = 1.4355U_p + 4.5962$ was obtained from linear regression for U_s - U_p relation of slurry (Mg_{0.9}, Fe_{0.1})O.

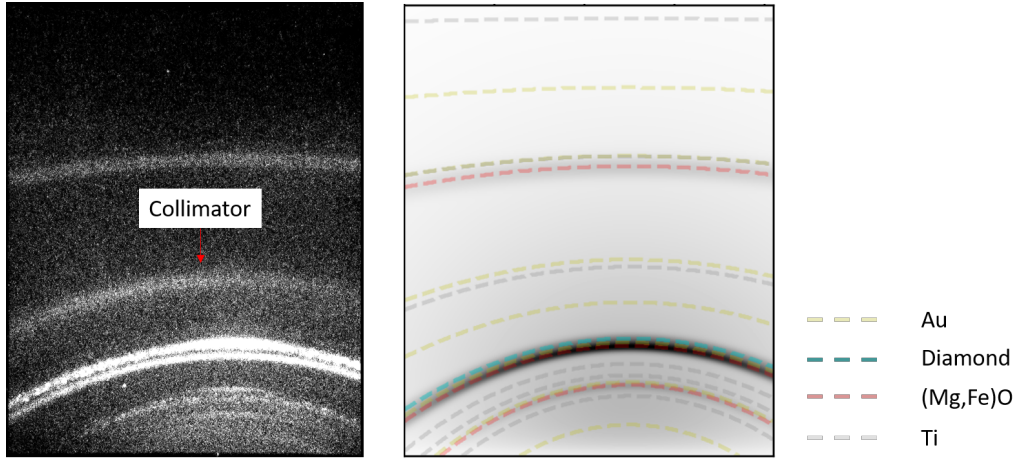


Figure 5.10: XRD images of IP2 covering 2θ of approximately 35° to 85° used for calibration taken from the experiment (left) and the simulation (right).

show that only the B1 structure of $(\text{Mg}_{0.9}, \text{Fe}_{0.1})\text{O}$ was present. One shot at a laser intensity of $1.43 \times 10^{13} \text{ W/cm}^2$ was partly probed at the shock-released time and shows a very weak XRD with a large background. This might show that the sample was liquid on the release path. For $(\text{Mg}_{0.6}, \text{Fe}_{0.4})\text{O}$, the XRD reflection from (200) plane at ambient from IP2 is at 2θ of 51.7° . The corresponding volume and density are 77.1 \AA^3 and 4.56 g/cm^3 . One shock compression shot probed at the shock release time shows only the B1 structure. The pressure of slurry $(\text{Mg}_{0.9}, \text{Fe}_{0.1})\text{O}$ in full compression for a shot at the target with a quartz window at $1.4 \times 10^{13} \text{ W/cm}^2$ was obtained directly from the impedance matching, while the pressures of the other target without quartz window at $1.4 \times 10^{13} \text{ W/cm}^2$ were calculated from equations 5.11 and 5.13: the initial density of the slurry $(\text{Mg}_{0.9}, \text{Fe}_{0.1})\text{O}$ is 3.174 g/cm^3 . The pressure of the corresponding density from the XRD probed at shock release time cannot be directly obtained with the same methods. The density of the XRD peak fitting and the calculated pressure are shown in Table A.4. The pressure-density from this experiment is further discussed in Section 5.3.

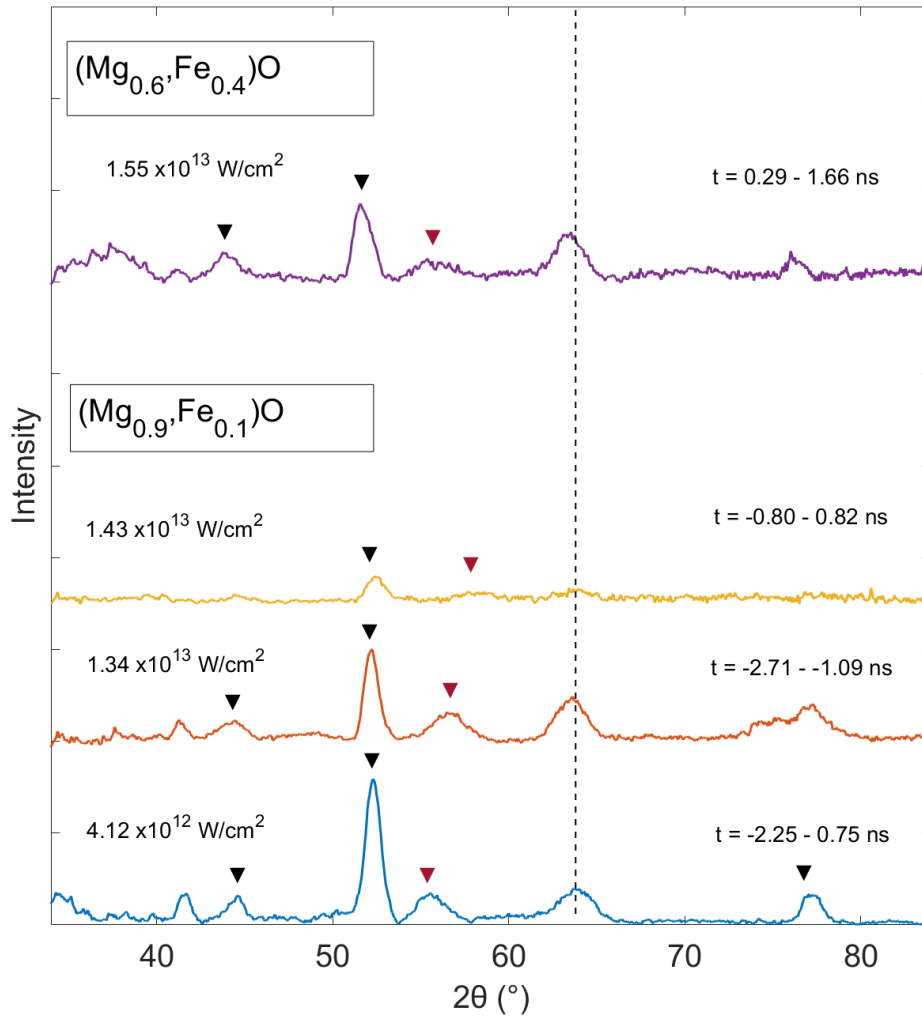


Figure 5.11: Integrated XRD lineouts of $(\text{Mg}_{0.9}, \text{Fe}_{0.1})\text{O}$ and $(\text{Mg}_{0.6}, \text{Fe}_{0.4})\text{O}$ collected by IP2 at various laser intensities. Black reverted triangles are referred to as reflections from (111), (200), and (220) planes sorted from low to high angles of 2θ and red reverted triangles are compressed (200) peaks. A dash line is labeled as a collimator.

5.2 (Mg,Fe)O structures under shock compression

The main goal of the shock compression experiment of (Mg,Fe)O performed at the MEC of LCLS is to probe structural changes along the Hugoniot starting from B1 structures along the solid solution. Slurry samples were prepared with four different compositions of (Mg,Fe)O from reference [59]: (Mg_{0.9}, Fe_{0.1})O, (Mg_{0.6}, Fe_{0.4})O, (Mg_{0.4}, Fe_{0.6})O, and (Mg_{0.2}, Fe_{0.8})O. This aims to compare the different phase stability that is affected by different Fe or Mg contents. The shock compression was launched by 5-ns flat-top laser with the maximum energy of 40J. The target configuration is BK/slurry (Mg,Fe)O, where some targets were glued with sapphire or quartz windows. Two diagnostics, which are XRD measurement at 13 keV and VISAR, were performed as described in Section 3.3.

Integrated XRD lineouts of (Mg_{0.9}, Fe_{0.1})O at ambient and under shock loading shot at different laser intensities are shown in Figure 5.12. X-ray delays were also adjusted such that the XRD was probed before, during, or after a shock breakout time. The relative time to the breakout time obtained from VISAR is represented below the XRD lineouts, where $t = 0$ ns indicates probing exactly at the shock breakout time from slurry (Mg,Fe)O. The ambient XRD from Quad 0 includes reflection from (111) and (200) planes, which are at Q value of 2.58 \AA^{-1} and 2.97 \AA^{-1} , respectively. The corresponding volume and density are 74.9 \AA^3 and 3.85 g/cm^3 . The results of shock-compressed shots show that only the B1 structure was observed at fully shock-compressed shots up to the maximum laser intensity of $1.16 \times 10^{13} \text{ W/cm}^2$. The maximum pressure of 172 GPa was reached at this laser intensity: the methods for pressure calculation are described later in this section. At 1.3 ns after the shock breakout, the broad feature consisting of at least two peaks was detected in the shot with the maximum laser intensity: this was also obviously observed in the 2D XRD image in Figure 5.13. These can be caused by (Mg_{0.9}, Fe_{0.1})O at different pressures or/and temperatures throughout the target. The other assumption is that it arises from different compositions decomposed from (Mg_{0.9}, Fe_{0.1})O during the shock release.

Figure 5.14 shows the integrated XRD lines of (Mg_{0.6}, Fe_{0.4})O from the shock compression shot and at ambient obtained from Quad 0. The reflections from (111) and (200) at ambient shot are at Q of 2.56 \AA^{-1} and 2.95 \AA^{-1} , the corresponding volume and density are 76.6 \AA^3 and 4.58 g/cm^3 . The results show that only B1 structure was observed up to the maximum laser intensity of $1.16 \times 10^{13} \text{ W/cm}^2$, which is similar to what being observed in (Mg_{0.9}, Fe_{0.1})O. The maximum pressure of 178 GPa was reached: the methods for pressure calculation are described later in this section. For this composition, some targets were glued with a quartz or a sapphire window. The relative time of XRD probing

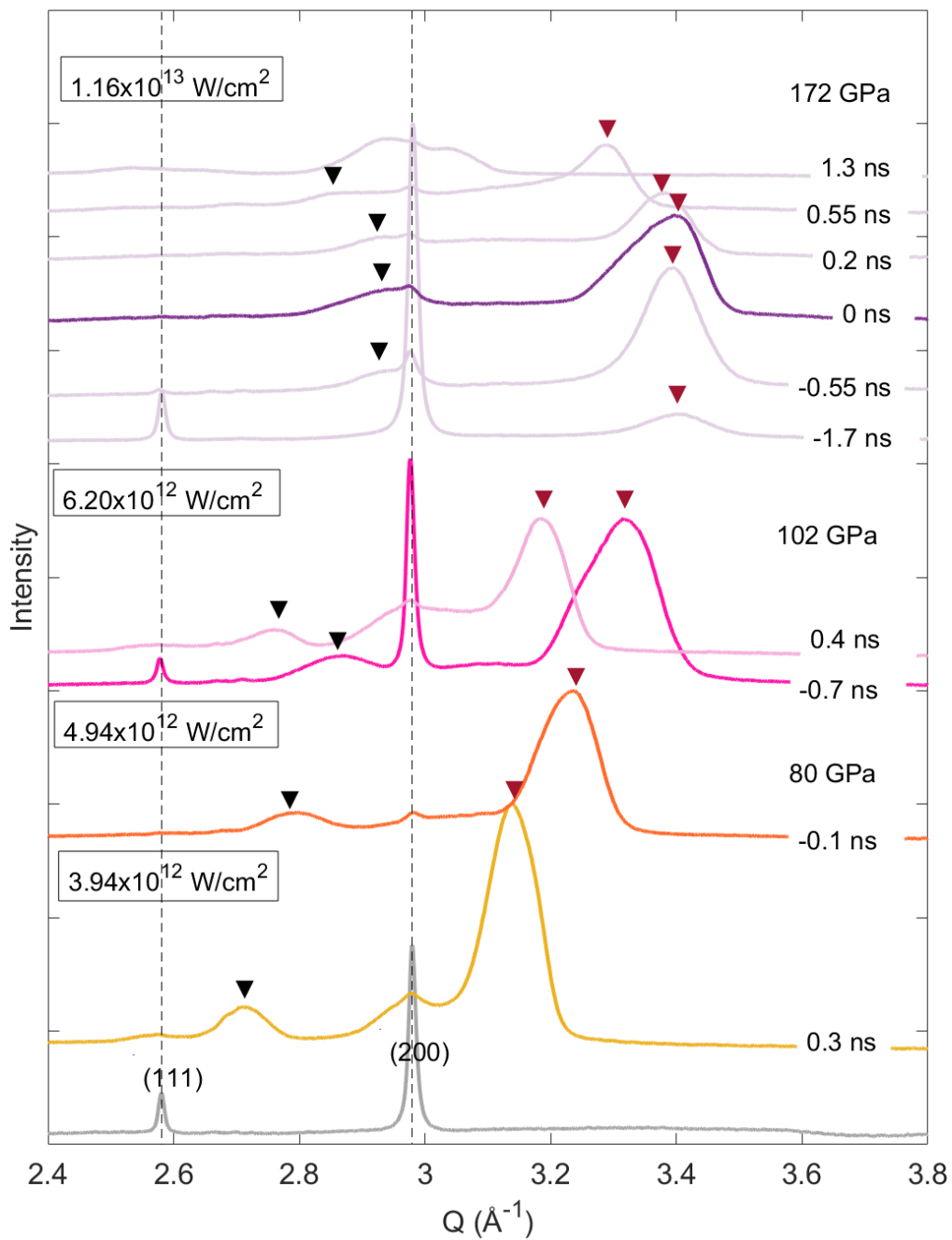


Figure 5.12: Integrated XRD lineouts of $(\text{Mg}_{0.9}, \text{Fe}_{0.1})\text{O}$ under shock compression at various laser intensities collected by Quad 0 detector. The pressures correspond to the pressure reached at the fully shock-compression by using the corresponding laser intensities. $(\text{Mg}_{0.9}, \text{Fe}_{0.1})\text{O}$ at ambient includes reflections from (111) and (200) planes shown as black dash lines. The compressed (111) and (200) peaks are labeled as black and red reverted triangles, respectively.

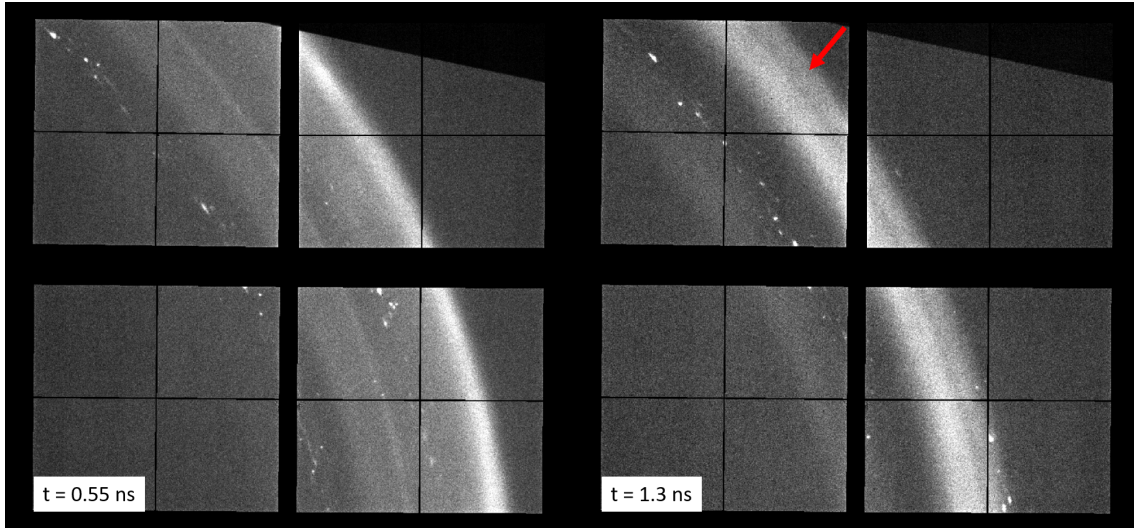


Figure 5.13: 2D XRD images of the shots with a laser intensity of $1.16 \times 10^{13} \text{ W/cm}^2$ at 0.55 and 1.3 ns after the shock breakout time.

compared to the shock breakout time was calculated. The targets with windows show an inconsistency between the XRD and the corresponding relative time. For example, the XRD of the shot with a laser intensity of $6.0 \times 10^{12} \text{ W/cm}^2$ on the target with a quartz window probed at $t = -0.1 \text{ ns}$ shows similarity to the XRD of the target without a window probed at $t = 0.7 \text{ ns}$. This indicates an inaccurate shock breakout time of a target with a window observed from VISAR. The breakout time from a glue layer between slurry and window was taken instead of a breakout time from a slurry. These discrepancies are also observed in the shots with a laser intensity of $8.4 \times 10^{12} \text{ W/cm}^2$, where all the targets were glued to sapphire windows resulting in inconsistent XRD time series. However, this complication could also arise from multiple shock reflection and transmission between a sample and a window: hydrodynamic simulation is needed to get better insights to this observed behavior.

XRD was obtained for three shock compression shots with a laser intensity of $1.16 \times 10^{13} \text{ W/cm}^2$ on slurry $(\text{Mg}_{0.4}, \text{Fe}_{0.6})\text{O}$. The results from Quad 0 are shown as Figure 5.15. At ambient, reflections from (100) and (200) are at Q of 2.55 \AA^{-1} and 2.94 \AA^{-1} which are only slightly different from $(\text{Mg}_{0.6}, \text{Fe}_{0.4})\text{O}$. The shock compression results show only evidence for the B1 structure at shock breakout and during shock release. The obtained density at the shock breakout time is 7.60 g/cm^3 .

Integrated XRD lineouts of $(\text{Mg}_{0.2}, \text{Fe}_{0.8})\text{O}$ at ambient and during shock compression are shown as Figure 5.16. The reflections from (111) and (200) are at Q of 2.55 \AA^{-1} and 2.94 \AA^{-1} . The volume and density of $(\text{Mg}_{0.2}, \text{Fe}_{0.8})\text{O}$ at ambient were calculated to be 77.5 \AA^3 and 5.60 g/cm^3 . Similar to the other compositions, only the B1 structure was

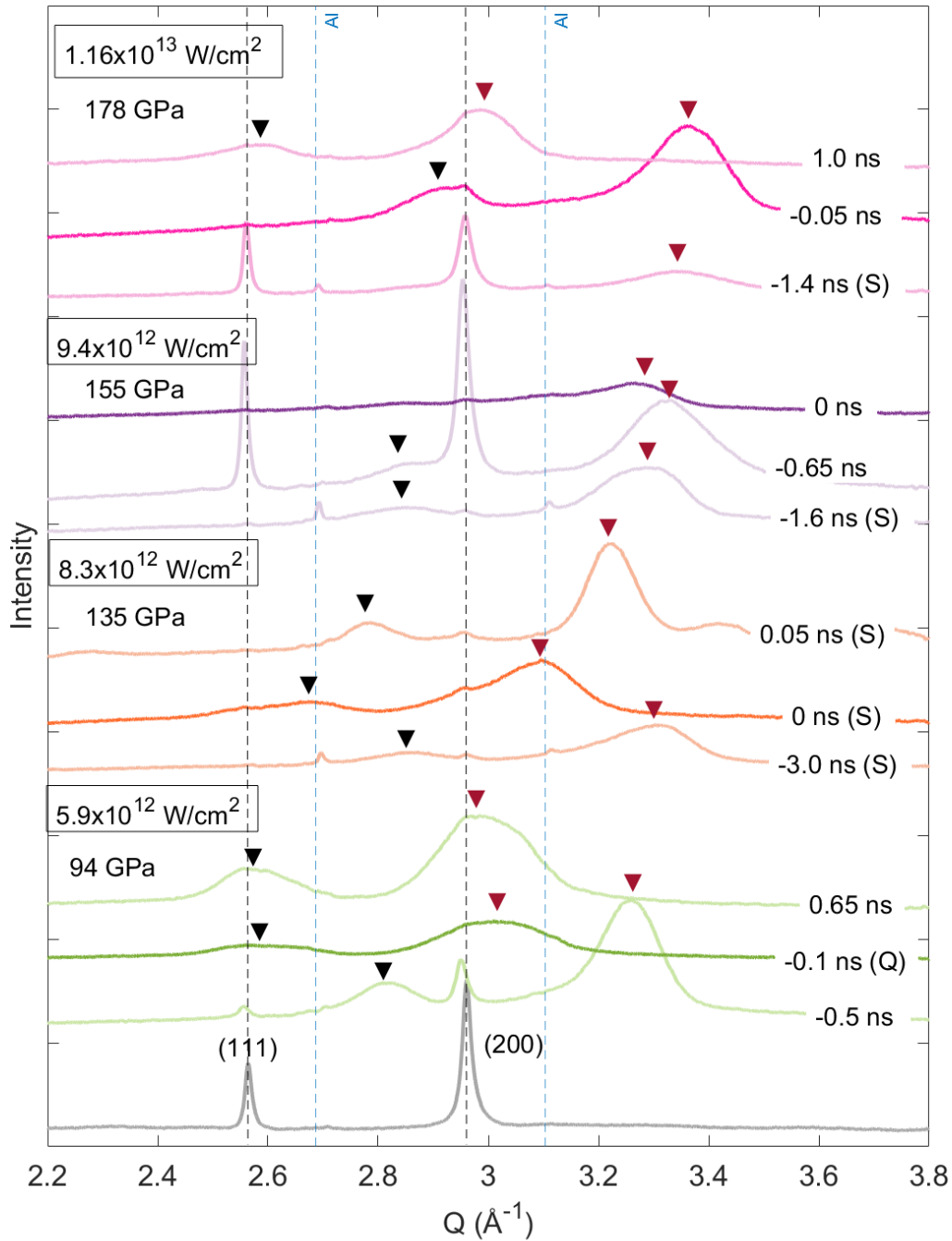


Figure 5.14: Integrated XRD lineouts of $(\text{Mg}_{0.6}, \text{Fe}_{0.4})\text{O}$ under shock compression at various laser intensities collected by Quad 0 detector. The pressures correspond to the pressure reached at the fully shock-compression by using the corresponding laser intensities. $(\text{Mg}_{0.6}, \text{Fe}_{0.4})\text{O}$ at ambient includes reflections from (111) and (200) planes shown as black dash lines. The compressed (111) and (200) peaks are labeled as black and red reverted triangles, respectively. Q and S are referred to as a target with a quartz or a sapphire window. Al peaks from a sample frame are at blue dash line positions.

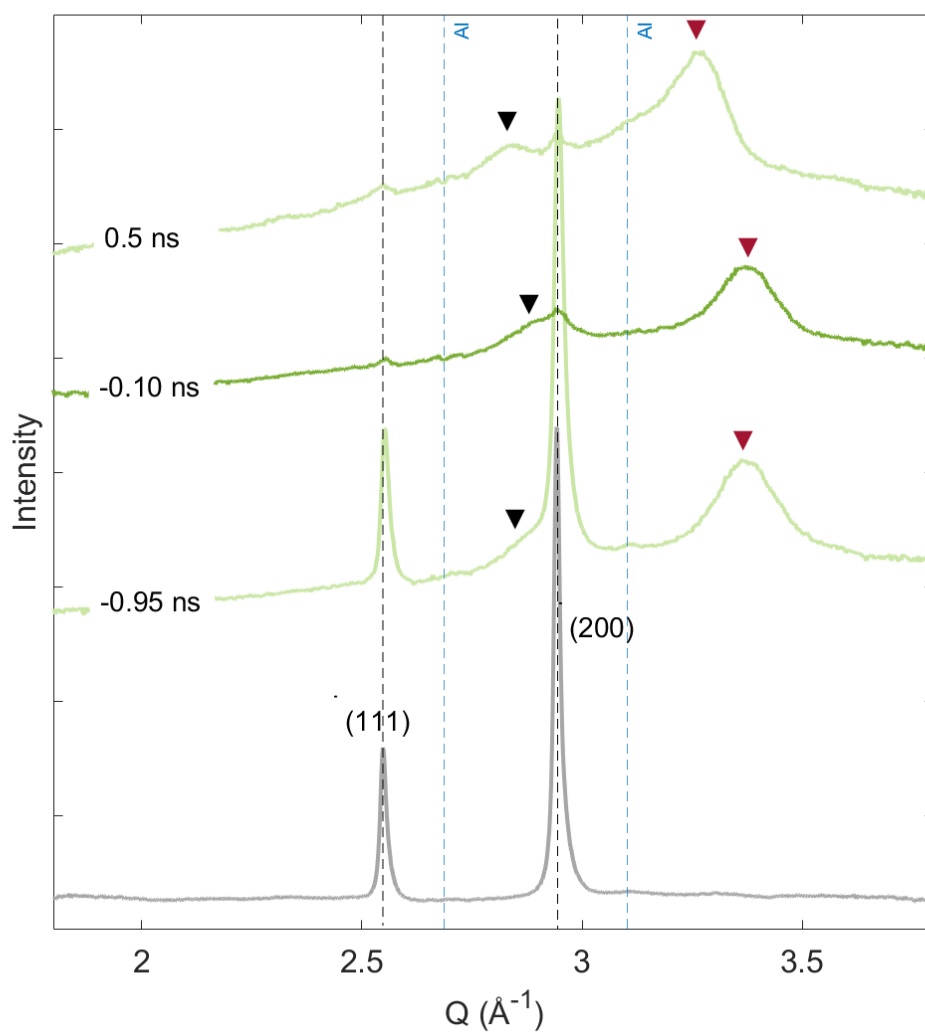


Figure 5.15: Integrated XRD lineouts of $(\text{Mg}_{0.4}, \text{Fe}_{0.6})\text{O}$ under shock compression at a laser intensity of $1.16 \times 10^{13} \text{ W/cm}^2$ collected by Quad 0 detector. $(\text{Mg}_{0.4}, \text{Fe}_{0.6})\text{O}$ at ambient includes reflections from (111) and (200) planes shown as black dash lines. The compressed (111) and (200) peaks are labeled as black and red reverted triangles, respectively. Al peaks from a sample frame are at blue dash line positions.

observed up to the maximum laser intensity at 1.2×10^{13} W/cm². In addition, the larger diffuse background was collected at the maximum laser intensity compared to the lower ones, but there was no other clear evidence of melting. At $t = 1.6$ ns of this intensity, the broad feature composing of at least two peaks was also observed but was less clear than for (Mg_{0.9}, Fe_{0.1})O. The 2D XRD from Quad 0 is depicted as Figure 5.17.

The volume and density of (Mg, Fe)O at the shock breakout time were obtained by performing a *Le Bail* refinement in the GSAS-II software package [73] and peak fitting using the origin software. Parameters from the refinement and the peak fitting can be found in Tables A.5 and A.6. Volume and density plots as a function of laser intensity are shown in Figure 5.18. The results show the consistency of volume and density with laser intensity: an increase in laser intensity led to a smaller volume or a denser (Mg,Fe)O. The volume or density trends were also similar for all the compositions of (Mg,Fe)O.

Pressure determination of slurry (Mg,Fe)O

Apart from XRD, VISAR measurements were also performed to derive pressure evolution in slurry (Mg,Fe)O during shock compression. Figure 5.20 shows the relation between laser intensity and average shock velocity in black Kapton and slurry (Mg,Fe)O. The results show that most of the average velocities are consistent except for two data points. These were collected from targets that were glued to sapphire windows. Thus, the unusual low velocity, i.e. the later shock breakout time, could be caused by a thick glue layer. U_s of the slurry used for pressure calculation cannot directly be obtained from the breakout time. Additional information such as U_s in black Kapton or shock breakout time from black Kapton as a function of laser intensity is needed.

Shock compression shots on black Kapton targets were not performed in this experiment. However, the BK/epoxy targets shot with the laser intensity of 8.41×10^{12} to 1.18×10^{13} W/cm² was instead measured by VISAR. The shock breakout times from black Kapton was recorded since an epoxy layer was transparent as shown in Figure 5.19. VISAR images show a dramatic reflectivity-change when a shock wave enters from black Kapton to an epoxy layer. The corresponding shock breakout times from black Kapton at these laser intensities are shown as Figure 5.21. In addition, hydrodynamic simulation of the black Kapton targets using the measured laser profile from the experiment were performed and are plotted as a comparison. The shifts of approximately 0.6 to 0.8 ns between the results from VISAR and hydrodynamic simulation are observed in Figure 5.21. As discussed in section 4.3, the calculated shock breakout time from FeO in the BK/FeO

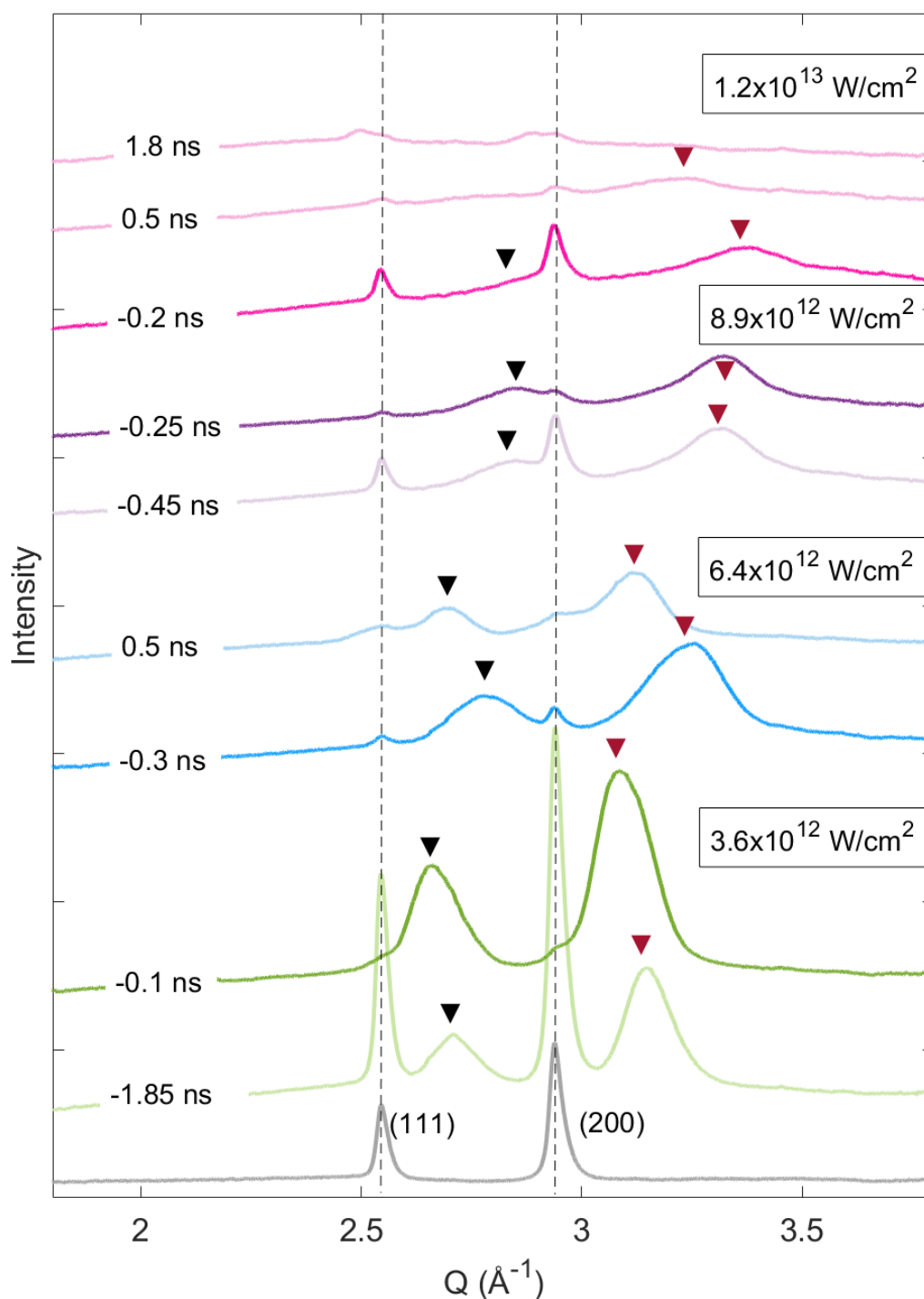


Figure 5.16: Integrated XRD lineouts of $(\text{Mg}_{0.2}, \text{Fe}_{0.8})\text{O}$ under shock compression at various laser intensities collected by Quad 0 detector. $(\text{Mg}_{0.2}, \text{Fe}_{0.8})\text{O}$ at ambient includes reflections from (111) and (200) planes shown as black dash lines. The compressed (111) and (200) peaks are labeled as black and red reverted triangles, respectively.

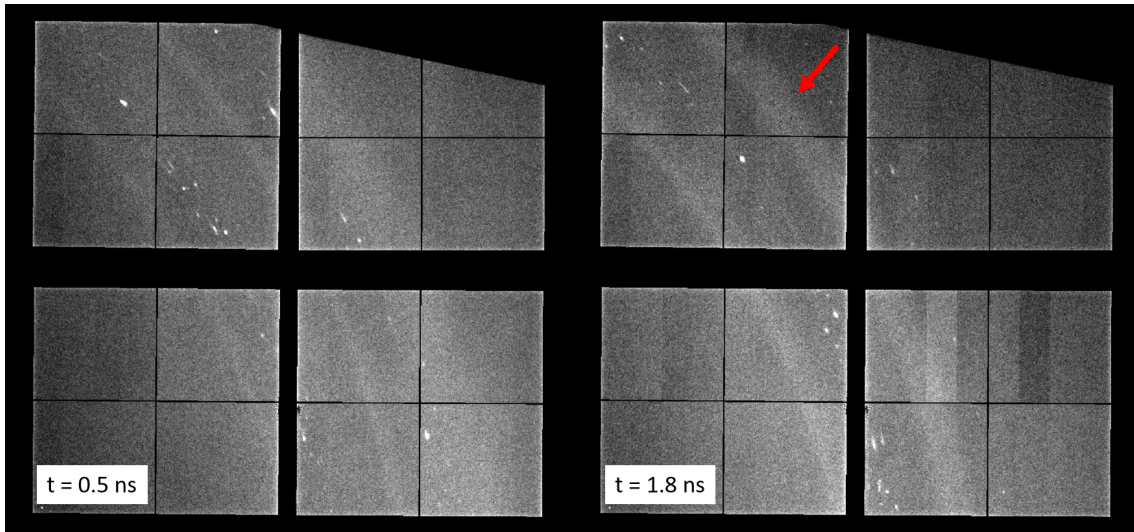


Figure 5.17: 2D XRD images of the shots with a laser intensity of $1.16 \times 10^{13} \text{ W/cm}^2$ at 0.5 and 1.8 ns after the shock breakout time.

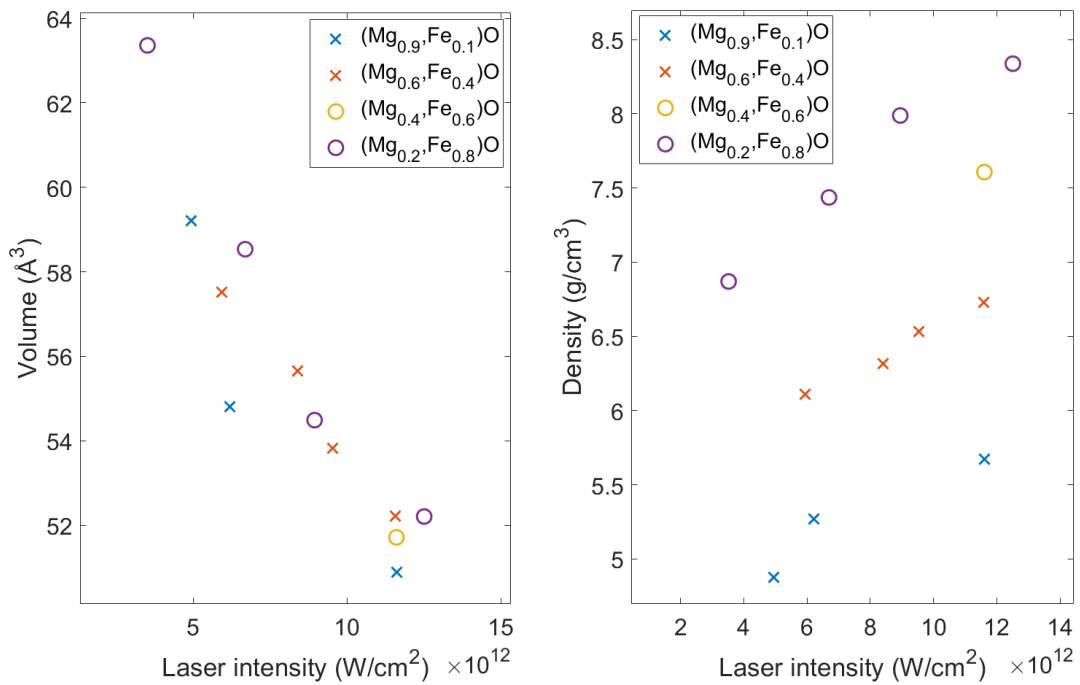


Figure 5.18: Volume and density of $(\text{Mg}_{0.9}, \text{Fe}_{0.1})\text{O}$, $(\text{Mg}_{0.6}, \text{Fe}_{0.4})\text{O}$, $(\text{Mg}_{0.4}, \text{Fe}_{0.6})\text{O}$, and $(\text{Mg}_{0.2}, \text{Fe}_{0.8})\text{O}$ under shock compression as a function of laser intensity.

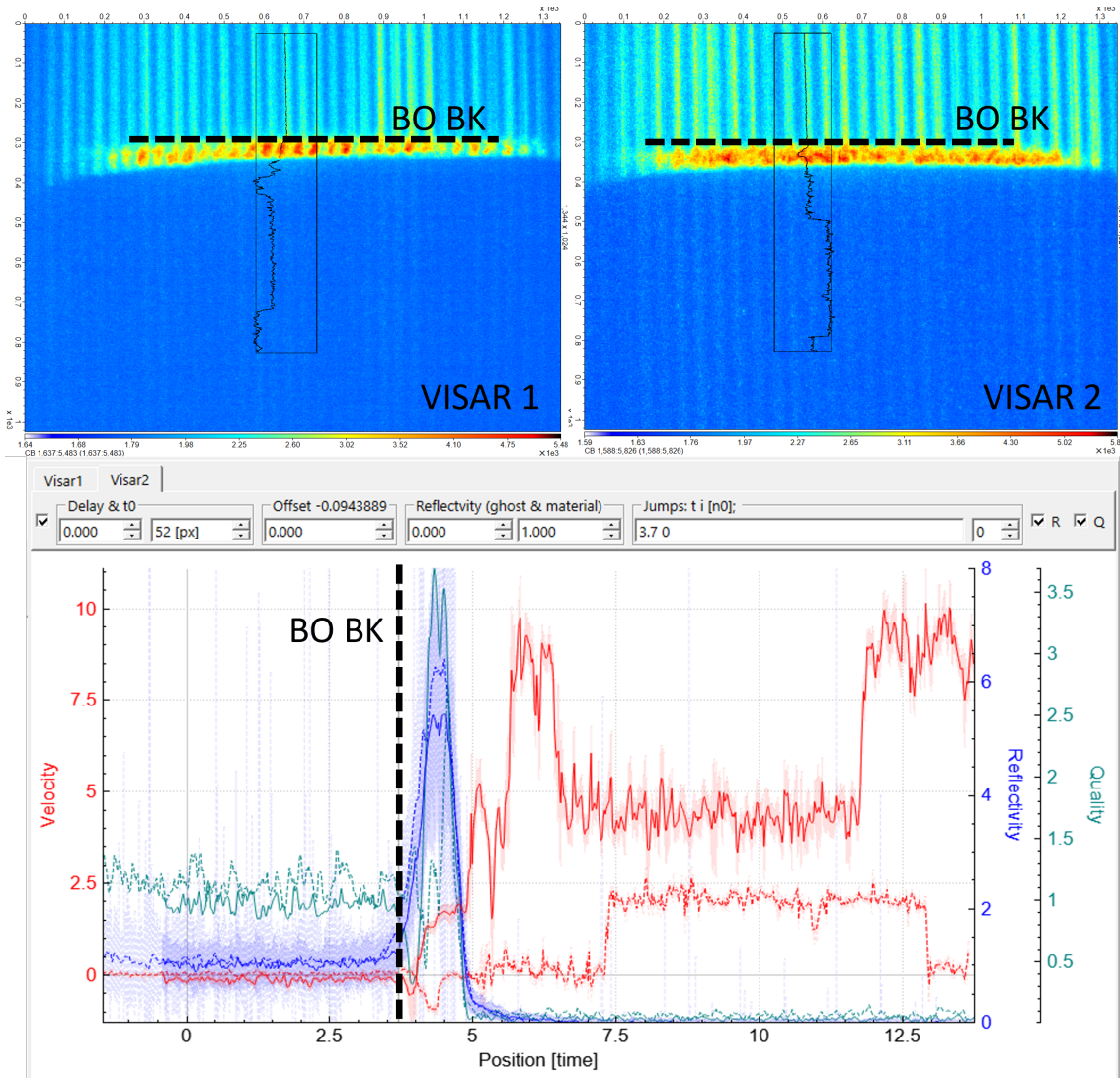


Figure 5.19: Example VISAR1 and VISAR2 images from run 401 of the BK/epoxy target and the extracted velocity, reflectivity, and quality profile from Neutrino software. The black dash line is referred to as the shock breakout time from black Kapton.

targets shown as Figure 4.12 is approximately 0.1 to 0.4 ns later than the one obtained from VISAR. The delays were mainly caused by the t_0 shift, which is estimated at at least ± 0.3 ns compared to the t_0 measured at the beginning of the experiment. Apart from shot-to-shot fluctuation of t_0 during the day, the additional shifts of 0.2 to 0.4 ns observed in Figure 5.21 could originate from other sources. For instance, the effective laser intensity on the day of the experiment for slurry (Mg,Fe)O was different from the day of the experiment for FeO such as intensity distribution of the driven laser. In this case, the relation $I_{\text{numerical}} = 0.45I_{\text{experiment}}$ have to be adjusted to higher than 0.45 to obtain the similar breakout time to the data from VISAR. However, the actual causes cannot be completely concluded from the available data. The shifts of 0.7 ± 0.1 ns was used for modification of the breakout time obtained from hydrodynamic simulation to the data on the day of the experiment at the laser intensity range of 4.0×10^{12} to 1.2×10^{13} W/cm², where the relation between laser intensity and shock breakout time from black Kapton is approximately linear. The time difference between shock breakout time from black Kapton and from slurry at the same laser profile was considered to be the shock transit time in a slurry layer. U_s in slurry can be calculated based on the estimated transit time in slurry and the corresponding slurry thickness. Figure 5.22 shows the approximated U_s in slurry (Mg,Fe)O for all the compositions as a function of a density from XRD probed at a shock breakout time from slurry. The results show very large U_s range with no clear relation between U_s and XRD density. The large error bars are caused by uncertainty of t_0 . The scattered data could also originate from the inhomogeneity of the slurry thickness. This suggests that the pressure of slurry cannot be accurately obtained from this method.

The calculations of the pressure of the slurry (Mg, Fe)O in this experiment were performed by two methods. The first method is based on impedance matching at a black Kapton-slurry interface. This method uses pressure in black Kapton at the interface calculated just before a shock wave enters the slurry from hydrodynamic simulation by using the laser pulse extracted from the experiment with modification of $I_{\text{numerical}} = 0.45I_{\text{experiment}}$. To perform impedance matching, the Hugoniot of black Kapton and the slurry (Mg, Fe)O are required. The Hugoniot of polyimide with a density of 1.415 g/cm³ [83] and the Hugoniot of the slurry (Mg_{0.9}, Fe_{0.1}) O obtained as equation 5.13 were used in this study. The U_s - U_p relation of (Mg_{0.9}, Fe_{0.1}) O was also used for (Mg_{0.6}, Fe_{0.4}) O by assuming a small difference between them. The impedance matching is similar to that performed in Figure 5.8. Here, the Hugoniot of black Kapton and slurry (Mg,Fe)O were used instead of the Hugoniot of quartz and Rayleigh line, respectively. The second method was

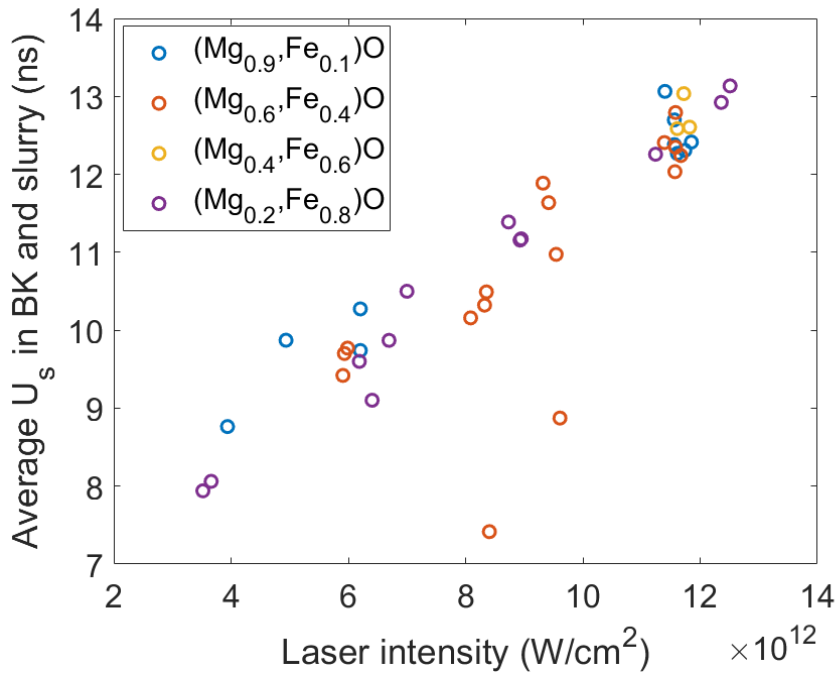


Figure 5.20: Average shock velocity propagating through black Kapton and slurry (Mg,Fe)O as a function of laser intensity.

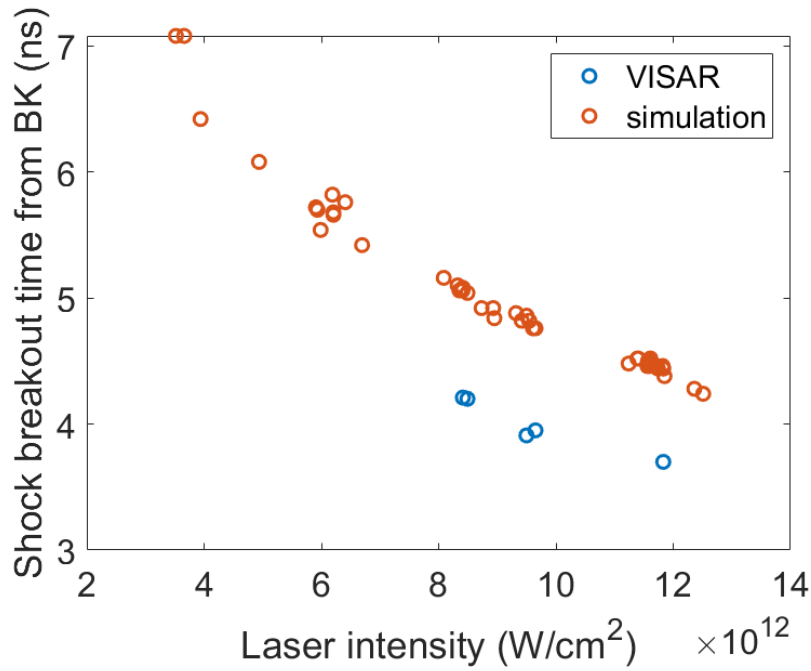


Figure 5.21: Shock breakout time from black Kapton as a function of laser intensity provided by VISAR measurement and hydrodynamic simulation.

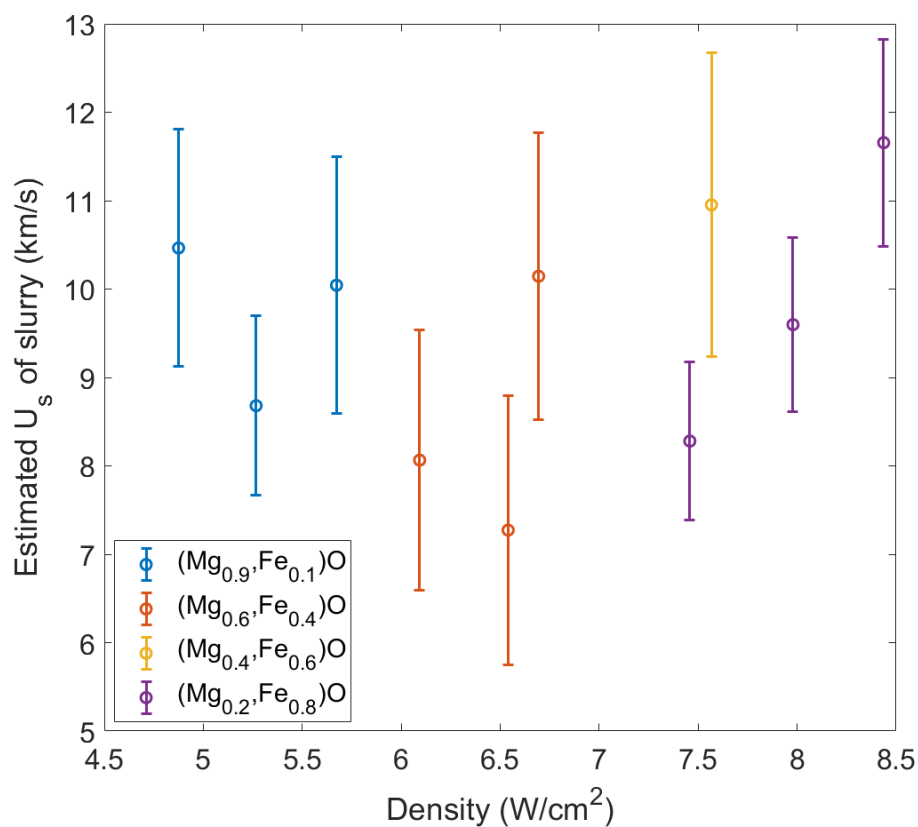


Figure 5.22: U_s in slurry (Mg,Fe)O as a function of XRD density estimated from shock breakout time of black Kapton, which was calculated by hydrodynamic simulation with the adjustment of 0.6 to 0.8 ns.

done by impedance matching at a slurry-window interface. In this experiment, some shots were made on the BK/slurry ($\text{Mg}_{0.6}, \text{Fe}_{0.4}$) O targets glued to quartz or sapphire windows. U_s and U_p information from the windows can be used for impedance matching to calculate pressure in a sample as described in Section 4.2. Instead of the FeO Hugoniot, the Hugoniot of slurry ($\text{Mg}_{0.9}, \text{Fe}_{0.1}$) O obtained from equation 5.13 was used for the slurry ($\text{Mg}_{0.6}, \text{Fe}_{0.4}$) O. The calculated pressures of slurry (Mg,Fe)O are labeled in Figures 5.12 and 5.14. The details are also attached as Tables A.7 and A.8 in the Appendix A.

Figure 5.23 shows the relation between the density of ($\text{Mg}_{0.9}, \text{Fe}_{0.1}$) O and ($\text{Mg}_{0.6}, \text{Fe}_{0.4}$) O and the pressure, which was obtained from impedance matching with the pressure in black Kapton compared to impedance matching with U_s or U_p of a quartz or sapphire window. The input density was obtained from XRD of the shots measured before or at shock breakout time. The pressures from impedance matching with windows and the XRD densities were not obtained from the same shots, but both parameters were obtained from shots with similar laser intensities. The results of Figure 5.23 show that the maximum pressure of approximately 180 GPa was reached for both compositions at maximum densities of ($\text{Mg}_{0.9}, \text{Fe}_{0.1}$) O and ($\text{Mg}_{0.6}, \text{Fe}_{0.4}$) O are 5.67 and 6.69 g/cm³, respectively. The pressures obtained from impedance matching of the slurry ($\text{Mg}_{0.6}, \text{Fe}_{0.4}$) O and windows are lower compared to those obtained from the impedance matching with black Kapton at the same density. The differences were considered due to the thick glue layer between slurry and window. This causes an inaccurate pressure calculated from impedance matching, where a glue layer cannot be taken into account. The thick glue layers resulted in later shock breakout times compared to target without windows shot with the same laser intensity. However, as the delay in break out time of 0.3 ns is still in the uncertainty range of t_0 shifts, the thickness of the glue layer is difficult to define. Another consequence from a thick glue layers could be observed from XRD: the XRD probed before or at the shock breakout time, which was obtained from VISAR, shows a release state instead of a fully compressed state. For example, the XRD peak, which is labeled as a red reverted triangle, probed at -0.1 ns with a laser intensity of 5.9×10^{12} W/cm² of Figure 5.14 shows a smaller Q or 2θ compared to the same peak probed at -0.5 ns. Therefore, in this case, the XRD could be measured when a shock wave was already released from a slurry and was in a glue layer. Since the XRD was similar to the measurement obtained from the target without window at 0.65 ns. The shock breakout time obtained from VISAR, which was defined from a sudden change of velocity or reflectivity in a window, was consequently not accurate with an error of approximately 0.7 ns: this time corresponds to approximately

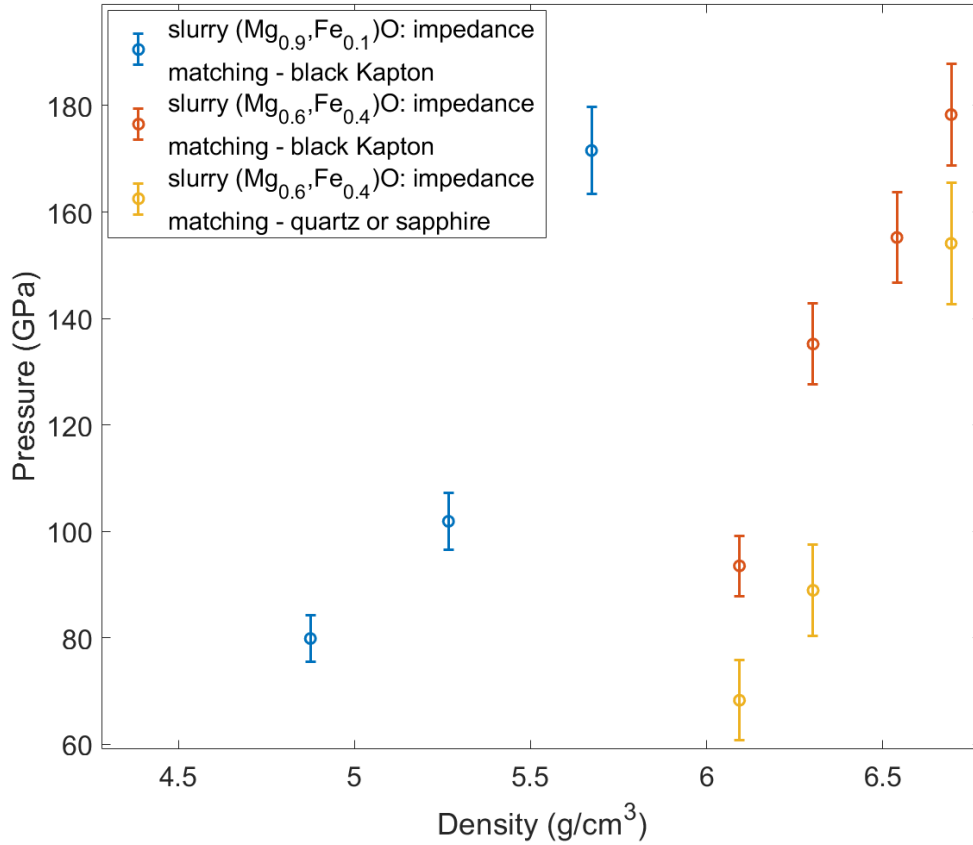


Figure 5.23: Pressure- U_p relation of slurry (Mg_{0.9}, Fe_{0.1}) O and slurry (Mg_{0.6}, Fe_{0.4}) O. Pressures are calculated from impedance matching with pressure in black Kapton and with U_s or U_p of a quartz or a sapphire window. Density of (Mg_{0.9}, Fe_{0.1}) O and (Mg_{0.6}, Fe_{0.4}) O are obtained from XRD probed at the shock breakout time from a slurry layer.

6 to 7 μm calculated from the average shock velocity. However, this estimation assumes a stable laser power and distribution for all the shots with similar laser intensity, which might not actually be correct for all cases.

5.3 Discussion

This chapter presents the Hugoniot relations of slurry (Mg_{0.9}, Fe_{0.1}) O and slurry (Mg_{0.6}, Fe_{0.4}) O up to a pressure of 280 GPa measured from the experiment at the LULI2000 facility. As shown in Figure 5.9, U_s - U_p plot of slurry (Mg_{0.9}, Fe_{0.1}) O shows a linear relationship up to U_p of 5.9 km/s, which corresponds to a pressure of 240 GPa. At higher pressure, U_s become smaller: the two shots with the maximum laser intensity at $4 \times 10^{13} \text{ W/cm}^2$ show similar U_s at approximately 12 km/s. Similar results were also observed in the slurry (Mg_{0.6}, Fe_{0.4}) O. However, due to insufficient data of (Mg_{0.6}, Fe_{0.4}) O

at lower intensities, the unusual drop of U_s compared to the trend of the data cannot be concluded. One of the possible reasons for describing the change in the U_s trend in the slurry ($\text{Mg}_{0.9}, \text{Fe}_{0.1}$) O is a phase transition. In chapter 4, the results show that the B1-liquid phase transition of FeO along its Hugoniot occurs at a pressure of 172 to 189 GPa. Previous shock compression studies of MgO show the B1-B2 phase transition at a pressure of 397 to 425 GPa and 9700K [15]. The boundary of B2 liquid was found to be above 600 GPa [14][15]. For (Mg, Fe)O, there have been no experimental studies on the B1-B2 phase transition and the B1-liquid or B2-liquid phase transition of (Mg,Fe)O along its Hugoniot until now. The B1-B2 phase transition of ($\text{Mg}_{0.9}, \text{Fe}_{0.1}$) O from *ab initio* calculation was at approximately 460 GPa and 7000K and the B1-B2 phase transition occurs at lower pressure when increasing temperature [94]. In addition, higher Mg content in ($\text{Mg}_{1-x}, \text{Fe}_x$) O, where x ranges from 0 to 0.12, leads to a higher pressure at the B1-B2 phase transition [94]. Another work on ($\text{Mg}_{1-x}, \text{Fe}_x$) O, where x ranges from 0.007 to 0.015, suggested that the B1-B2 phase transition occurs at approximately 380 to 390 GPa for the whole range of compositions in this study and the pressure-temperature range of the B1-B2 coexisting phase becomes larger with increasing Mg contents [95]. To confirm the phase transition, an XRD measurement at this pressure is needed. Furthermore, the U_s - U_p relation of the slurry ($\text{Mg}_{0.9}, \text{Fe}_{0.1}$) O from the shots at a pressure of higher than 300 GPa is required to justify this phase transition.

Figure 5.24 compares U_s - U_p relation of slurry ($\text{Mg}_{0.9}, \text{Fe}_{0.1}$) O and slurry ($\text{Mg}_{0.6}, \text{Fe}_{0.4}$) O from this study to the previous studies of shock compression on polycrystalline ($\text{Mg}_{0.94}, \text{Fe}_{0.06}$) O [39] and ($\text{Mg}_{0.6}, \text{Fe}_{0.4}$) O [31]. The results show the consistency between the data points from slurry ($\text{Mg}_{0.9}, \text{Fe}_{0.1}$) O of this study and polycrystalline ($\text{Mg}_{0.6}, \text{Fe}_{0.4}$) O of the previous study [31] up to U_p of approximately 4.2 km/s. These slurry data also follow the trend of ($\text{Mg}_{0.6}, \text{Fe}_{0.4}$) O from [31], which is shown as a blue dash line, until U_p of 5.5 km/s. In contrast, the data at the maximum U_s of 14.6 km/s from this study do not follow this trend, so the U_s - U_p linear relation of slurry ($\text{Mg}_{0.9}, \text{Fe}_{0.1}$) O up to this point, which is shown as a purple dash line, is different from the previous study [31]. In addition, the U_s - U_p relation of the slurry shows disagreement to the trend of polycrystalline ($\text{Mg}_{0.94}, \text{Fe}_{0.06}$) O [39], which is shown as a green dash line. The similarity or the difference between the data cannot be justified since there are no low pressure U_s - U_p from this study to compare.

The Hugoniot pressure- U_p relations of slurry ($\text{Mg}_{0.9}, \text{Fe}_{0.1}$) O and slurry ($\text{Mg}_{0.6}, \text{Fe}_{0.4}$) O are also compared to the calculated Hugoniot of slurry ($\text{Mg}_{0.94}, \text{Fe}_{0.06}$) O

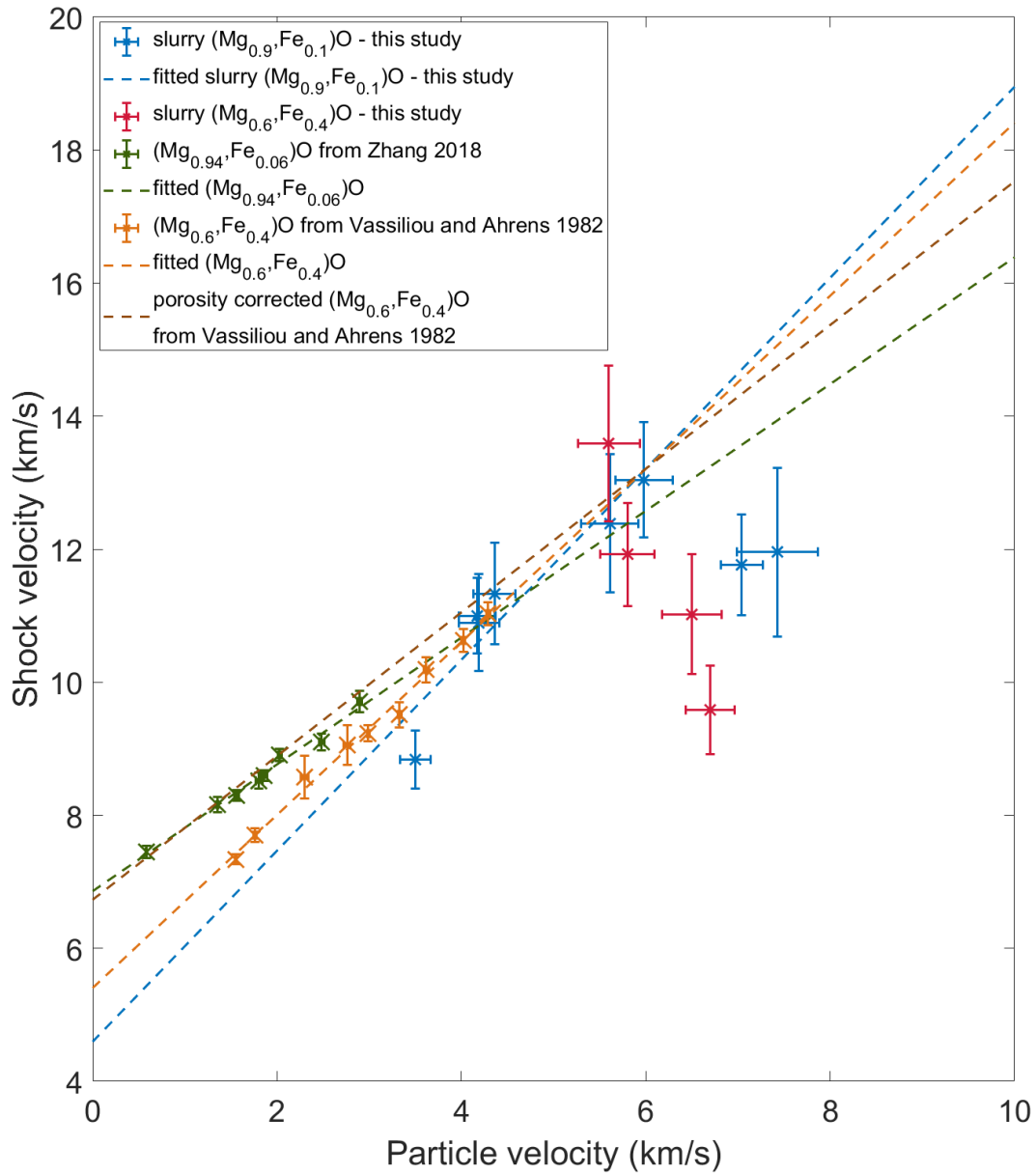


Figure 5.24: U_s - U_p relation of slurry ($\text{Mg}_{0.9}, \text{Fe}_{0.1}$)O and slurry ($\text{Mg}_{0.6}, \text{Fe}_{0.4}$)O from this study compared to the previous studies on polycrystalline (Mg,Fe)O [31][39].

and $(\text{Mg}_{0.6}, \text{Fe}_{0.4})\text{O}$ as shown in Figure. These were calculated from Hugoniot of epoxy [84], and $(\text{Mg}_{0.94}, \text{Fe}_{0.06})\text{O}$ [39] or $(\text{Mg}_{0.6}, \text{Fe}_{0.4})\text{O}$ [31] based on a velocity-based mixing rule. It is assumed that the mixture is at equilibrium pressure and U_p of the mixture is a weighted average of U_p of each individual component [54] [96]. The results show that both the Hugoniot of slurry $(\text{Mg}, \text{Fe})\text{O}$ from this study do not agree with the calculated slurry Hugoniot, where the pressures of $(\text{Mg}_{0.9}, \text{Fe}_{0.1})\text{O}$ from this study at the same U_p are higher compared to the calculated slurry Hugoniot. The pressure at the same U_p is lower compared to the Hugoniot of $(\text{Mg}, \text{Fe})\text{O}$ from polycrystalline samples, which is consistent with the lower density of the slurry samples. The results indicate that the slurry states under shock compression are complicated and might not be described by the velocity-based mixing rules. Although the literature [54] showed the consistency of the Hugoniot pressure-density relations between the slurry and pure materials, where the slurry pressures were calculated from the Hugoniot based on this velocity-based mixing rule, the data are only up to 100 GPa. The slurry behavior under shock compression at higher pressure could be different. The other possible reason could be the Hugoniot of epoxy used for the calculation: data from the literature [84] are available up to approximately 80 GPa. An extrapolation of these data to a higher pressure of 300 GPa used for the calculated Hugoniot of slurry could be inaccurate.

The relations between pressure and XRD density of $(\text{Mg}_{0.9}, \text{Fe}_{0.1})\text{O}$ and $(\text{Mg}_{0.6}, \text{Fe}_{0.4})\text{O}$ from the shock compression experiment of slurry $(\text{Mg}_{0.9}, \text{Fe}_{0.1})\text{O}$ and slurry $(\text{Mg}_{0.6}, \text{Fe}_{0.4})\text{O}$ at the MEC of LCLS and the LULI2000 facility are plotted as Figure 5.26 and $(\text{Mg}_{0.6}, \text{Fe}_{0.4})\text{O}$, respectively. The results are compared to previous shock compression of polycrystalline $(\text{Mg}_{0.94}, \text{Fe}_{0.06})\text{O}$ [39] or $(\text{Mg}_{0.6}, \text{Fe}_{0.4})\text{O}$ [31]. The densities from the literature [39] were not directly provided and were calculated from U_s , U_p , and the initial density of 3.753 g/cm^3 . The results of slurry $(\text{Mg}_{0.9}, \text{Fe}_{0.1})\text{O}$ from both experiments are consistent with the results from the literature, except the data at a pressure of 26 GPa. At this point, the pressure from this study is approximately 15 GPa lower than the polycrystalline one. The results of slurry $(\text{Mg}_{0.6}, \text{Fe}_{0.4})\text{O}$ from impedance matching with black Kapton also show consistency compared to the result of polycrystalline $(\text{Mg}_{0.6}, \text{Fe}_{0.4})\text{O}$ from the literature [31]. The results from impedance matching with windows show lower pressure at the same density: the possible reason is already described in Section 5.2. The discrepancy at low pressure, such as in slurry $(\text{Mg}_{0.9}, \text{Fe}_{0.1})\text{O}$ is not observed for slurry $(\text{Mg}_{0.6}, \text{Fe}_{0.4})\text{O}$. Thus, this discrepancy of one data point cannot be concluded whether it was caused by technical problems from the experiment or other

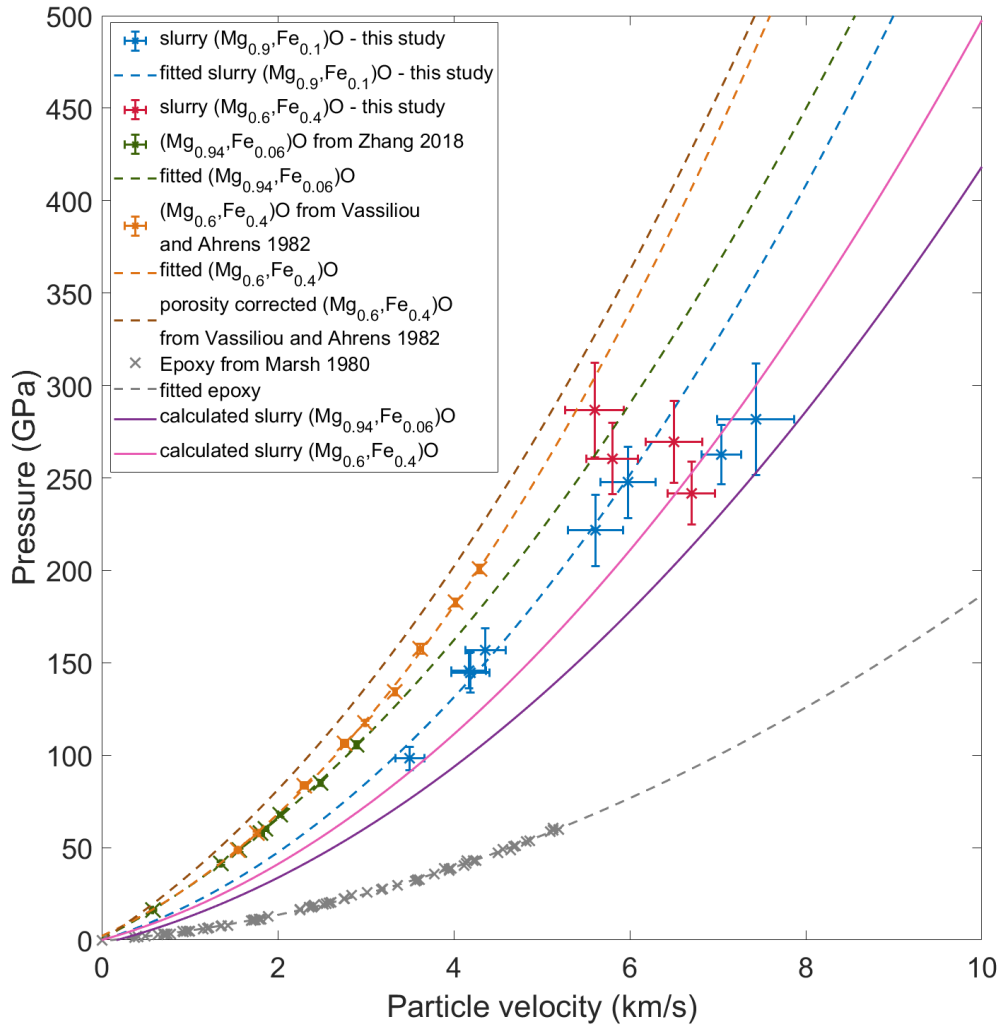


Figure 5.25: $P-U_p$ relation of slurry (Mg_{0.9}, Fe_{0.1})O and slurry (Mg_{0.6}, Fe_{0.4})O from this study compared to the previous studies on polycrystalline (Mg,Fe)O [31][39] and the calculated Hugoniot of slurry.

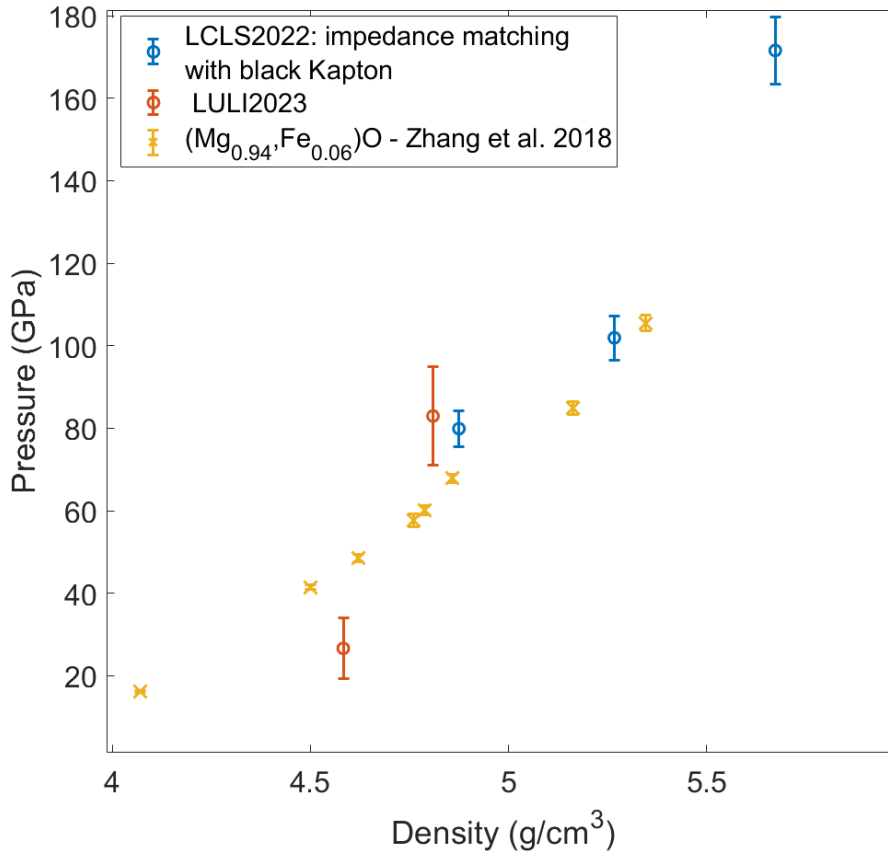


Figure 5.26: Pressure-density relation from this study of shock-compression on slurry $(\text{Mg}_{0.9}, \text{Fe}_{0.1})\text{O}$ compared to the previous research of shock compression on polycrystalline $(\text{Mg}_{0.96}, \text{Fe}_{0.04})\text{O}$ [39]. The density from this study was obtained from XRD measurement.

sources. One possible reason to point out is the precision of the extrapolation to the low pressure of the U_s-U_p relation in equation 5.13. The U_s-U_p data of slurry $(\text{Mg}_{0.9}, \text{Fe}_{0.1})\text{O}$ matches well with this equation at a pressure of 140 to 250 GPa. The data at 100 GPa is not very well matched. Therefore, the calculated pressure of lower pressure than 100 GPa might not be very accurate. U_s-U_p data at lower pressures on $(\text{Mg}_{0.9}, \text{Fe}_{0.1})\text{O}$ are needed to draw a better conclusion.

The pressure-unit cell volume relation of $(\text{Mg}_{0.9}, \text{Fe}_{0.1})\text{O}$ from this shock compression experiment was compared to those from the previous DAC studies [36][97][98], as shown in Figure 5.26. The results show the larger volume from this study compared to the other studies at a temperature of 300 K. In addition, the result from this study is more comparable to the DAC study [98] at a temperature of 1600 to 1900 K. Similar results are observed in Figure 5.29. The results show that the unit cell volume of $(\text{Mg}_{0.6}, \text{Fe}_{0.4})\text{O}$ from this study are larger compared to those from the DAC studies [97][99] at the same pressure.

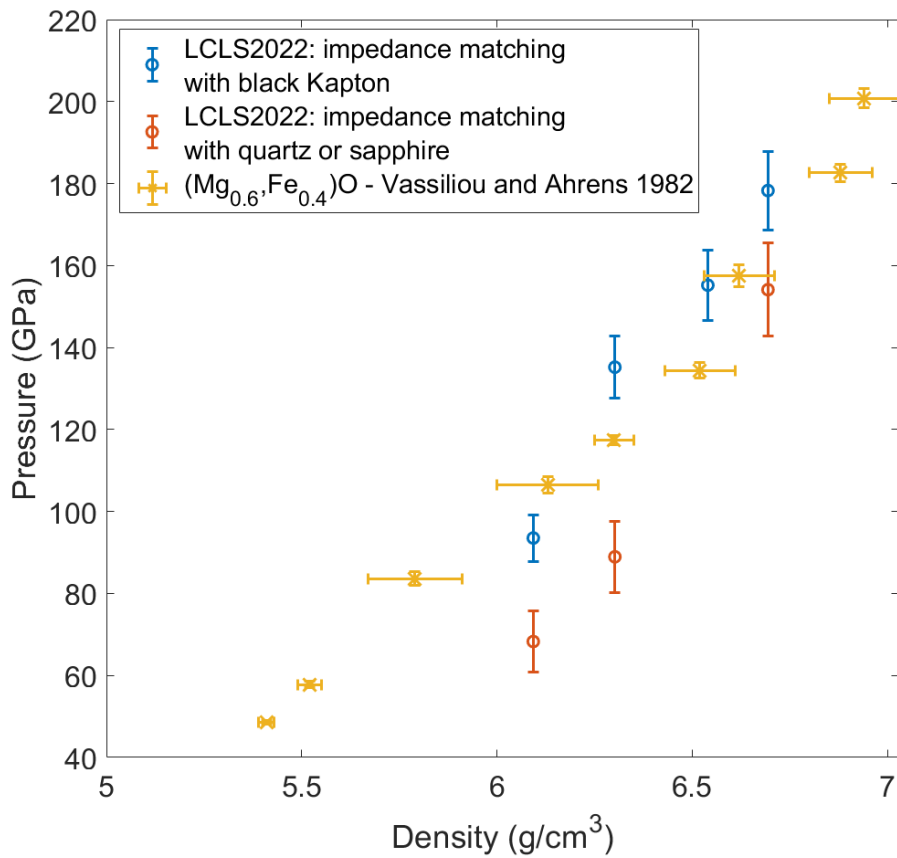


Figure 5.27: Pressure-density relation from this study of shock-compression on slurry (Mg_{0.6}, Fe_{0.4})O compared to the previous research of shock compression on polycrystalline (Mg_{0.6}, Fe_{0.4})O [31]. The density from this study was obtained from XRD measurement.

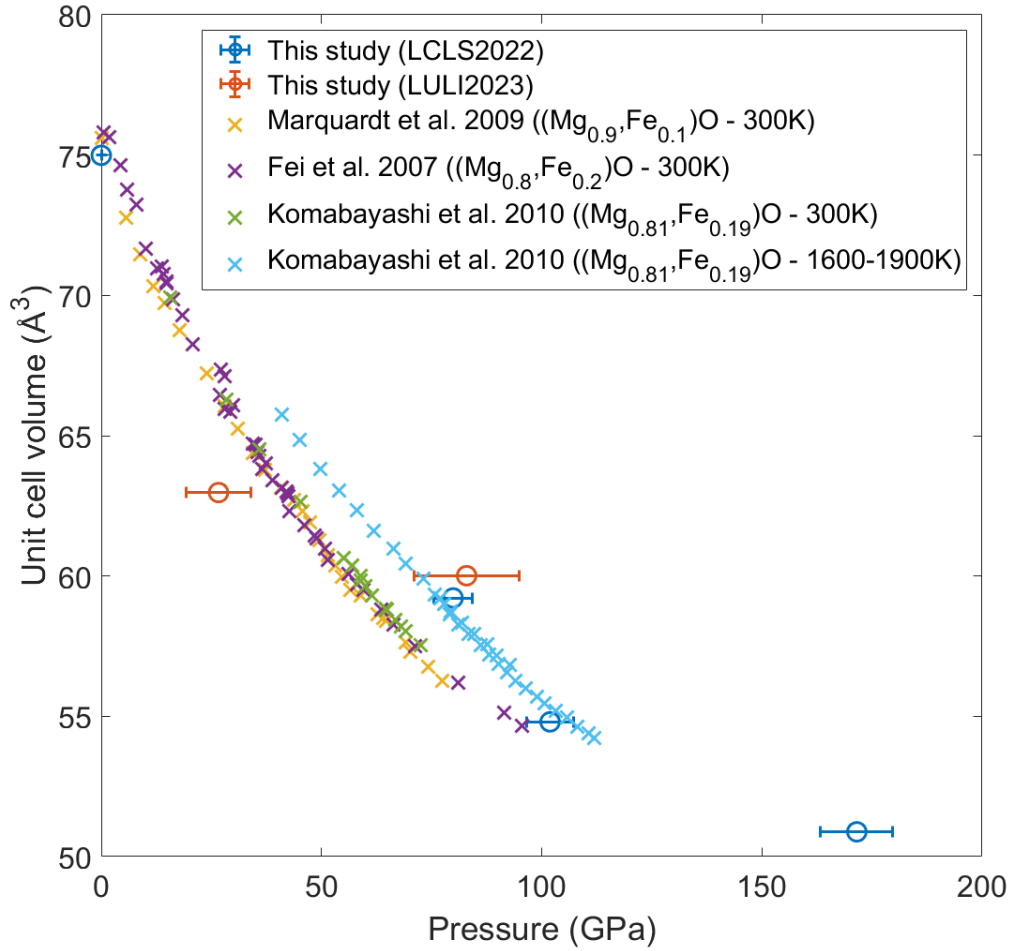


Figure 5.28: Pressure-unit cell volume relation from this study of shock compression on slurry $(\text{Mg}_{0.9}, \text{Fe}_{0.1})\text{O}$ compared to the previous DAC studies [36][97][98].

These expressed high temperature conditions of $(\text{Mg}_{0.9}, \text{Fe}_{0.1})\text{O}$ and $(\text{Mg}_{0.6}, \text{Fe}_{0.4})\text{O}$ under shock compression. However, one data point of $(\text{Mg}_{0.9}, \text{Fe}_{0.1})\text{O}$ at 26 GPa is not consistent, which is similar to what being observed in Figure 5.26. The possible explanation is discussed in the previous paragraph.

Apart from the XRD measurement at the shock breakout time i.e. at full compression, the $(\text{Mg}, \text{Fe})\text{O}$ structures during shock release were probed in the experiment at the LCLS. The data were collected at more than 1 ns after the shock breakout to observe whether $(\text{Mg}, \text{Fe})\text{O}$ returned to ambient states. Figure 5.12 and Figure 5.16 show very broad peaks of $(\text{Mg}, \text{Fe})\text{O}$ probed at 1.3 and 1.8 ns after the shock breakout. The broad peaks composed of at least two different pressure could originate from heterogeneity of pressure or/and temperature inside the materials. However, these are not observed in FeO probed at 0.9 or 2.6 ns after the shock breakout as shown in Figure 4.2. Another explanation could

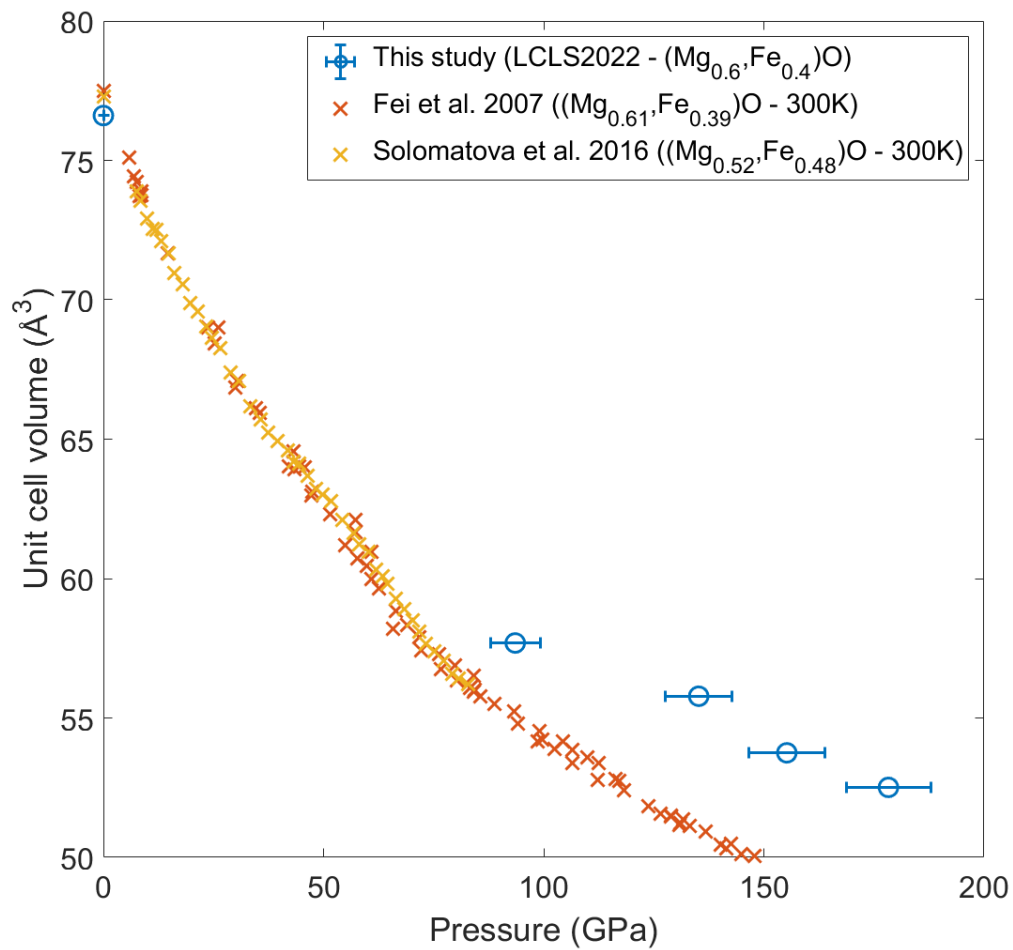


Figure 5.29: Pressure-unit cell volume relation from this study of shock compression on slurry (Mg_{0.6}, Fe_{0.4}) O compared to the previous DAC studies [97][99].

be that the broad peak could arise from the decomposition of (Mg,Fe)O. Previous studies observed the decomposition of (Mg, Fe)O into lighter and heavier phases after 5 to 6 hours of heating at a pressure of 86 GPa [28] and after the laser-heated DAC experiment [29]. This raises questions about the decomposition of (Mg,Fe)O in nanoseconds. Repeating of the experiment at the same pressure on (Mg, Fe)O is needed for further interpretation.

Chapter 6

Conclusion and Future Perspectives

6.1 Conclusion

This work investigates (Mg,Fe)O and FeO phase stability under shock compression at the pressure conditions relevant to those in planetary interiors. The results from the shock compression experiments performed at the MEC of the LCLS and the LULI2000 facilities are presented in Chapter 4 and 5. PVD and slurry FeO and (Mg,Fe)O samples were used as the main targets. These represent the different behaviors between pure material and powder-epoxy mixture under shock compression. In addition, four compositions of slurry (Mg,Fe)O ranging from (Mg_{0.9}, Fe_{0.1}) O to (Mg_{0.2}, Fe_{0.8}) O were chosen to observe the effects of Fe contents on the phase behaviors. The XRD measurement were made using femtosecond XFEL pulses and the time scans with nanosecond steps around the shock breakout were performed. The pressure conditions at fully shocked compression were determined from VISAR diagnostic and hydrodynamic simulation with MULTI code. In summary, the Hugoniot EoS of slurry (Mg,Fe)O were obtained. The (Mg,Fe)O and FeO structural phase transition along their Hugoniot from the both experiments are identified and compared to the previous researches.

FeO were compressed up to the maximum pressure of 250 GPa along its Hugoniot starting from B1 structure phase. Although PVD-FeO targets with Fe₂O₃ contamination were used, the high pressure XRD peak of Fe₂O₃ was not observed in any shock compression shots in this experiment. The FeO was found to be stable as B1 phase up to the pressure of 172 GPa and the liquid FeO was observed at the pressure greater than 189 GPa. Thus, the solid-liquid boundary of FeO along the Hugoniot was identified at 172 to 189 GPa in this study. This finding was approximately 10 GPa lower than those was calculated from the literature [22], where the intersection between the Hugoniot [26] and

the melting line of FeO [82] was estimated at approximately 200 GPa. The volumes of FeO under shock loading were obtained from the XRD measurement. The starting lattice parameter (a) and volume was 4.20 \AA and 74.34 \AA^3 , which are smaller than the powder FeO due to the residual stress during the deposition. The maximum compression was at 172 GPa when the lattice parameter and the volume of FeO were 3.67 \AA and 49.38 \AA^3 . The compressed volumes (V/V_0) at the corresponding pressure are compared and show the consistency to the previous study by DAC experiments [20][19] and shock compression experiment [26]. The volume of FeO at a pressure of 120 to 130 GPa was smaller than the trend at lower pressure. No structural phase transition was observed in the XRD, so the electronic transition such as the high spin to low spin transition could occur at this pressure range.

(Mg,Fe)O were shock-compressed up to the maximum pressure of 280 GPa. The first EoS measurement of the slurry targets was successfully done and the U_s - U_p Hugoniot relation of slurry ($\text{Mg}_{0.9}, \text{Fe}_{0.1}$) O was obtained up to the pressure of 240 GPa as $U_s = 1.4355U_p + 4.5962$. Due to the unavailability of the slurry ($\text{Mg}_{0.6}, \text{Fe}_{0.4}$) O data at low pressure, the U_s - U_p linear relation of slurry ($\text{Mg}_{0.9}, \text{Fe}_{0.1}$) O cannot be obtained from the experiment. The Hugoniot relation of slurry ($\text{Mg}_{0.9}, \text{Fe}_{0.1}$) O shows the disagreement to the Hugoniot calculated based on the velocity-based mixing rule taken from the literature [54]. These could originate from the invalidity of the calculated slurry Hugoniot using this method at a pressure greater than 100 GPa and the inaccuracy of the extrapolation of the epoxy Hugoniot when the pressure is more than 80 GPa. Moreover, the discontinuity of the Hugoniot P - U_p and U_s - U_p relations of slurry were observed at the pressure greater than 240 GPa. This is possibly interpreted as the B1-B2 phase transition of ($\text{Mg}_{0.9}, \text{Fe}_{0.1}$) O. The pressure at the B1-B2 phase boundary of ($\text{Mg}_{0.9}, \text{Fe}_{0.1}$) O was suggested by the *ab initio* calculation at approximately 460 GPa and 7000K and at lower pressure when increasing the temperature [94]. However, the temperature data along the Hugoniot from the experiment is missing, so the comparison cannot be completely concluded.

The XRD measurement of (Mg,Fe)O under shock loading was performed in the both experiments at the MEC of the LCLS and the LULI2000 facility. The phase structures were obtained up to a pressure of approximately 180 GPa, where the pressures were only determined for slurry ($\text{Mg}_{0.9}, \text{Fe}_{0.1}$) O and slurry ($\text{Mg}_{0.6}, \text{Fe}_{0.4}$) O. Up to the maximum pressure, only the B1 structure were observed along the Hugoniot for all the four compositions of (Mg,Fe)O. The differences of the structural phase stability due to the variation of Fe contents were not clearly observed up to this pressure and cannot be concluded from

the available data. The density of $(\text{Mg}_{0.9}, \text{Fe}_{0.1})\text{O}$ and $(\text{Mg}_{0.6}, \text{Fe}_{0.4})\text{O}$ at the corresponding pressure are consistent to the previous studies of shock compression on the polycrystalline $(\text{Mg}_{0.94}, \text{Fe}_{0.06})\text{O}$ [39] and $(\text{Mg}_{0.6}, \text{Fe}_{0.4})\text{O}$ [31] when the pressures are greater than 100 GPa. The pressure-unit cell volume of $(\text{Mg}_{0.9}, \text{Fe}_{0.1})\text{O}$ and $(\text{Mg}_{0.6}, \text{Fe}_{0.4})\text{O}$ were also compared to those from the previous DAC studies [36][97][98][99]. The results show the larger volumes at the same pressure that are caused by higher temperature in shock compression experiments. Apart from the XRD at fully compression, the XRD of $(\text{Mg}_{0.9}, \text{Fe}_{0.1})\text{O}$ and $(\text{Mg}_{0.2}, \text{Fe}_{0.8})\text{O}$ was measured at more than 1 ns after the shock breakout. The broad peak features consisting of at least two peaks were observed in both compositions, which were not observed in the shot on PVD FeO. These could be caused by inhomogeneity of temperature and pressure or dissociation of $(\text{Mg,Fe})\text{O}$ during the shock release.

6.2 Implication for geology and planetary science

$(\text{Mg,Fe})\text{O}$ is the second most abundant phase of the Earth's mantle [9][10][11] and is also considered as a major phase constituting interiors of super-Earths. Thus, the knowledge of phase stability and physical properties at extreme conditions of $(\text{Mg,Fe})\text{O}$ as well is crucially important for understanding and modeling the structure and formation of the Earth and super-Earths. This includes the knowledge of the solid-liquid boundary and solid-solid phase transitions such as the B1-B2 phase transition. FeO, an end-member of $(\text{Mg,Fe})\text{O}$, could be present near the CMB and be formed by interactions between the core and the mantle [81][100][101] or magma ocean crystallization [102]. The high spin to low spin transition of FeO is expected in the large pressure range between 90 to 150 GPa [24]. This spin cross over was reported to be coupled with 2.5 % volume decrease and smaller decrease in B8-phase of $\text{Fe}_{0.96}\text{O}$ at high temperature [80]. Thus, the spin transition of FeO could be observed in this study as a small volume collapse at a pressure of 120 to 130 GPa along the Hugoniot. The spin transition of FeO could influence the heat-flow variations in the base mantle and contribute to the seismic anomalies of the D'' region [81][103].

Apart from FeO, this study includes the investigation of the $(\text{Mg,Fe})\text{O}$ phase stability at high pressure-temperature conditions. The B1-B2 phase transition of $(\text{Mg,Fe})\text{O}$ could be observed at a pressure greater than 250 GPa. This condition does not occur within the Earth's mantle, where the core-mantle boundary (CMB) is at approximately 136 GPa and 4800K [104] and according to present models $(\text{Mg,Fe})\text{O}$ is not present in the mantle.

However, it could occur in super-Earths with deeper core-mantle boundaries. For example, the pressure at the CMB of the $5M_E$, where M_E is the Earth's mass, is expected at 600 GPa and could reach TPa in the larger super-Earths [8][105]. The studies reported a decrease in mantle viscosity across the B1- B2 phase transition in MgO at the super-Earth interior conditions [106][107]. The mantle viscosity strongly affects the rheological properties such as convection style and thermal evolution [22][107].

6.3 Future perspectives

In this study, shock compression studies of FeO showed its melting behavior along the Hugoniot curve. In addition, FeO under shock compression showed a volume decrease at pressures between 120 to 130 GPa. No phase transition was observed in this pressure region. The nature of the volume decrease could be studied in future experiments by spectroscopic studies to understand whether an electronic transition is observed at this pressure.

The shock compression experiments (Mg,Fe)O were conducted in this study and allowed the observation of the phase transition along the Hugoniot. The Hugoniot EoS of slurry ($Mg_{0.9}, Fe_{0.1}$) O was successfully obtained up to a pressure of 270 GPa. However, the data of slurry ($Mg_{0.6}, Fe_{0.4}$) O from the EoS experiment were available from the pressure of 250 GPa, where the discontinuity could already occur. Therefore, the U_s-U_p linear relation cannot be obtained for this composition and the differences compared to slurry ($Mg_{0.9}, Fe_{0.1}$) O cannot be justified. To fully understand and interpret the results of slurry ($Mg_{0.6}, Fe_{0.4}$) O, the U_s and U_p data at lower and higher pressure are required and future experiments are suggested. In addition, the data at a pressure greater than 280 GPa and XRD measurements at pressures where the discontinuity was observed are needed to confirm the B1-B2 phase transition of (Mg,Fe)O. The experiment at the same pressure conditions on the pure (Mg,Fe)O samples such as PVD and single crystals would be required to study the discontinuity in more detail. Apart from the observation along the Hugoniot conditions, the XRD measurement at 1 ns after shock break out i.e. on the release states of (Mg,Fe)O were also performed in this study. The results showed broad peak features that be either interpreted as an inhomogeneity of pressure or temperature in the material or a dissociation of (Mg,Fe)O. Repeating the experiment at the same pressure-temperature conditions would be required to further support the interpretation.

Appendix A

Parameters from XRD and VISAR analysis

Table A.1: Results from XRD peak fitting of PVD-FeO from the experiment at the MEC of LCLS.

Run	Laser Intensity (TW/cm ²)	2 θ of (200) (°)	error	a (Å)	Volume (Å ³)	V/V ₀	P (GPa)
306	0.00	26.2260	0.0005	4.2037	74.2836	1.0000	0.0000
169	2.24	20.7359	0.0022	4.0524	66.5466	0.8958	31.8300
159	3.53	22.1115	0.0025	3.8031	55.0069	0.7405	94.0900
157	4.60	22.3196	0.0010	3.7681	53.5013	0.7202	105.5700
301	5.60	29.9161	0.0032	3.6949	50.4442	0.6791	129.2800
88	6.10	22.7756	0.0019	3.6936	50.3916	0.6784	142.5900
151	6.55	22.5672	0.0015	3.7273	51.7820	0.6971	152.3780
177	6.79	22.7362	0.0018	3.6999	50.6504	0.6819	157.4080
173	6.99	22.7646	0.0028	3.6954	50.4636	0.6793	161.2430
175	7.03	22.7766	0.0032	3.6935	50.3851	0.6783	162.7800
137	7.38	22.8117	0.0041	3.6878	50.1556	0.6752	172.1560
141	7.61	22.9328	0.0057	3.6813	49.8886	0.6716	175.3030

Table A.2: Results from XRD peak fitting and refinement of slurry-FeO from the experiment at the MEC of LCLS.

Run	Laser Intensity (TW/cm ²)	Peak fitting		GSAS II			
		a (Å)	Volume (Å ³)	a (Å)	Volume (Å ³)	reduced- χ^2	R _w (%)
347	6.42	3.9376	61.0519	3.9253	60.4800	0.5400	6.1410
351	8.69	3.8998	59.3090	3.8852	58.6470	2.0400	5.9640

Table A.3: U_s , U_p and pressure of quartz and slurry $(\text{Mg}_{0.9}, \text{Fe}_{0.1})\text{O}$ and slurry $(\text{Mg}_{0.6}, \text{Fe}_{0.4})\text{O}$ obtained from the experiment at the LULI2000 facility

Run	Laser int. (TW/cm ²)	U_s quartz (km/s)	dU_s quartz (km/s)	U_s slurry (km/s)	dU_s slurry (km/s)	U_p slurry (km/s)	dU_p slurry (km/s)	P slurry (GPa)	dP slurry (GPa)
$(\text{Mg}_{0.9}, \text{Fe}_{0.1})\text{O}$									
14	13.4	8.33	0.15	8.84	0.44	3.50	0.16	98.33	6.28
20	13.5	9.65	0.18	11.00	0.57	4.17	0.20	145.64	9.45
7	15.6	9.96	0.18	11.33	0.77	4.36	0.23	156.73	11.84
8	16.1	9.65	0.18	10.90	0.73	4.19	0.22	144.76	10.87
41	23.2	11.85	0.22	12.39	1.04	5.61	0.31	221.56	19.34
30	29.9	12.43	0.25	13.04	0.87	5.98	0.31	247.68	19.31
18	38.4	13.51	0.13	11.76	0.76	7.04	0.23	262.60	16.09
12	40.3	14.01	0.27	11.96	1.27	7.43	0.44	281.81	30.24
$(\text{Mg}_{0.6}, \text{Fe}_{0.4})\text{O}$									
34	25.4	12.39	0.22	11.92	0.77	5.80	0.29	260.48	19.14
40	27.2	12.44	0.23	13.59	1.17	5.60	0.33	286.67	25.48
37	30.5	13.01	0.17	9.58	0.66	6.70	0.27	241.70	16.97
24	33.1	13.09	0.20	11.02	0.90	6.50	0.32	269.52	22.20

 Table A.4: Results from peak fitting and pressure of slurry $(\text{Mg}_{0.9}, \text{Fe}_{0.1})\text{O}$ and $(\text{Mg}_{0.6}, \text{Fe}_{0.4})\text{O}$ obtained from the experiment at the LULI2000 facility

Run	Laser intensity (TW/cm ²)	2θ of (200) (°)	error	a (Å)	Volume (Å ³)	Density (g/cm ³)	U_s (km/s)	Pressure (GPa)
$(\text{Mg}_{0.9}, \text{Fe}_{0.1})\text{O}$ (slurry density 3.174 g/cm ³)								
49	ambient	52.299	0.002	4.212	74.704	3.864		
49	4.12	55.619	0.012	3.978	62.973	4.583	6.46 ±0.38	26.62 ±7.31
14	ambient	52.197	0.004	4.219	75.108	3.843		
14	13.4	56.600	0.011	3.915	60.010	4.810	8.84 ±0.40	82.95 ±11.93
21	ambient	52.455	0.007	4.200	74.085	3.896		
21	14.3	58.232	0.034	3.815	55.506	5.200		
$(\text{Mg}_{0.6}, \text{Fe}_{0.4})\text{O}$ (slurry density 3.766 g/cm ³)								
56	ambient	51.722	0.009	4.257	77.143	4.556		
56	15.5	55.765	0.042	3.969	62.519	5.622		

Table A.5: Parameters from XRD refinement of (Mg,Fe)O from the experiment at the MEC of LCLS.

Run	Laser Intensity (TW/cm ²)	a (Å)	Volume (Å ³)	density (g/cm ³)	reduced- χ^2	R _w (%)
(Mg _{0.9} , Fe _{0.1})O						
404	0.00	4.2143	74.8470	3.8570	0.55	21.94
415	4.94	3.8978	59.2170	4.8750	6.76	14.79
411	6.21	3.7983	54.8000	5.2670	9.73	15.65
405	11.61	3.7056	50.8820	5.6730	1.16	6.16
(Mg _{0.6} , Fe _{0.4})O						
428	0.00	4.2474	76.6250	4.5870	0.86	12.23
437	5.93	3.8640	57.6890	6.0930	1.01	6.05
455	8.41	3.8208	55.7790	6.3020	1.95	11.19
445	9.54	3.7739	53.7490	6.5400	0.79	4.85
429	11.58	3.7447	52.5100	6.6940	0.84	4.61
(Mg _{0.4} , Fe _{0.6})O						
466	11.61	3.7323	51.9920	7.5670	0.24	3.36
(Mg _{0.2} , Fe _{0.8})O						
370	0.00	4.2605	77.3360	5.6290	0.60	13.71
391	3.52	3.9844	63.2530	6.8820	11.06	12.02
381	6.69	3.8791	58.3690	7.4580	1.47	4.76
379	8.95	3.7927	54.5550	7.9790	0.50	3.03
371	12.51	3.7228	51.5940	8.4370	0.20	1.53

Table A.6: Parameters from XRD peak fitting of (Mg,Fe)O from the experiment at the MEC of LCLS.

Run	Laser Intensity (TW/cm ²)	2 θ of (200) (°)	error	a (Å)	Volume (Å ³)	density (g/cm ³)
(Mg _{0.9} , Fe _{0.1})O						
404	0.00	26.1416	0.0004	4.2170	74.9924	3.8487
415	4.94	28.3507	0.0023	3.8944	59.0636	4.8866
411	6.21	29.0987	0.0028	3.7964	54.7151	5.2750
405	11.61	29.8268	0.0011	3.7057	50.8881	5.6717
(Mg _{0.6} , Fe _{0.4})O						
428	0.00	25.9478	0.0009	4.2480	76.6558	4.5849
437	5.93	28.6088	0.0023	3.8600	57.5116	6.1111
455	8.41	28.9300	0.0058	3.8180	55.6567	6.3148
445	9.54	29.2617	0.0015	3.7757	53.8253	6.5296
429	11.58	29.5639	0.0028	3.7379	52.2268	6.7295
(Mg _{0.4} , Fe _{0.6})O						
466	11.61	29.6635	0.0019	3.7257	51.7142	7.6063
(Mg _{0.2} , Fe _{0.8})O						
370	0.00	25.8606	0.0027	4.2621	77.4208	5.6218
391	3.52	27.6818	0.0021	3.9866	63.3588	6.8695
381	6.69	28.4376	0.0023	3.8827	58.5347	7.4357
379	8.95	29.1397	0.0028	3.7911	54.4893	7.9877
371	12.51	29.5675	0.0038	3.7375	52.2082	8.3367

 Table A.7: Pressure of slurry (Mg_{0.9}, Fe_{0.1})O and (Mg_{0.6}, Fe_{0.4})O obtained from impedance matching with pressure in black Kapton from hydrodynamic simulation.

Run	Laser Intensity (TW/cm ²)	P BK sim (interface) (GPa)	U_p slurry (km/s)	dU_p slurry (km/s)	P slurry (GPa)	dP slurry (GPa)
(Mg _{0.9} , Fe _{0.1})O						
415	4.937	48.13	2.8941	0.1061	79.88	4.3714
411	6.205	62.16	3.4058	0.116	101.9	5.3213
405	11.610	107.24	4.7591	0.1406	171.55	8.1897
(Mg _{0.6} , Fe _{0.4})O						
437	5.933	54.3	2.9825	0.1198	93.53	5.6436
455	8.406	79.89	3.8051	0.1373	135.2	7.6218
445	9.544	92.29	4.1585	0.1445	155.21	8.5456
429	11.580	106.655	4.5409	0.1522	178.29	9.5958

Table A.8: Pressure of slurry ($\text{Mg}_{0.6}, \text{Fe}_{0.4}$)O obtained from impedance matching with U_p or U_s in windows obtained from VISAR.

Run	Laser int. (TW/cm ²)	window	U_p/U_s window (km/s)	dU_p/dU_s window (GPa)	U_p slurry (km/s)	dU_p slurry (km/s)	P slurry (GPa)	dP slurry (GPa)
435	5.908	qtz (U_p)	2.865	0.195	2.403	0.182	68.280	7.547
451	8.086	sap (U_s)	11.034	0.172	2.883	0.186	88.940	8.641
449	8.324	sap (U_s)	11.071	0.179	2.923	0.193	90.077	9.018
453	8.355	sap (U_s)	11.034	0.172	2.883	0.186	88.940	8.641
431	11.57	sap (U_s)	12.220	0.185	4.140	0.192	154.110	11.381

Appendix B

Example of input for MULTI hydrodynamic simulation

Listing B.1: Example of MULTI input of a target with the configuration 49- μm PN/ 5- μm FeO/ 25- μm sapphire. The laser is obtained from the experiment with $I_{\text{numerical}} = 0.45I_{\text{experiment}}$ and the wavelength is 527 nm.

&RBOUND

```
TEMRAD = 0.0 , IEXT = 0 , LTR = 0 ,  
XTR = 0. ,  
ALPHAL = 0. , ALPHAR = 0. , BETAL = 0. ,  
BETAR = 0. ,  
GAB = 1. , GBA = 1. , GOB = 0 ,  
GOA = 0. ,
```

&END

&INPUT

```
IGEO = 1 , NSPLIT = 1 , NDIV = 1 ,  
VARNOM = .1 ,  
TEXIT = 20E-9 , DTN = 10.0E-12 ,  
NEXIT = 500000 ,  
TOUT(1:2) = 0.0E-15, 100.0E-9 ,
```

&END

&FILM

```
itime = 4 ,  
dtdisk = 20e-12  
&END
```

```
&NGMK
```

```
outmrp= F, NLHYD = T, NLRAD = T , NL2TMP = F,  
NLZMOR = F , NLPICH = F ,  
NLMAC = F, NLFUS = F, ncolli = 2 ,
```

```
&END
```

```
&LAYER
```

```
NC = 500 , THICK = 25e-4 , ZONPAR = 1.01 ,  
R0 = 1.12 , TE0 = 0.026 , TI0 = 0.026 ,  
v0 = 0.0 ,  
ATWGT = 6.51 , ATNUM0 = 5.7 , ZION = 5.7 ,  
zmin = 0.1 ,  
FIM = '~/Tables/Polystyrene/7591_3eos.multi.gz'  
FIP = '~/Tables/Polystyrene/C1H1_planck_mult_gr.lanl.gz'  
FIR = '~/Tables/Polystyrene/C1H1_rossld_grey.lanl.gz'  
FIZ = '~/Tables/Polystyrene/C1H1_zeff.lanl.gz'
```

```
&END
```

```
&LAYER
```

```
NC = 105 , THICK = 24e-4 , ZONPAR = 1.00 ,  
R0 = 1.12 , TE0 = 0.026 , TI0 = 0.026 ,  
v0 = 0.0 ,  
ATWGT = 6.51 , ATNUM0 = 5.7 , ZION = 5.7 ,  
zmin = 0.1 ,  
FIM = '~/Tables/Polystyrene/7591_3eos.multi.gz'  
FIP = '~/Tables/Polystyrene/C1H1_planck_mult_gr.lanl.gz'  
FIR = '~/Tables/Polystyrene/C1H1_rossld_grey.lanl.gz'  
FIZ = '~/Tables/Polystyrene/C1H1_zeff.lanl.gz'
```

```
&END
```

&LAYER

```

NC      = 105      , THICK  = 5e-4  , ZONPAR = 1.0 ,
R0      = 5.74     , TE0    = 0.026  , TI0    = 0.026 ,
v0      = 0.0     ,
ATWGT  = 71.844   , ATNUM0 = 23.81   , ZION    = 23.81 ,
zmin   = 0.1     ,
FIM     = '~/'Tables/FeO-22.multi.gz'
IMION   = 0
FIE     = '~/'Tables/Iron/Fe__NG.eps.gz'
FIP     = '~/'Tables/Iron/Fe__NG.opp.gz'
FIR     = '~/'Tables/Iron/Fe__NG.opr.gz'
FIZ     = '~/'Tables/Iron/Fe__NG.opz.gz'

```

&END

&LAYER

```

NC      = 95      , THICK  = 25e-4  , ZONPAR = 1.025 ,
R0      = 3.98     , TE0    = 0.026  , TI0    = 0.026  ,
v0      = 0.0     ,
ATWGT  = 101.96   , ATNUM0 = 11.14   ,
ZION    = 11.14   , zmin   = 0.1   ,
FIM     = '~/'Tables/Sapphire/7411.ieos.multi.gz'
IMION   = 0
FIE     = '~/'Tables/Sapphire/Sapphire.ope.gz'
FIP     = '~/'Tables/Sapphire/Sapphire.opp.gz'
FIR     = '~/'Tables/Sapphire/Sapphire.opr.gz'
FIZ     = '~/'Tables/Sapphire/Sapphire.opz.gz'

```

&END

&PULSE

```

INTER   = 0 ,
WL      = 527E-7 ,
FILEPULSE = 'run343_laser-sum.txt'
PIMAX   = 0.45 , ! numerical intensity ratio
PITIME  = -1e-9 , ! delay by 1 ns to get a laser at t<0

```

Tmax = 1E-9,
PINACH = 0

&END

&THERM

FFACTOR = 0.5 ,

&END

FINAL

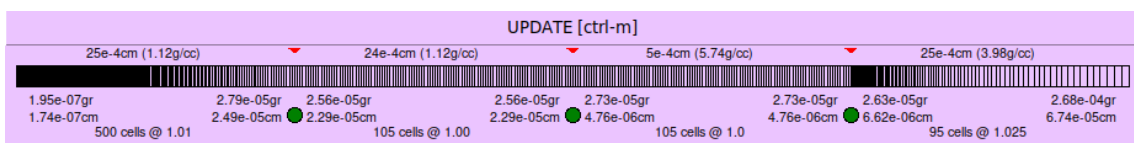


Figure B.1: The corresponding mesh tab of the MULTI simulation.

Bibliography

- [1] A. Wolszczan and D. A. Frail, “A planetary system around the millisecond pulsar psr1257 + 12,” *Nature*, vol. 355, p. 145–147, Jan 1992.
- [2] F. W. Wagner, N. Tosi, F. Sohl, H. Rauer, and T. Spohn, “Rocky super-earth interiors - structure and internal dynamics of corot-7b and kepler-10b,” *Astronomy & Astrophysics*, vol. 541, May 2012.
- [3] N. Madhusudhan, K. K. Lee, and O. Mousis, “A possible carbon-rich interior in super-earth 55 cancri e,” *The Astrophysical Journal*, vol. 759, Oct 2012.
- [4] T. Sharp, “Bridgmanite—named at last,” *Science*, vol. 346, no. 6213, pp. 1057–1058, 2014.
- [5] G. Helffrich and B. Wood, “The earth’s mantle,” *Nature*, vol. 412, pp. 501–7, 09 2001.
- [6] M. Akaogi, E. Ito, and A. Navrotsky, “Olivine-modified spinel-spinel transitions in the system $\text{mg}_2\text{SiO}_4\text{-Fe}_2\text{SiO}_4$: Calorimetric measurements, thermochemical calculation, and geophysical application,” *Journal of Geophysical Research: Solid Earth*, vol. 94, no. B11, pp. 15671–15685, 1989.
- [7] L. Zhang, Y. Meng, W. Yang, L. Wang, W. L. Mao, Q.-S. Zeng, J. S. Jeong, A. J. Wagner, K. A. Mkhoyan, W. Liu, R. Xu, and H. kwang Mao, “Disproportionation of $(\text{mg,fe})\text{SiO}_3$ perovskite in earth’s deep lower mantle,” *Science*, vol. 344, no. 6186, pp. 877–882, 2014.
- [8] T. Duffy, N. Madhusudhan, and K. Lee, *Mineralogy of Super-Earth Planets*, vol. 2, pp. 149–178. United States: Elsevier Inc., Jan. 2015.
- [9] T. Irifune, “Absence of an aluminous phase in the upper part of the earth’s lower mantle,” *Nature*, vol. 370, p. 131–133, Jul 1994.

- [10] B. Wood, “Phase transformations and partitioning relations in peridotite under lower mantle conditions,” *Earth and Planetary Science Letters*, vol. 174, 01 2000.
- [11] F. V. Kaminsky, *Introduction*, pp. 1–3. Cham: Springer International Publishing, 2017.
- [12] F. V. Kaminsky, *Ultramafic Lower-Mantle Mineral Association*. Cham: Springer International Publishing, 2017.
- [13] S. Ritterbex, T. Harada, and T. Tsuchiya, “Vacancies in mgo at ultrahigh pressure: About mantle rheology of super-earths,” *Icarus*, vol. 305, pp. 350–357, 2018.
- [14] R. S. McWilliams, D. K. Spaulding, J. H. Eggert, P. M. Celliers, D. G. Hicks, R. F. Smith, G. W. Collins, and R. Jeanloz, “Phase transformations and metallization of magnesium oxide at high pressure and temperature,” *Science*, vol. 338, no. 6112, pp. 1330–1333, 2012.
- [15] J. K. Wicks, S. Singh, M. Millot, D. E. Fratanduono, F. Coppari, M. G. Gorman, Z. Ye, J. R. Rygg, A. Hari, J. H. Eggert, T. S. Duffy, and R. F. Smith, “B1-b2 transition in shock-compressed mgo,” *Science Advances*, vol. 10, no. 23, p. eadk0306, 2024.
- [16] F. Coppari, R. Smith, J. Eggert, J. Wang, J. Rygg, A. Lazicki, J. Hawreliak, G. Collins, and T. Duffy, “Experimental evidence for a phase transition in magnesium oxide at exoplanet pressures,” *Nature Geoscience*, vol. 6, pp. 926–929, Nov. 2013.
- [17] T. Yagi, T. Suzuki, and S.-I. Akimoto, “Static compression of wüstite (fe_{0.98}o) to 120 gpa,” *Journal of Geophysical Research: Solid Earth*, vol. 90, no. B10, pp. 8784–8788, 1985.
- [18] Y. Fei and H. kwang Mao, “In situ determination of the nias phase of feo at high pressure and temperature,” *Science*, vol. 266, no. 5191, pp. 1678–1680, 1994.
- [19] H. Ozawa, K. Hirose, S. Tateno, N. Sata, and Y. Ohishi, “Phase transition boundary between b1 and b8 structures of feo up to 210gpa,” *Physics of the Earth and Planetary Interiors*, vol. 179, no. 3, pp. 157–163, 2010.

- [20] R. A. Fischer, A. J. Campbell, O. T. Lord, G. A. Shofner, P. Dera, and V. B. Prakapenka, “Phase transition and metallization of feo at high pressures and temperatures,” *Geophysical Research Letters*, vol. 38, no. 24, 2011.
- [21] H. Ozawa, F. Takahashi, K. Hirose, Y. Ohishi, and N. Hirao, “Phase transition of feo and stratification in earth’s outer core,” *Science*, vol. 334, no. 6057, pp. 792–794, 2011.
- [22] F. Coppari, R. F. Smith, J. Wang, M. Millot, D. Kim, J. R. Rygg, S. Hamel, J. H. Eggert, and T. S. Duffy, “Implications of the iron oxide phase transition on the interiors of rocky exoplanets,” *Nature Geoscience*, vol. 14, p. 121–126, Feb 2021.
- [23] F. R.A. and C. A.J., “High pressure melting of wüstite,” *American Mineralogist*, vol. 95, p. 1473–1477, 2010.
- [24] G. Morard, D. Antonangeli, J. Bouchet, A. Rivoldini, S. Boccato, F. Miozzi, E. Boulard, H. Bureau, M. Mezouar, C. Prescher, S. Chariton, and E. Greenberg, “Structural and electronic transitions in liquid feo under high pressure,” *Journal of Geophysical Research: Solid Earth*, vol. 127, no. 11, p. e2022JB025117, 2022.
- [25] K. Ohta, R. E. Cohen, K. Hirose, K. Haule, K. Shimizu, and Y. Ohishi, “Experimental and theoretical evidence for pressure-induced metallization in feo with rocksalt-type structure,” *Phys. Rev. Lett.*, vol. 108, p. 026403, Jan 2012.
- [26] E. B. Knittle, R. Jeanloz, A. C. Mitchell, and W. J. Nellis, “Metallization of fe_{0.94}o at elevated pressures and temperatures observed by shock-wave electrical resistivity measurements,” *Solid State Communications*, vol. 59, pp. 513–515, 1986.
- [27] L. Dubrovinsky, N. Dubrovinskaia, S. Saxena, H. Annersten, E. Halenius, H. Harryson, F. Tutti, S. Rekhi, and B. T. Le, “Stability of ferropicrinite in the lower mantle,” *SCIENCE*, vol. 289, no. 5478, pp. 430–432, 2000. Addresses: Dubrovinsky LS, Uppsala Univ, Inst Earth Sci, S-75236 Uppsala, Sweden. Uppsala Univ, Inst Earth Sci, S-75236 Uppsala, Sweden. European Synchrotron Radiat Facil, F-38043 Grenoble, France.
- [28] L. Dubrovinsky, N. Dubrovinskaia, H. Annersten, E. Hålenius, and H. Harryson, “Stability of (mg_{0.5}fe_{0.5})o and (mg_{0.8}fe_{0.2})o magnesiowüstites in the lower mantle,” *European Journal of Mineralogy*, vol. 13, pp. 857–861, 09 2001.

- [29] K. Ohta, K. Fujino, Y. Kuwayama, T. Kondo, K. Shimizu, and Y. Ohishi, “Highly conductive iron-rich (mg,fe)O magnesiowüstite and its stability in the earth’s lower mantle,” *Journal of Geophysical Research: Solid Earth*, vol. 119, no. 6, pp. 4656–4665, 2014.
- [30] J.-F. Lin, D. L. Heinz, H. kwang Mao, R. J. Hemley, J. M. Devine, J. Li, and G. Shen, “Stability of magnesiowüstite in earth’s lower mantle,” *Proceedings of the National Academy of Sciences*, vol. 100, no. 8, pp. 4405–4408, 2003.
- [31] M. S. Vassiliou and T. J. Ahrens, “The equation of state of Mg_{0.6}Fe_{0.4}O to 200 gpa,” *Geophysical Research Letters*, vol. 9, no. 2, pp. 127–130, 1982.
- [32] S. Speziale, A. Milner, V. E. Lee, S. M. Clark, M. P. Pasternak, and R. Jeanloz, “Iron spin transition in earth’s mantle,” *Proceedings of the National Academy of Sciences*, vol. 102, no. 50, pp. 17918–17922, 2005.
- [33] J. M. Jackson, S. V. Sinogeikin, S. D. Jacobsen, H. J. Reichmann, S. J. Mackwell, and J. D. Bass, “Single-crystal elasticity and sound velocities of (Mg_{0.94}Fe_{0.06})O ferropericlase to 20 gpa,” *Journal of Geophysical Research: Solid Earth*, vol. 111, no. B9, 2006.
- [34] J.-F. Lin, S. D. Jacobsen, W. Sturhahn, J. M. Jackson, J. Zhao, and C.-S. Yoo, “Sound velocities of ferropericlase in the earth’s lower mantle,” *Geophysical Research Letters*, vol. 33, no. 22, 2006.
- [35] J. C. Crowhurst, J. M. Brown, A. F. Goncharov, and S. D. Jacobsen, “Elasticity of (mg,fe)O through the spin transition of iron in the lower mantle,” *Science*, vol. 319, no. 5862, pp. 451–453, 2008.
- [36] H. Marquardt, S. Speziale, H. J. Reichmann, D. J. Frost, and F. R. Schilling, “Single-crystal elasticity of (Mg_{0.9}Fe_{0.1})O to 81 gpa,” *Earth and Planetary Science Letters*, vol. 287, no. 3, pp. 345–352, 2009.
- [37] Z. Wu, J. a. F. Justo, and R. M. Wentzcovitch, “Elastic anomalies in a spin-crossover system: Ferropericlase at lower mantle conditions,” *Phys. Rev. Lett.*, vol. 110, p. 228501, May 2013.
- [38] J. Yang, X. Tong, J.-F. Lin, T. Okuchi, and N. Tomioka, “Elasticity of ferropericlase across the spin crossover in the earth’s lower mantle,” *Scientific Reports*, vol. 5, Dec 2015.

- [39] N. B. Zhang, Y. Cai, X. H. Yao, X. M. Zhou, Y. Y. Li, C. J. Song, X. Y. Qin, and S. N. Luo, “Spin transition of ferroperricite under shock compression,” *AIP Advances*, vol. 8, p. 075028, 07 2018.
- [40] H. Marquardt, J. Buchen, A. S. J. Méndez, A. Kurnosov, M. Wendt, A. Rothkirch, D. Pennicard, and H.-P. Liermann, “Elastic softening of (mg_{0.8}fe_{0.2})_o ferroperricite across the iron spin crossover measured at seismic frequencies,” *Geophysical Research Letters*, vol. 45, no. 14, pp. 6862–6868, 2018.
- [41] A. S. J. Méndez, S. Stackhouse, V. Trautner, B. Wang, N. Satta, A. Kurnosov, R. J. Husband, K. Glazyrin, H.-P. Liermann, and H. Marquardt, “Broad elastic softening of (mg,fe)_o ferroperricite across the iron spin crossover and a mixed-spin lower mantle,” *Journal of Geophysical Research: Solid Earth*, vol. 127, no. 8, p. e2021JB023832, 2022. e2021JB023832 2021JB023832.
- [42] R. J. Trainor, J. W. Shaner, J. M. Auerbach, and N. C. Holmes, “Ultrahigh-pressure laser-driven shock-wave experiments in aluminum,” *Phys. Rev. Lett.*, vol. 42, pp. 1154–1157, Apr 1979.
- [43] J. Edwards, K. T. Lorenz, B. A. Remington, S. Pollaine, J. Colvin, D. Braun, B. F. Lasinski, D. Reisman, J. M. McNaney, J. A. Greenough, R. Wallace, H. Louis, and D. Kalantar, “Laser-driven plasma loader for shockless compression and acceleration of samples in the solid state,” *Phys. Rev. Lett.*, vol. 92, p. 075002, Feb 2004.
- [44] S. Pascarelli, M. McMahon, C. Pépin, O. Mathon, R. F. Smith, W. L. Mao, H.-P. Liermann, and P. Loubeyre, “Materials under extreme conditions using large x-ray facilities,” *Nature Reviews Methods Primers*, vol. 3, Nov 2023.
- [45] A. Bharti and N. Goyal, “Fundamental of synchrotron radiations,” in *Synchrotron Radiation* (D. Joseph, ed.), ch. 2, Rijeka: IntechOpen, 2019.
- [46] J.-A. Hernandez, N. Sévelin-Radiguet, R. Torchio, S. Balugani, A. Dwivedi, G. Berruyer, D. Bugnazet, S. Chazalotte, C. Clavel, D. Lorphévret, and et al., “The high power laser facility at beamline id24-ed at the esrf,” *High Pressure Research*, vol. 44, p. 372–399, May 2024.
- [47] D. Capatina, K. D’Amico, J. Nudell, J. Collins, and O. Schmidt, “Dcs - a high flux beamline for time resolved dynamic compression science – design highlights,” *AIP Conference Proceedings*, vol. 1741, p. 030036, 07 2016.

- [48] B. Nagler, B. Arnold, G. Bouchard, R. F. Boyce, R. M. Boyce, A. Callen, M. Campell, R. Curiel, E. Galtier, J. Garofoli, E. Granados, J. Hastings, G. Hays, P. Heimann, R. W. Lee, D. Milathianaki, L. Plummer, A. Schropp, A. Wallace, M. Welch, W. White, Z. Xing, J. Yin, J. Young, U. Zastra, and H. J. Lee, “The Matter in Extreme Conditions instrument at the Linac Coherent Light Source,” *Journal of Synchrotron Radiation*, vol. 22, pp. 520–525, May 2015.
- [49] Y. Inubushi, T. Yabuuchi, T. Togashi, K. Sueda, K. Miyanishi, Y. Tange, N. Ozaki, T. Matsuoka, R. Kodama, T. Osaka, S. Matsuyama, K. Yamauchi, H. Yumoto, T. Koyama, H. Ohashi, K. Tono, and M. Yabashi, “Development of an experimental platform for combinative use of an xfel and a high-power nanosecond laser,” *Applied Sciences*, vol. 10, no. 7, 2020.
- [50] U. Zastra, K. Appel, C. Baehtz, O. Baehr, L. Batchelor, A. Berghäuser, M. Banjafar, E. Brambrink, V. Cerantola, T. E. Cowan, H. Damker, S. Dietrich, S. Di Dio Cafiso, J. Dreyer, H.-O. Engel, T. Feldmann, S. Findeisen, M. Foese, D. Fulla-Marsa, S. Göde, M. Hassan, J. Hauser, T. Herrmannsdörfer, H. Höppner, J. Kaa, P. Kaefer, K. Knöfel, Z. Konôpková, A. Laso García, H.-P. Liermann, J. Mainberger, M. Makita, E.-C. Martens, E. E. McBride, D. Möller, M. Nakatsutsumi, A. Pelka, C. Plueckthun, C. Prescher, T. R. Preston, M. Röper, A. Schmidt, W. Seidel, J.-P. Schwinkendorf, M. O. Schoelmerich, U. Schramm, A. Schropp, C. Strohm, K. Sukharnikov, P. Talkovski, I. Thorpe, M. Toncian, T. Toncian, L. Wollenweber, S. Yamamoto, and T. Tschentscher, “The High Energy Density Scientific Instrument at the European XFEL,” *Journal of Synchrotron Radiation*, vol. 28, pp. 1393–1416, Sep 2021.
- [51] P. Mason, S. Banerjee, J. Smith, T. Butcher, J. Phillips, H. Höppner, D. Möller, K. Ertel, M. De Vido, I. Hollingham, and et al., “Development of a 100j, 10hz laser for compression experiments at the high energy density instrument at the european xfel,” *High Power Laser Science and Engineering*, vol. 6, p. e65, 2018.
- [52] P. M. Celliers, D. K. Bradley, G. W. Collins, D. G. Hicks, T. R. Boehly, and W. J. Armstrong, “Line-imaging velocimeter for shock diagnostics at the omega laser facility,” *Review of Scientific Instruments*, vol. 75, pp. 4916–4929, 11 2004.
- [53] R. F. Smith, J. H. Eggert, M. D. Saculla, A. F. Jankowski, M. Bastea, D. G. Hicks, and G. W. Collins, “Ultrafast dynamic compression technique to study the kinetics

- of phase transformations in bismuth,” *Phys. Rev. Lett.*, vol. 101, p. 065701, Aug 2008.
- [54] R. F. Smith, V. Rastogi, A. E. Lazicki, M. G. Gorman, R. Briggs, A. L. Coleman, C. Davis, S. Singh, D. McGonegle, S. M. Clarke, T. Volz, T. Hutchinson, C. McGuire, D. E. Fratanduono, D. C. Swift, E. Folsom, C. A. Bolme, A. E. Gleason, F. Coppari, H. Ja Lee, B. Nagler, E. Cunningham, P. Heimann, R. G. Kraus, R. E. Rudd, T. S. Duffy, J. H. Eggert, and J. K. Wicks, “Development of slurry targets for high repetition-rate x-ray free electron laser experiments,” *Journal of Applied Physics*, vol. 131, p. 245901, 06 2022.
- [55] J. Fritz and A. Greshake, “High-pressure phases in an ultramafic rock from mars,” *Earth and Planetary Science Letters*, vol. 288, no. 3, pp. 619–623, 2009.
- [56] D. A. Pavlov, A. I. Bobrov, N. V. Malekhonova, A. V. Pirogov, and A. V. Nezhdanov, “Self-assembled nanocrystals discovered in chelyabinsk meteorite,” *Scientific Reports*, vol. 4, Mar 2014.
- [57] A. V. Rane, K. Kanny, V. Abitha, and S. Thomas, *Chapter 5 - Methods for Synthesis of Nanoparticles and Fabrication of Nanocomposites*. Micro and Nano Technologies, Woodhead Publishing, 2018.
- [58] N. Haldar, T. Mondal, and C. K. Ghosh, *Carbon-based coatings: Synthesis and applications*. Elsevier, 2023.
- [59] C. Plückthun, *Investigating the effect of the compression rate on the kinetic response of diamond anvil cell experiments*. PhD thesis, Universität Rostock, 2021.
- [60] R. H. Nafziger, G. C. Ulmer, and E. Woermann, *Gaseous Buffering for the Control of Oxygen Fugacity at One Atmosphere*, pp. 9–41. Berlin, Heidelberg: Springer Berlin Heidelberg, 1971.
- [61] I. Prencipe, J. Fuchs, S. Pascarelli, D. W. Schumacher, R. B. Stephens, N. B. Alexander, R. Briggs, M. Büscher, M. O. Cernaiianu, A. Choukourov, and et al., “Targets for high repetition rate laser facilities: needs, challenges and perspectives,” *High Power Laser Science and Engineering*, vol. 5, p. e17, 2017.
- [62] D. Riley, “Shock and ramp compression,” in *Warm Dense Matter*, 2053-2563, pp. 2–1 to 2–29, IOP Publishing, 2021.

- [63] P. M. Celliers, G. W. Collins, D. G. Hicks, and J. H. Eggert, “Systematic uncertainties in shock-wave impedance-match analysis and the high-pressure equation of state of Al,” *Journal of Applied Physics*, vol. 98, p. 113529, 12 2005.
- [64] H.-S. Park, S. J. M. Ali, P. M. Celliers, F. Coppari, J. Eggert, A. Krygier, A. E. Lazicki, J. M. McNaney, M. Millot, Y. Ping, R. E. Rudd, B. A. Remington, H. Sio, R. F. Smith, M. D. Knudson, and E. E. McBride, “Techniques for studying materials under extreme states of high energy density compression,” *Physics of Plasmas*, vol. 28, p. 060901, 06 2021.
- [65] J. M. Walsh and R. H. Christian, “Equation of state of metals from shock wave measurements,” *Phys. Rev.*, vol. 97, pp. 1544–1556, Mar 1955.
- [66] J. W. Forbes, *Impedance Matching Technique*, pp. 31–57. Berlin, Heidelberg: Springer Berlin Heidelberg, 2012.
- [67] A. Denoëud, J.-A. Hernandez, T. Vinci, A. Benuzzi-Mounaix, S. Brygoo, A. Berlioux, F. Lefevre, A. Sollier, L. Videau, A. Ravasio, M. Guarguaglini, L. Duthoit, D. Loison, and E. Brambrink, “X-ray powder diffraction in reflection geometry on multi-beam kJ-type laser facilities,” *Review of Scientific Instruments*, vol. 92, p. 013902, 01 2021.
- [68] A. L. Meadowcroft, C. D. Bentley, and E. N. Stott, “Evaluation of the sensitivity and fading characteristics of an image plate system for x-ray diagnostics,” *Review of Scientific Instruments*, vol. 79, p. 113102, 11 2008.
- [69] G. Boutoux, D. Batani, F. Burgy, J.-E. Ducret, P. Forestier-Colleoni, S. Hulin, N. Rabhi, A. Duval, L. Lecherbourg, C. Reverdin, K. Jakubowska, C. I. Szabo, S. Bastiani-Ceccotti, F. Consoli, A. Curcio, R. De Angelis, F. Ingenito, J. Baggio, and D. Raffestin, “Validation of modelled imaging plates sensitivity to 1-100 keV x-rays and spatial resolution characterisation for diagnostics for the “petawatt aquitaine laser”,” *Review of Scientific Instruments*, vol. 87, p. 043108, 04 2016.
- [70] R. Ramis, R. Schmalz, and J. Meyer-Ter-Vehn, “Multi — a computer code for one-dimensional multigroup radiation hydrodynamics,” *Computer Physics Communications*, vol. 49, no. 3, pp. 475–505, 1988.
- [71] R. A. Fischer, A. J. Campbell, G. A. Shofner, O. T. Lord, P. Dera, and V. B.

- Prakapenka, “Equation of state and phase diagram of feo,” *Earth and Planetary Science Letters*, vol. 304, no. 3, pp. 496–502, 2011.
- [72] H. Oettel and R. Wiedemann, “Residual stresses in pvd hard coatings,” *Surface and Coatings Technology*, vol. 76-77, pp. 265–273, 1995.
- [73] B. H. Toby and R. B. Von Dreele, “*GSAS-II*: the genesis of a modern open-source all purpose crystallography software package,” *Journal of Applied Crystallography*, vol. 46, pp. 544–549, Apr 2013.
- [74] X. Cao, Y. Wang, X. Li, L. Xu, L. Liu, Y. Yu, R. Qin, W. Zhu, S. Tang, L. He, C. Meng, B. Zhang, and X. Peng, “Refractive index and phase transformation of sapphire under shock pressures up to 210GPa,” *Journal of Applied Physics*, vol. 121, p. 115903, 03 2017.
- [75] H. Liu, J. S. Tse, and W. J. Nellis, “The electrical conductivity of Al_2O_3 under shock-compression,” *Scientific Reports*, vol. 5, Aug 2015.
- [76] R. Jeanloz and T. J. Ahrens, “Equations of state of feo and cao,” *Geophysical Journal International*, vol. 62, pp. 505–528, 1980.
- [77] R. M. Hazen and R. Jeanloz, “Wüstite (Fe_{1-x}O): A review of its defect structure and physical properties,” *Reviews of Geophysics*, vol. 22, no. 1, pp. 37–46, 1984.
- [78] C. A. McCammon and L.-g. Liu, “The effects of pressure and temperature on non-stoichiometric wüstite, Fe_{1-x}O : The iron-rich phase boundary,” *Physics and Chemistry of Minerals*, vol. 10, p. 106–113, Feb 1984.
- [79] V. V. Dobrosavljevic, D. Zhang, W. Sturhahn, S. Chariton, V. B. Prakapenka, J. Zhao, T. S. Toellner, O. S. Pardo, and J. M. Jackson, “Melting and defect transitions in feo up to pressures of earth’s core-mantle boundary,” *Nature Communications*, vol. 14, Nov 2023.
- [80] H. Ozawa, K. Hirose, K. Ohta, H. Ishii, N. Hiraoka, Y. Ohishi, and Y. Seto, “Spin crossover, structural change, and metallization in nias-type feo at high pressure,” *Phys. Rev. B*, vol. 84, p. 134417, Oct 2011.
- [81] E. Greenberg, R. Nazarov, A. Landa, J. Ying, R. Q. Hood, B. Hen, R. Jeanloz, V. B. Prakapenka, V. V. Struzhkin, G. K. Rozenberg, and I. V. Leonov, “Phase transitions

- and spin state of iron in feo under the conditions of earth's deep interior," *Phys. Rev. B*, vol. 107, p. L241103, Jun 2023.
- [82] T. Komabayashi, "Thermodynamics of melting relations in the system fe-feo at high pressure: Implications for oxygen in the earth's core," *Journal of Geophysical Research: Solid Earth*, vol. 119, no. 5, pp. 4164–4177, 2014.
- [83] K. Katagiri, N. Ozaki, D. Murayama, K. Nonaka, Y. Hironaka, Y. Inubushi, K. Miyanishi, H. Nakamura, T. Okuchi, T. Sano, Y. Seto, K. Shigemori, K. Sueda, T. Togashi, Y. Umeda, M. Yabashi, T. Yabuuchi, and R. Kodama, "Hugoniot equation-of-state and structure of laser-shocked polyimide $c_{22}h_{10}n_2o_5$," *Phys. Rev. B*, vol. 105, p. 054103, Feb 2022.
- [84] S. Marsh and L. Properties, *LASL Shock Hugoniot Data*. Los Alamos Scientific Laboratory Series on Dynamic Material Properties, Vol 5, University of California Press, 1980.
- [85] D. G. Hicks, T. R. Boehly, P. M. Celliers, J. H. Eggert, E. Vianello, D. D. Meyerhofer, and G. W. Collins, "Shock compression of quartz in the high-pressure fluid regime," *Physics of Plasmas*, vol. 12, p. 082702, 08 2005.
- [86] M. D. Knudson and M. P. Desjarlais, "Shock compression of quartz to 1.6 tpa: Redefining a pressure standard," *Phys. Rev. Lett.*, vol. 103, p. 225501, Nov 2009.
- [87] M. D. Knudson and M. P. Desjarlais, "Adiabatic release measurements in α -quartz between 300 and 1200 gpa: Characterization of α -quartz as a shock standard in the multimegabar regime," *Phys. Rev. B*, vol. 88, p. 184107, Nov 2013.
- [88] D. G. Hicks, T. R. Boehly, J. H. Eggert, J. E. Miller, P. M. Celliers, and G. W. Collins, "Dissociation of liquid silica at high pressures and temperatures," *Phys. Rev. Lett.*, vol. 97, p. 025502, Jul 2006.
- [89] G. Ghosh, "Dispersion-equation coefficients for the refractive index and birefringence of calcite and quartz crystals," *Optics Communications*, vol. 163, no. 1, pp. 95–102, 1999.
- [90] M. A. Meyers, *Shock Waves*, ch. 4, pp. 98–123. John Wiley & Sons, Ltd, 1994.
- [91] G. I. Kerley, "The linear us-up relation in shock-wave physics," 2013.

- [92] J. Kieffer and J. Wright, “Pyfai: a python library for high performance azimuthal integration on gpu,” *Powder Diffraction*, vol. 28, no. S2, p. S339–S350, 2013.
- [93] C. Prescher and V. B. Prakapenka, “Dioptas: a program for reduction of two-dimensional x-ray diffraction data and data exploration,” *High Pressure Research*, vol. 35, no. 3, pp. 223–230, 2015.
- [94] T. Wan, Y. Sun, and R. M. Wentzcovitch, “Intermediate spin state and the b_1 – b_2 transition in ferroperricite,” *Phys. Rev. Res.*, vol. 4, p. 023078, Apr 2022.
- [95] F. Della Pia and D. Alfè, “ b_1 – b_2 phase transition of ferroperricite at planetary interior conditions,” *Phys. Rev. B*, vol. 105, p. 134109, Apr 2022.
- [96] O. E. Petel and F. X. Jetté, “Comparison of methods for calculating the shock hugoniot of mixtures,” *Shock Waves*, vol. 20, p. 73–83, Sep 2009.
- [97] Y. Fei, L. Zhang, A. Corgne, H. Watson, A. Ricolleau, Y. Meng, and V. Prakapenka, “Spin transition and equations of state of (mg, fe)_o solid solutions,” *Geophysical Research Letters*, vol. 34, no. 17, 2007.
- [98] T. Komabayashi, K. Hirose, Y. Nagaya, E. Sugimura, and Y. Ohishi, “High-temperature compression of ferroperricite and the effect of temperature on iron spin transition,” *Earth and Planetary Science Letters*, vol. 297, no. 3, pp. 691–699, 2010.
- [99] N. V. Solomatova, J. M. Jackson, W. Sturhahn, J. K. Wicks, J. Zhao, T. S. Toellner, B. Kalkan, and W. M. Steinhardt, “Equation of state and spin crossover of (mg,fe)_o at high pressure, with implications for explaining topographic relief at the core-mantle boundary,” *American Mineralogist*, vol. 101, no. 5, pp. 1084–1093, 2016.
- [100] K. Hirose, G. Morard, R. Sinmyo, K. Umemoto, J. Hernlund, G. Helffrich, and S. Labrosse, “Crystallization of silicon dioxide and compositional evolution of the earth’s core,” *Nature*, vol. 543, p. 99–102, Feb 2017.
- [101] R. Trønnes, M. Baron, K. Eigenmann, M. Guren, B. Heyn, A. Løken, and C. Mohn, “Core formation, mantle differentiation and core-mantle interaction within earth and the terrestrial planets,” *Tectonophysics*, vol. 760, pp. 165–198, 2019. Linking Plate Tectonics and Volcanism to Deep Earth Dynamics – a tribute to Trond H. Torsvik.

-
- [102] C.-E. Boukaré, Y. Ricard, and G. Fiquet, “Thermodynamics of the mgo-feo-sio₂ system up to 140 gpa: Application to the crystallization of earth’s magma ocean,” *Journal of Geophysical Research: Solid Earth*, vol. 120, no. 9, pp. 6085–6101, 2015.
- [103] M. Manga and R. Jeanloz, “Implications of a metal-bearing chemical boundary layer in d” for mantle dynamics,” *Geophysical Research Letters*, vol. 23, no. 22, pp. 3091–3094, 1996.
- [104] Q. Williams, R. Jeanloz, J. Bass, B. Svendsen, and T. J. Ahrens, “The melting curve of iron to 250 gigapascals: A constraint on the temperature at earth’s center,” *Science*, vol. 236, p. 181–182, Apr 1987.
- [105] D. Valencia, R. J. O’Connell, and D. Sasselov, “Internal structure of massive terrestrial planets,” *Icarus*, vol. 181, no. 2, pp. 545–554, 2006.
- [106] S. Ritterbex, T. Harada, and T. Tsuchiya, “Vacancies in mgo at ultrahigh pressure: About mantle rheology of super-earths,” *Icarus*, vol. 305, pp. 350–357, 2018.
- [107] S. ichiro Karato, “Rheological structure of the mantle of a super-earth: Some insights from mineral physics,” *Icarus*, vol. 212, no. 1, pp. 14–23, 2011.

Curriculum Vitae

Education

- March 2021 – March 2025: European XFEL, Germany.
Ph.D. student of the HED group, European XFEL and the Statistical Physics Group, University of Rostock.
Supervisors: Prof. Dr. Ronald Redmer, Dr. Karen Appel.
- September 2018 – June 2020: Lund University, Sweden.
Master of Science (M.Sc.) in Physics.
Thesis topic: X-ray imaging at high brilliance sources.
- May 2013 – May 2017: Chiang Mai University, Thailand.
Bachelor of Science (B.Sc.) in Physics.
Thesis topic: Beam dynamic simulation of photocathode RF electron gun.

Scholarship and Research experiences

- 2020 – 2021: Chiang Mai University.
Research assistant: Plasma and beam physics research facility.
- 2017: Chiang Mai University.
Teaching assistant: Introduction to electromagnetic theory 1.
- 2013 – present: Thai government scholarship.
Development and promotion of science and technology talents project (DPST).

Statement of authorship

I hereby declare that I am the sole author of this thesis and that I have not used any sources other than those listed in the bibliography and identified as references. I further declare that I have not submitted this thesis at any other institution in this form or otherwise.

Ich versichere hiermit an Eides statt, dass ich die vorliegende Arbeit selbständig angefertigt und ohne fremde Hilfe verfasst habe, keine außer den von mir angegebenen Hilfsmitteln und Quellen dazu verwendet habe und die den benutzten Werken inhaltlich und wörtlich entnommenen Stellen als solche kenntlich gemacht habe. Weiterhin versichere ich, dass ich diese Arbeit an keiner anderen Institution in dieser oder einer ähnlichen Form eingereicht habe.

Khachiwan Buakor

Rostock, 20. Dezember 2024

